Photocatalytic degradation of some pesticides and polycyclic aromatic hydrocarbons by metal doped titania nanoparticles

Thesis submitted in fulfillment of the
requirement of the degree of
Doctor of Philosophy

By

Inderpreet Singh Grover

(Regd. No. 900909010)

School of Chemistry & Biochemistry
Thapar University, Patiala - 147 004
Punjab (India)
November-2014

Certificate

This is to certify that the thesis entitled "***Photocatalytic degradation of some pesticides and polycyclic aromatic hydrocarbons by metal doped titania nanoparticles***" being submitted by Mr. Inderpreet Singh Grover in fulfillment of the requirement for the award of the degree of Doctor of Philosophy in School of Chemistry and Biochemsitry, Thapar University, Patiala, is a record of candidate's own independent and original research work carried out by him under our supervision and guidance. The material embodied in this thesis has not been submitted in part or full to any other University or Institute for the award of any degree.

13/11/2014

Dr. Stanam Singh
Associate Professor
School of Chemistry and Biochemistry
Thapar University, Patiala-147004
Punjab (India)

13.11.2014

Dr. Bonamali Pal
Professor & Head
School of Chemistry and Biochemistry
Thapar University, Patiala-147004
Punjab (India)

Candidate's Declaration

I, hereby declare that the work presented in the thesis entitled "***Photocatalytic degradation of some pesticides and polycyclic aromatic hydrocarbons by metal doped titania nanoparticles***" in fulfillment of the requirement for the award of the degree of Doctor of Philosophy being submitted to School of Chemistry and Biochemistry, Thapar University, Patiala, is an authentic record of my own work carried out under the supervision of Dr. Stanam Singh and Dr. Bonamali Pal, School of Chemistry and Biochemistry, Thapar University, Patiala (India). The matter embodied in this thesis has not been submitted in part or full to any other university or institute for the award of any degree in India or Abroad.

Place: Patiala

Date: 13-11-2014

13-11-2014

(Inderpreet Singh Grover)

Acknowledgements

I humbly prostrate myself before the Almighty God for his grace and enduring blessings which enabled me to complete this work successfully with my full satisfaction.

First and foremost, I would like to express my sincere gratitude to my research supervisors ***Dr. Satnam Singh and Dr. Bonamali Pal,*** *for introducing me to this exciting field of science and for his valuable guidance, continuous support, motivation and patience throughout the Ph.D. work. I have learnt extensively from his, including how to regard an old question from a new perspective and how to approach a problem by systematic thinking. Their persistent courage and confidence will always inspire me, and I hope to continue to work with his noble thoughts. I am really glad to be associated with persons like them in my life.*

I am profoundly obliged to ***Dr. Bonamali Pal****, Professor and Head, School of Chemistry and Biochemistry, Thapar University, Patiala for their good wishes and motivation.*

I would like to thank my doctoral committee for their encouragement, constructive criticism and inspirations.

Special regards to my beginning teachers and teachers of the School of Chemistry and Biochemistry for providing suggestions and taking interest in the progress of work along with lab facility. Deep sense of gratitude to all because of whose teaching at different stages of education has made it possible for me to see this day.

I am thankful to my lab-mates and other friends for always standing by my side and sharing a great relationship as compassionate friends. I will forever cherish the warmth shown by them, whose smiling face always made me refreshing.

A special thanks to ***Mr. Gurmeet Singh Lotey****,* ***Mr. Jaspal Singh and Mr. Paramjot Jha*** *for their timely support and lively discussions.*

I would like to thank ***other staff*** *of the School of Chemistry and Biochemistry, Thapar University, Patiala for the constant official help and cooperation.*

I would like to pay high regards to my mother ***Mrs. Inderjeet Kaur,*** *my father* ***Balwinder Singh,*** *for their love, affection, patience and blessings. I am extremely happy to fulfill their ultimate desire that today, I achieve.*

Most of the results described in this thesis would not have been possible without the help of laboratories at the institutes like, ***SAI,*** *Thapar University, Patiala,* ***SAIF****, Punjab University, Chandigarh,* ***AIRF****, Jawaharlal Nehru University, Delhi,* ***SAIF,*** *IIT Bombay.*

I gratefully acknowledge, ***University Grants Commission, New Delhi (India),*** *for providing me financial support in the initial years and Thapar University, Patiala (India) for financial support in the later years.*

13-11-2014

(Inderpreet Singh Grover)

Table of Contents

List of Symbols/Abbreviations

e^-	Electron
h^+	Hole
CB	Conduction Band
VB	Valence Band
SC	Semiconductor
M	Metal
-OH	Hydroxyl group
E_g	Band gap energy
nm	Nano-meter
µm	Micro-meter
µs	Micro-second
sec	Second
min	Minute
h	Hour
g	Gram
µg	Micro-gram
ml	Milli-liter
µl	Micro-liter
µmol	Micro-moles
Å	Angstrom
%	Percentage
at.%	Atomic Percentage
wt%	Weight Percentage
vol%	Volume Percentage
ca.	Calculated
ppm	Parts Per Million
λ	Wavelength
L	Length
D	Diameter

UV	Ultra Violet
Vis	Visible
ζ	Zeta potential
P25	Commercially available P25-TiO2
TNT	Sodium Titanate Nanotubes
TNT(S)	Sodium Titanate Nanorods
TNR	TiO_2 Nanorods
TNW	TiO_2 Nanowires
TNP	TiO_2 Nanoparticles
TNPg	Titania Nanopolygons
PCA	Photocatalytic Activity
M-TNP	Metal loaded Titania Nanoparticles
TNT-Au^{+3}(I)	Au^{+3} (Insitu) impregnated sodium titanate nanotubes
TNT-Au^{+3}(IS)	Au^{+3} (Insitu) impregnated sodium titanate nanotubes calcined at 800 ^oC
TNT-Au^o(P)	Au photodeposited sodium titanate nanotubes
TNT-Au^o(PS)	Au photodeposited sodium titanate nanotubes calcined at 800 ^oC
TNT-Au(M)	Au-nanospheres mixed sodium titanate nanotubes
TNT-Au(MS)	Au-nanospheres mixed sodium titanate nanotubes calcined at 800 ^oC
PZC	Point of Zero Charge
IMI	Imidacloprid
MP	Methyl Parathion
m-DNB	*m*-dinitrobenzene
m-DAB	*m*-diaminobenzene
m-NA	*m*-nitroaniline
C_{strain}	Compression Strain
τ_{av}	Average lifetime of excited charge carriers
TiO_2(A)	Anatase TiO_2
TiO_2(R)	Rutile TiO_2
C-2 to C-9	TiO_2 Nanorods calcined at 200-900 ^oC
Au-C-8	Au-photodeposited TiO_2 Nanorods calcined at 800 ^oC
TCD	Thermal Conductivity Detector

HPLC	High Performance Liquid Chromatography
GC	Gas Chromatograph
GC-MS	Gas Chromatograph coupled to Mass Spectrometer
IC	Ion Chromatograph
I-1 to I-8	Identified photoproduced intermediates of imidacloprid
DRS	Diffuse Reflectance Spectroscope
SEM	Scanning Electron Microscope
EDS	Energy Dispersive Spectra
FE-SEM	Field Emission Scanning Electron Microscope
TEM	Transmission Electron Microscope
XRD	X-Ray Diffraction
S_{BET}	Brunauer, Emmett and Teller Surface Area
FT-IR	Fourier Transformed Infrared
DLS	Dynamic Light Scattering
$^{\bullet}OH$	Hydroxyl radical
$O_2^{-\bullet}$	Superoxide radical

Abstract

Photocatalysis is an area of immense research for finding suitable benign photocatalyst for fast and complete mineralization of environmental pollutants such as pesticides and polycyclic aromatic hydrocarbons. Undeniably, TiO_2 specifically P25-TiO_2 which is commercially available TiO_2 have been widely studied for the same, however suffers from some disadvantages such as crystal phase transformation at high temperature, UV-light sensitivity and low percentage of mineralization of above mentioned molecules, limiting its utilization. This creates a scope to modify TiO_2 and/or to find other Ti-O based materials possessing similar physicochemical properties but with improved photocatalytic activity for decomposition of aforementioned molecules. In this context, present work considers the synthesis of titania/titanate nanostructures in different sizes, shapes, crystal structures which were loaded by metals/coated by SiO_2 of different shell thickness and studied for the decomposition of some pesticides and polycyclic aromatic hydrocarbons to CO_2 in comparison to P25-TiO_2.

Titania based nanocatalysts such as sodium titanates of different morphology having superior surface properties are getting wide importance in photocatalytic research. Despite having sodium (Na) content and its high temperature synthesis (that generally deteriorate the photoactvity), these Na-titanates often exhibit better photoactivity than P25-TiO_2 catalyst. Hence, **chapter-3** demonstrated the influence of crystal structure, BET surface area, surface charge, zeta potential and metal loading on the photocatalytic activity of as-prepared sodium titanate nanotubes and titania nanorods. Straw like hollow orthorhombic nanotube ($Na_2Ti_2O_5 \cdot H_2O$) particles (diameter = 9-12 nm and length = 82-115 nm) and rice like anatase nanorod particles (diameter = 8–13 nm and length = 81-134 nm) were obtained by the hydrothermal treatment of P25-TiO_2 with NaOH, which in fact, altered the net surface charge of these as-prepared nanoparticles. The observed zeta potential = -2.82 (P25-TiO_2), -13.5 (nanotubes) and -22.5 mV (nanorods) are significantly altered by the Ag and Cu deposition. It has been found here that nanotube particles displayed best photocatalytic activity for imidacloprid insecticide degradation to CO_2 formation under UV irradiation because of its largest surface area 176 m^2g^{-1} among the studied catalysts.

Sodium titanate nanotubes having higher photocatalytic activity than P25-TiO_2 was photodeposited by Ag-nanoparticles (0.2-1.0 wt%, 3-5 nm) and studied for decomposition of imidacloprid in **chapter-4**. The enhanced pseudo-first order rate constants for photooxidation of

imidacloprid to CO_2 were found to increase with increase in Ag-photodeposition onto nanotubes upto 0.5 wt%. The investigation for the fate of heteroatoms (N, O and Cl) present in imidacloprid showed increase in formation of inorganic ions (nitrate, nitrite and chloride) with time of photooxidation as confirmed by Ion chromatograph. Despite complete degradation of imidacloprid in 180 min, its mineralization to CO_2 was 70% due to formation of some persistent heteroatom containing intermediates as revealed by time dependant GC-MS study. Based upon these results, a probable pathway for mineralization of imidacloprid and a chemical mass balanced equation in relation to theoretically expected equation after its complete mineralization is proposed and described.

Preparation of crystalline monoclinic stick like sodium titanate nanorods by calciantion (at 800 ^oC) of sodium titanate nanotubes, having much less surface area (21 m^2g^{-1}) but higher average relaxation time of excited charge carriers to that of nanotubes and P25-TiO_2, as confirmed by XRD, TEM and time resolved photoluminescence decay studies is presented in **chapter-5**. These nanostructures were modified by Au-photodeposition (0.5 and 2.0 wt%) and studied for photoreduction of m-dinitrobenzene and photooxidation of sulfosulfuron. The selective formation of m-diaminobenzene by photoreduction of m-dinitrobenzene was comparable to sodium titanate nanorods (89.5 ± 0.5%) and P25-TiO_2 (98.2±0.8%), whereas Au-deposition (0.5 and 2 wt%) notably altered the products (m-nitroaniline and m-diaminobenzene) distribution after 8 h of UV-light irradiation, confirmed by GC-MS analysis. This high photoactivity of as-prepared nanorods could be credited to better delocalization and longer relaxation lifetime (68 µs) of photoexcited e^-/h^+ pairs along the length of crystalline sodium titanate nanorods than P25-TiO_2 (45 µs). The photooxidation of sulfosulfuron herbicide (1000 ppm) and corresponding CO_2 formation was found to be highest with sodium titanate nanotubes due to the presence of more hydroxyl groups over the largest surface area which was found to dominates over its least relaxation lifetime (41 µs).

An understanding of the collective influence of Au-loading and calcination for the change in crystal-structure, morphology, phase composition and their photocatalytic-activity of titanate-nanostructures is investigated in **chapter-6**. Bare and Au-loaded (Au^{+3}, Au^o and Au-nanoparticles) sodium-titanate-nanotubes were calcined in air at 800 ^oC, where TNT having BET-surface-area 176 m^2g^{-1} transformed into sodium-titanate-nanorods of surface-area of 21 m^2g^{-1} while Au-loaded nanotubes led to a variety of fragmented-particles having different

crystal-structures, surface-area (21-39 m^2g^{-1}) and sizes (50-75 nm), attributed to the strain induced thermal-decomposition of nanotubes after Au-loading. Their comparative photocatalytic- activities were evaluated by the photooxidation of insecticide imidacloprid with identification of intermediates formed during its mineralization to CO_2 under UV-light irradiation, where 0.5 wt% Au^o-deposited-nanotubes followed by calcination showed highest photocatalytic-activity in-contrast to other catalysts. These results are well explained in correlation with their crystal phase, surface-area, size, shape, and relaxation time of photoexcited electron-hole pairs.

An important finding of the present work is delivered by **chapter-7**, showing complete retention (> 98%) of anatase TiO_2 crystalline phase after high temperature (800 ^oC) treatment of rice-like TiO_2 nanorods relative to 100% conversion of the rutile phase after calcination of P25-TiO_2 under similar conditions. In addition to XRD, the existence of anatase phase at > 800 ^oC was confirmed by the presence of its characteristic vibrational bands (144, 395, 513 and 639 cm^{-1}) in the Raman spectra. It was found that TiO_2 nanorods undergo fragmentation to a highly crystalline irregular morphology (60-70 nm), nanopolygons (91-110 nm) and smaller rod-shaped particles (length = 60-110 nm and diameter = 7-12 nm), accompanied by a gradual increase in their crystallite size (from 16 to 40 nm) and decrease in surface area (from 79 to 31 $m^2\ g^{-1}$) with increased calcination temperatures from 200 to 900 ^oC. This TiO_2 anatase phase displayed enhanced photocatalytic oxidation rate (~2–11 times higher than rutile TiO_2) for methyl parathion (a neurotoxic pesticide) degradation to various intermediate products and ultimately to CO_2, whereas 1.0 wt% Au–TiO_2 significantly improved the photoactivity.

Preparation of SiO_2 coated TiO_2 particles having different thickness of silica shell and their comparative photocatalytic activity, for the photooxidation of naphthalene (20 ppm) and anthracene (20 ppm) is shown in **chapter-8**. The presence of SiO_2 over TiO_2 was demonstrated by FT-IR analysis, showing peaks corresponding to Si-O-Si (1081 cm^{-1}) and Si-O-Ti (950 cm^{-1}) bonds. HR-TEM analysis confirmed the presence of SiO_2 in as-prepared samples of shell thickness 12-15 nm and > 50 nm, with Si amount (0.8-4.2 at.%) determined by EDS analysis. Increase in thickness of SiO_2 increases the surface area of TiO_2 (69-235 m^2g^{-1}) which in turn improves the adsorption of naphthalene/anthracene. However, the observed trend for the photocatalytic activity is in contrast to the trend of adsorption studies, where, as-prepared samples with highest surface area exhibited the least photocatalytic activity, while catalyst of

least surface area (among silica coated samples) showed highest activity for degradation of naphthalene and anthracene to CO_2. Despite complete degradation of naphthalene and anthracene, an incomplete mineralization occurred, ascribed to the existence of various intermediates identified by GC-MS analysis.

Influence of TiO_2 morphology and Au-loading (1.0 wt%) for photocatalytic activity under UV- and Sun-light is delivered in **chapter-9**. The phase composition obtained by XRD study of as-prepared TiO_2 nanowires (anatase = 72%, rutile = 28%) was found to be almost similar to commercially available P25-TiO_2 (anatase = 70%, rutile = 30%). SEM analysis revealed the presence of elongated nanostructures corresponding to length = 1.9-8.0 μm and diameter = 80-270 nm for bare sample. The TEM analysis for Au-loaded TNW showed uniform dispersion of Au nanoparticles (3-6 nm) over elongated nanostructures having dimension in agreement with the SEM analysis. Time resolved analysis revealed that by changing the shape from nearly spherical (P25-TiO_2) to lengthy nanostructures, the recombination time of e^-/h^+ pair increases from 45 to 64 μs and was 79 μs after Au-loading on the later. The photocatalytic activity of bare and Au-loaded TiO_2 nanowires under UV- and Sun-light was assessed by decomposition of propiconazole to CO_2, where Au-loaded TNW always exhibited higher activity than P25-TiO_2, and various intermediates after its complete degradation were identified by GC-MS analysis.

1. Introduction and literature survey

1.1 Principle of TiO_2 photocatalysis

Nanocrystalline TiO_2 an n-type semiconductor of band gap energy (E_g) ~3.0-3.2 ev (vs NHE), have been widely studied [1-10] as photocatalyst for decomposition of environmental pollutants. It mainly exist in three crystal pahses, namely, anatase, rutile and brookite. Generally, TiO_2 having anatse (~70%) and rutile (~30%) exhibit higher photocatalytic activity (for degradation of pollutants) than any of these phase alone and is found in commericallly avaliable P25-TiO_2 (P25). Upon photoirradiation of TiO_2 under ultraviolet (UV) and/or visible (Vis.) light from sunlight or an illuminated light source having energy ≥ its band gap energy (E_g), electrons (e^-) in its valence band (VB) gets excited to the conduction band (CB) resulting into the formation of the positively charged holes (h^+) in the VB and diffuse [1-3] to the surface from the bulk of the catalyst. The photogenerated h^+ having strong oxidizing power (+3.1 V vs NHE) reacts with either adsorbed water molecules or other chemical species to form hydroxyl radicals or directly oxidizes [1-5] the molecules at interface TiO_2 and e- in the CB (-0.5 to -1.5 V vs NHE) participates for reduction processes that converts the adsorbed molecular oxygen to oxidative superoxide radical anions ($O_2^{\bullet-}$) or reduces [1-10] the substrate molecule. There are indeed other good reasons for favoring TiO_2 which includes strong oxidizing power, photogenerated e^- that are reducing enough to produce superoxide from molecular oxygen, antibacterial activity, self-cleaning activity, cost effective, chemically inert, and most importantly its non-toxicity to living beings, favouring its use as a photocatalyst.

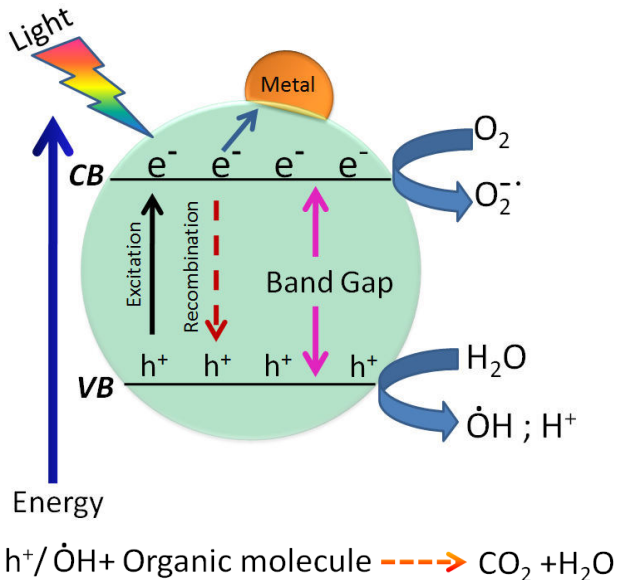

Fig. 1.1 Mechanism of photocatalysis.

Effect of metal loading on photocatalytic activity of TiO_2:

The photocatalytic performance of TiO_2 can be further improve by metal (M) loading, and is frequently used for variety of applications, viz., in solar energy conversion, photocatalysis

and electronic devices [1,4,5,11]. These M-TiO_2 hybrid nanoparticles often exhibit noticeably different properties than the individual components due to separate electron and dielectric confinement in the TiO_2 and M part, respectively [4,5]. The photoproduced charge carries in the TiO_2 can be transferred efficiently to the M part, resulting in shifting of plasmon frequency and/or promotion of redox reactions by suppressing the recombination of excited charge species as seen in Fig. 1.1. Another advantageous function of metal loading is comprehensible and incoherent interactions between M and TiO_2, leading to broadening and extension of its absorbance spectra to the visible region [1,2,4,5,8]. Generally, noble metals (e.g. Au, Ag, Ni, Cu, Pt, Rh, and Pd) with Fermi level lower than TiO_2 should have been deposited on its surface for enhanced charge separation [1,4,5,8] and is advantageous compared with other photosensitized systems because of its relatively more stability in an aerated atmosphere [1]. Therefore, theses M-TiO_2 composites have been utilized for the photodegradation/decomposition of toxic organic pollutants such for the waste water treatment and removal of other environmental pollutants such as dyes [1-6,8-10], dehydrogenation of alcohols [12,13], reduction of pharmaceutically important nitrocompounds [14-16], degradation of polycyclic aromatic hydrocarbons (PAHs) [17-30] and other heteroatom containing organic molecules such as pesticides [31-53].

1.2 Pesticides

Pesticides are the organic compounds that are used [54,55] to enhance the crop production by reducing/inhibiting/mitigating/killing the target species. However, their irregular and indiscriminate application, acute toxicity at low concentration, bio-reluctance nature, inefficient transfer (~ 0.1%) to the target organism resulted in contamination of soil, water and air, where it can adversely affect [54,56] the non-target organisms. Moreover, because of longer half life ($t_{1/2}$) i.e., slow natural degradation and over use of pesticides led to their accumulation [54-56] in the environment. The pesticides once enter in the food chain are reported [58,59] to undergo biomagnification i.e., their amount in tissue becomes many fold than that found in surroundings. This has been identified as the cause for disturbed ecological system and is a threat for the humans too. For instance, Malwa region of Punjab is found to be highly contaminated [86-88] by the pesticides. Analysis of water and vegetable samples from this area showed the presence [87,88] of pesticides, such as a carcinogen heptachlor with its content higher (0.00004-0.006 ppm) than that of its permissible (0.00003 ppm) limit. Along with this, there is a threat to

human lives as excessive use of pesticides can cause diseases like cancer, e.g., reports [59a,59b] showed that 560 persons are suffering from cancer per 100000 population in this region.

There are more than 500 pesticide formulations that are in use most of them have been admitted in agricultural fields. Pesticides depending upon their molecular structure can be categorized into nine groups viz., phenylurea (sulfosulfuron, amidosulfuron, imidacloprid etc.), carbamates (methomyl, isolan etc.), triazines (atrazine, simazine etc.), organochlorines (endosulfan, aldrin etc.), organophasphorous (methyl-, ethyl-parathion, propiconazole etc.), phenoxy acids (propxour, MCPA etc.), quatneary ammonium salts (diquat, paraquat etc.), thiocarbamate (butylate, eptam etc.) and chlorophenols (pentachlorophenol, 2,3,4-trichlorphenol etc.). Among these, sulfosulfuron, imidacloprid (IMI), methylparathion (MP) and propiconazole have been widely used as herbicide/insecticide on a variety of crops over the past two decades [54,55]. These pesticides possess variable $t_{1/2}$ (30-365 days), following natural slow degradation process and transformed into some other heteroatom containing intermediates that are sometimes reported to be more toxic than the parent compounds [54,56]. As a result, these pesticides (Fig. 1.4) have been studied for their photodegradation in soil, water with/without the use of TiO_2 as a photocatalyst and are being discussed.

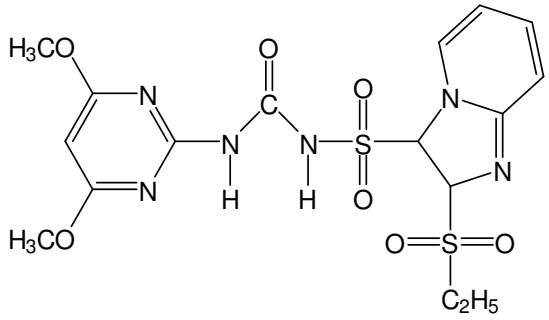

Sulfosulfuron

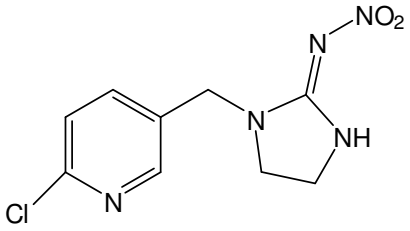

Imidacloprid

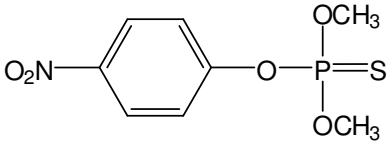

Methyl Parathion

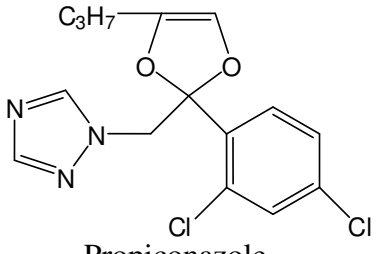

Propiconazole

Fig. 1.3 Structural formulae of studied pesticides.

1.2.1 Sulfosulfuron: It is an early-postmergent herbicide, introduced in 1982 by DuPont Crop Protection to control the isoproturon resistant *P. minor* (unwanted plant in wheat). Its degradation in wheat straw and in its grains was studied by Saha et al. [31], reporting 42% of its degradation under optimum conditions. Various identified intermediates formed during its degradation were also isolated. Ramesh et al. [32] studied the dissipation of sulfosulfuron (1 and 2 ppm) in water and suggested its $t_{1/2}$ = 67-76, and identified its metabolites (aminopyrimidine, demethyl sulfosulfuron, guanidine, sulfonamide, ethyl sulfone and rearranged amines). The study related to degradation of sulfosulfuron [33] under sunlight showed its photostability upto 115 days, and proceeds with breaking of sulfonylurea bridge, yielding different intermediates under alkaline and acidic conditions. Degradation of this pesticide in soil [34] revealed its varying half life (11-28 days) and 14% of its residual amount was determined after 120 days of direct sun light exposure. A very recent report [35] on photocatalytic oxidation of sulfosulfuron (5 ppm) showed its 40% removal after 60 min of UV-light exposure in presence of bare P25, however in presence of P25 and $Na_2S_2O_8$ its disappearance from solution becomes 80% after same time interval and under similar reaction conditions.

1.2.2 Imidacloprid: This pesticide was introduced in 1986 by Bayer Crop-Science and has been admitted in 120 nations worldwide over 140 agricultural and horticultural cultivated plants [35a]. Redlich et al. [35b] studied degradation of imidacloprid in aqueous solution under stimulated solar irradiation and found its $t_{1/2}$ to be 3 days, while some of identified degraded intermediates of the same were more persistent ($t_{1/2}$ upto 660 days) than the imidacloprid itself toward their decomposition. However, Liu et al. [36] reported its $t_{1/2}$ = 30 min when its aqueous solution was irradiated under UV-light in presence of P25. Kitsiou et al. [37] used P25 in relation to P25/Fe^{+3}/H_2O_2 system for its degradation and found increase in mineralization efficiencies from 3.4 to 14.1%, respectively after its photooxidation in UV-light. Various intermediates identified were 6-chloronicotic acid, methyl-6-chloronicotinate, N-ethylformaide, dimethyl foramide, amyl nitrite and chlorine dioxide. Tang et al. [38] studied bare P25 in comparison to P25 supported on H-ZSM-15 for degradation of imidacloprid and reported decrease in $t_{1/2}$ from 215 min to 10 min, respectively. The various intermediates formed during degradation were also reported. A report by Zabar et al. [39] that takes into account the degradation of three insecticides including imidacloprid showed 19% of actual mineralization despite its complete degradation in 2 h of photooxidation by using P25 as photocatalyst under UV-light. Very recently, Changgen et al.

[40] studied $H_3PW_{12}O_4$/La-TiO_2 for the oxidative removal of imidacloprid and found it to be 5-fold more active than bare TiO_2 for imidacloprid.

1.2.3 Methyl Parathion : Pignatello et al. [41] reported the complete oxidation of MP by UV assisted fenton system and found to yield HNO_3, H_2SO_4, H_3PO_4, oxalic acid, 4-nitrophenol and dimethyl phosphoric acid as intermediate compounds. O'Shea et al. [42] demonstrated the degradation of MP and its other family members using TiO_2 as photocatalysts, revealing that their degradation can be accomplished in oxygenated aqueous solutions. The final products for this photodegradation were found to be CO_2 and phosphoric acid. Similar to this, Konstantinou et al. [43] also studied MP and its family members using aqueous suspension of TiO_2 and identified their intermediates by mass spectroscopy. Sanjuan et al. [44] described the use of 2,4,6-triphenylpyrylium ion encapsulated in Y-zeloite for the photocatalytic decomposition of MP. It was suggested that encapsulation stabilized the pyrylium ion, resulting into its comparable activity to that of P25 for the degradation of MP and was believed to work via formation of radical intermediates. Evgenidou et al. [45] studied TiO_2 and ZnO as photocatalyst for the degradation and mineralization of MP and found that activity of former is 5 times higher than later and can be increased in the presence of $K_2S_2O_8$ oxidant. Various intermediates were also detected that were suggested to be formed by oxidation, hydroxylation, dealkylation and hydrolysis of its ester group. Moctezuma and his co-workers [46] investigated the degradation of MP using P25 as a photocatalyst and suggested mechanism for its decomposition under acidic conditions which was fast and distinct than that found for alkaline conditions.

1.2.4 Propiconazole: Vialaton et al. [47] studied the influence of humic acid and water (natural and deionised) on its photostability under stimulated solar light. It was found that degradation increases in presence of humic acid and its $t_{1/2}$ were ca. to be 60±10 and 85±10 days in natural and pure water, respectively. It was suggested that its degradation proceeds via. photocyclization and photohydrolysis routes. Pliego et al. [48] elucidate the use of high temperature fenton treatment for the removal of 18 pesticides including propiconazole from the waste water and optimized the conditions (pH and amount of fenton reagent) for its complete removal. This pesticide is also known to be degraded in soils [49] by hydroxylation of the n-propyl side chain and the dioxolane ring as well as with formation of 1,2,4-triazole with DT_{50} (loss of 50% of the parent) values of > 26 days under aerobic conditions at 25 °C. Another report [50] gave a range

of its soil half life of 40-51 days in an aerobic soil under controlled conditions. In a laboratory study, degradation of propiconazole and three other pesticides in four different types of soils showed it to be more persistent than the other pesticides, which was dependent upon the soil properties [51]. In laboratory studies on the, formation and loss of bound residues of propiconazole in soils, Kim et al. [52] showed its $t_{1/2}$ ~ 315 days in sandy loam soil, but was beyond the experimental time limit for silty clay loam soil. In a very recent report [53], the influence of ions for the degradation of Propiconazole along with 15 more pesticides was studied and it was found that presence of nitrate ion accelerates its rate of degradation while bicarbonates retards the same by scavenging hydroxal radicals.

1.3 Polycyclic Aromatic Hydrocarbons: It is a class of environmental pollutants that are formed [116-120] largely by the incomplete combustion and crop residue burning is one of its major sources in soil. These are found primarily in soil [60,61], sedements [62], oil [63] and air [64]. Among variety of PAHs, 16 are of special concern and some of these are found to be carcinogenic [60-64]. Studies have shown that humans are exposed to these PAHs and about 90% of PAHs intake comes from food [64], thereby making them another environmental pollutnat that should be minimized. Indeed, there are number of PAHs but two PAHs namely naphthalene (2 ring) and anthracene (3 ring) are initially formed during the combustion of agriculture waste [66] and therefore are considered in the present study.

The literature about naphthalene oxidation by photocatalysis showed its transfpormation into various compounds (naphthols, naphthoquinones etc.,) that finally mineralized to CO_2 and H_2O. Indeed, number of authors [17-20] used cosolvents (acetonitrile, ethanol etc.) which help in dissolution of naphthalene, but at the same time alters the rate for its photooxidation. The investigation related to the role of non-ionic surfactants [21] and organic contaminants [22] during its photodegration in presence of P25 suggested that hydroxal scavenging molecules reduced the rate of its degradation. Hykrdova et al. [19] studied the influence of quantum sized TiO_2 nanoparticles for the degradation of naphthalene and proposed a mechanism for its degradation, initiated by the attack of hydroxyl radicals. The role of photonic flux, temperature, solution pH, amount of P25 on degradation of naphthalene was studied by Liar et al. [23]. It was revealed that its degradation proceeds via hydroxylation and ring cleavage by the action of photoproduced hudroxyl and superoxide radicals. In a very recent report [24], the simultaneous degradation and hydrogen formation under inert conditions from aqueous solution of

naphthalene (5-20 ppm) was studied using P25 as a catalyst at pH = 3-8 under the UV-light irradiation. The degradation process was found to follow pseudo-first-order kinetics. The conditions (air flow, catalyst dose and UV-light intensity) for photooxidation of naphthalene in a batch reactor using slurry of P25 were optimised by Mahmoodi et al. [25] which were found to be in correlation with the theoretical predicated conditions. Ohno et al. [26] studied the influence of crystal phases of TiO_2 for the degradation of naphthalene. It was demonstrated that synergetic effect between anatase and rutile always improved the PCA of TiO_2 than any of these phases alone. The comparative photocatalytic (P25 as catalyst) and electrochemical degradation of anthracene along with four other PAHs in aqueous medium was studied by Cordeiro et al. [27]. It was proposed that photocatalytic degradation is initiated by hydroxyl radicals, while the direct electron transfer from adsorbed PAH to the electrode, activated the electrochemical oxidation. The mechanism involved during the photodegaration of anathracene in presence of P25 was proposed by Theurich et al. [28] and further verified by the work of Dass et al. [29]. Both of these reports indicated the attack of oxygenated radicals for the photooxidative transformation of anthracene into other intermediates. Woo et al. [30] demonstrated the degradation of naphthalene, anthracene and three other PAHs using P25. It was suggested that presence of aceteone as a cosolvent increased the solubility of these PAHs but after adding ~16% of it, significant alteration in the mechanism for degradation of naphthalene and anthracene was observed. It was also shown that attack site for reactive free radicals on the PAHs were dependent on localization energies of the different positions of compound.

Thus, it is clear from the above studies that the PCA of TiO_2/P25 used for degradation of aforementioned pesticides and PAHs is either slow/requires higher time for complete mineralization. Hence, there is a scope to increase PCA of TiO_2, and can be achieved by its modifying size and shape, since at nanoscale the properties (optical, electronic etc.) becomes dependant on these parameters.

1.4 Size, Shape and Surface modifications of TiO_2

It has been revealed from the studies that decrease in the size of TiO_2 nanoparticles lead to the change in the position of CB and VB to higher and lower values, respectively (Fig. 1.2) causing widening of E_g and is well known as quantum confinement [1,2,4,5,8,10]. As a result of this variation in positions of CB and VB, considerable change in the recombination of e^-/h^+ pair and hence in the PCA of TiO_2 was observed. Moreover, the S_{BET} and surface-to-volume ratio

dramatically increases as the size of a material decreases [1,2] as depicted in Fig. 1.2. For instance, Zhang et al. [67] studied the PCA of four sizes (~7, 15, 30 and 45 nm) of spherical TiO_2 nanoparticles on the decomposition of 2-propanol, and found that 7 nm particles showed 1.6 times better PCA than commercially available P25. Anpo et al. [68] investigated the PCA of TiO_2 nanoparticles on hydrogenation reactions of CH_3OH with H_2O, and observed increase in PCA with decrease in the diameter of the TiO_2 particles, especially below 10 nm.

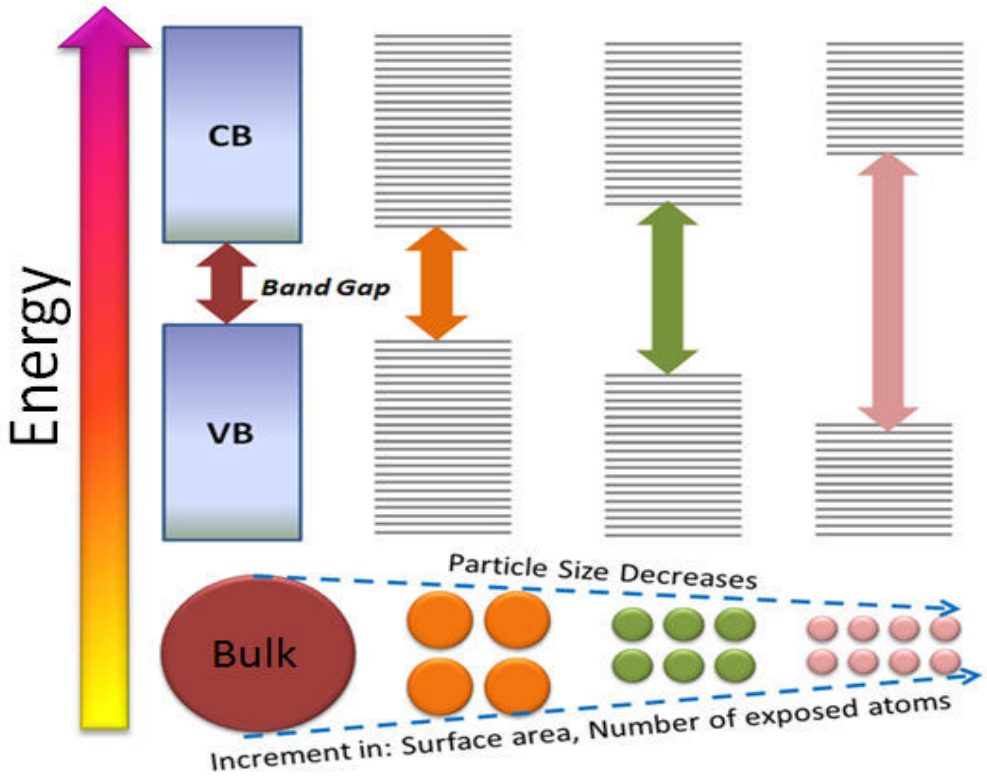

Fig. 1.2 Influence of decrease in particle size on band gap and other physical properties

However, by alternation in shape of TiO_2 such as by making anisotropic TiO_2 nanomaterials such as nanorods (TNR), nanotubes or nanowires (TNW) etc., have advantages with respect to the less recombination because of the short distance for diffusion of charge carrier [1,2,69-74] and delocalization of photoexcited electrons along their length. For example, Wang et al. [75] with favor from other reports [76,77] showed 10-70% higher PCA of rutile TNR for photooxidation of rhodamine-B. Testino et al. [78] showed superior activity of anatase TNR particles than rutile TNR and P25 particles for the degradation of phenol. They also found

comparatively higher activity of mixed phased (anatase and rutile) TNR particles than TNR with any of pure phase alone. Similarly, nanotubes because of its enhanced surface area, layered structure and of small wall thickness have also been often studied and found to exhibit higher PCA for degradation of the dyes [79-83]. For example, Zhu et al. [41], Antonio et al. [42] and Kim et al. [43] showed that the nanotubes prepared NaOH hydrothermal route exhibited 2-18 times higher PCA than P25 for the photooxidation of sulforhodamine, RB-69, rhodamine-B dyes, respectively. In a similar way TNW with its anatase and rutile phase is proven to show higher (~1.5-7.0 times) PCA than P25 for photooxidation of the toluene [85], methyl orange [86] and for H_2 formation [87] by water splitting. The improved activity of TNW was ascribed to its higher surface area and delocalization of photoexcited electrons. A report by Liu et al. [69] demonstrated the formation of mixed phase (brookite-anatase) TNW having PCA double than TNW with any of these phases alone. They indicated the improved charge migration as a cause for their higher activity toward the degradation of methyl orange. The PCA of these anisotropic structures have been also found to improve [88-100] after loading of metals (Ag, Au, Cu, Pt, Rh etc.) that were studied for the decomposition of dyes. For instance, loading of Au and Ag onto nanotubes [91] and TNW [91-100] was reported to increase rate of photooxidation and photooxidation of CO and methylene blue, respectively, and was ascribed to the decrease in excited charge recombination process.

Additionally, increase in the surface area of TiO_2 could also facilitate in the improvement in its PCA by favoring the adsorption of the reacting molecule on its surface. In this connection, the surface area of TiO_2 nanoparticles has been found to generally increase by attaching it to inert silicon dioxide (SiO_2). The relevant examples consider the incorporation of P25 particles into mesoporous silica and the use of this composite material for the photooxidation of β-naphthol [101], methylene blue [102], rhodamine-6G [103], propyzamide [104] and propionaldehyde [105]. However, the thickness of the silica shell is a crucial parameter that needs to be control while optimizing the PCA of TiO_2 nanoparticles coated by SiO_2, since over coating by SiO_2 reduces the light reaching the surface of TiO_2, ultimately decreasing the formation of e^-/h^+ pair and hence PCA. For example, in a recent report of Nussbaum et al.[106] it was suggested that SiO_2 layer of thickness < 1 nm can enhance the activity of P25 for oxidation of salicylic acid than its bare analogy, while layer of same ~2-3 nm can deteriorate its PCA under the similar experimental conditions.

Thus, it is clear from the aforementioned studies that by changing the sie, shape, loading of noble metal over it and/or coating by SiO_2 of suitable thickness improves the PCA of titania nanoparticles that have been manily studied for degradtion of dyes and can be used for the oxidative removal of other organic molecules such as pesticides and PAHs.

1.5 Research Gaps

Thus, literature revealed that most of the studies for photocatalytic degradation of pesticides and PAHs have been carried out with TiO_2 nanoparticles (other than anisotropic shape) or P25. However, it suffers from some drawbacks such as UV-light activity of TiO_2, slow rate for degradation of pesticides and PAHs, transformation of one intermediate into another which are sometimes more toxic and persistent than parent molecule and low percentage of mineralization. Therefore, any improvement in the photocatalytic activity of TiO_2 for degradation of aforementioned molecules is highly desirable and can be achieved by the following ways:

(i) Altering size and shape of TiO_2, causing improved electronic and optical properties.

(ii) Loading noble metal(s) on these different size and shaped nanoparticles that will further improve their charge dynamics.

(iii) Coating of a thin layer of porous SiO_2 over TiO_2 improves S_{BET} of TiO_2 and thereby adsorption efficiency of reacting molecules. The SiO_2 being inert and transparent to light would neither affect reacting molecules nor inhibit penetration of light reaching TiO_2. Moreover, it would also prevent aggregation of TiO_2 particles and provide a uniform well separated and dispersed TiO_2 nanoparticles that could deliver high PCA.

Although, these modified TiO_2 nanoparticles exhibiting higher photocatalytic activity than unmodified part have been well considered for photdegradation of environmental pollutants such as dyes, yet it has been rarely studied for photodecompostion of pesticides and PAHs. Moreover, no information is available regarding the role (if any) of heteroatom(s) present in the pesticides towards rate of their photooxiadation, formation and stability (i.e., $t_{1/2}$) of their photoproduced intermediates and final fate of the heteroatoms after complete degradation using these modified TiO_2 nanoparticles.

1.6 Keeping in view above resarch gaps the objective are:

1. Synthesis of various sizes and shapes of TiO_2 nanoparticles.

2. Studies of photocatalytic detoxification of some pesticides and polycyclic aromatic hydrocarbons.

3. To study the enhancement of photocatalytic activity by loading of certain metals.

4. Comparative study of photocatalytic activity between Degussa P-25 and prepared TiO_2 of different morphologies.

5. Effect of silica coating on the photocatalytic activity of TiO_2 nanostructures.

1.7 References:

[1] X. Chen and S.S. Mao, *Chem. Rev.*107 (2007) 2891-2959

[2] K. Nakata and A. Fujishima, *J. Photochem. Photobiol. A Chem. Rev.,* 13 (2012) 169-189.

[3] F. M, Arriaga, S. Esplugas and J. Gimenez, *Water Res.,* 44 (2010) 589-595.

[4] S. K. Kansal, P. Kundu, S. Sood, R. Lamba, A. Umar and S. K. Mehta, New J .Chem. 38 (2014) 3220-3226.

[5] M.I. litter, *Appl. Cata. B: Environ.,* 23 (1999) 89-114.

[6] A.K. Sinha, S. Jana, S. Pande, S. Sarkar, M. Pradhan, M. Basu, S. Saha, A. Pal and T. Pal, *Cryst. Engh. Comm*., 11 (2009) 1210-1212.

[7] S. Sood, S.K. Mehta, A. Umar and S.K. Kansal, *New J.Chem.* 38 (2014) 3127-3136

[8] A. Naldoni, M. D'Arienzo, M. Altomare, M. Marelli, R. Scotti, F. Morazzoni, E. Selli and V. Dal Santo, *Appl. Catal. B Environ.,* 130-131 (2013) 239-248.

[9] M.V. Dozzi and E. Selli, *Catal. Today*, 206 (2013) 26-31.

[10] C. Bernardini, G. Cappelletti, M.V. Dozzi and E. Selli, *J. Photochem. Photobiol. A Chem.*, 211 (2010) 185-192.

[11] I.S. Grover, S. Singh and B. Pal, *Appl. Surf. Sci.*, 280 (2013) 366-372.

[12] C.H. Lin, C.H. Lee, J.H. Chao, C.Y. Kuo, Y.C. Cheng, W.N. Huang, H.W. Chang, Y.M. Huang and M.K. Shih, *Catal. Lett.,* 98 (2004) 60-66.

[13] H.L. Kuo, C.Y. Kuo, C.H. Liu, J.H. Chao and C.H. Lin, *Catal. Lett.*, 113 (2007)7-12.

[14] I.S. Grover, S. Singh and B. Pal, *J. Nanosci. Nanotechnol.,* doi:10.1166/jnn.2014.9072

[15] F.C. Lizana, S.G. Quero, H. Idriss and M.A. Keane, *Catal. Sci.Technol.,* 1 (2011) 652-661.

[16] F.C. Lizana, S.G. Quero, H. Idriss and M. A. Keane, *J. Catal.,* 268 (2009) 223-234.

[17] J. Jia, T. Ohno, Y. Masaki and M. Matsumura, *Chem. Lett.,* 28 (1999) 963-964.

[18] F. Soana, M. Sturini, L. Cermenati, A. Albini, *J. Chem. Soc., Perkin Trans.,* 24 (2000) 699-704.

[19] L. Hykrdova, J. Jirkovsky, G. Mailhot and M. Bolte, *J. Photochem. Photobiol. A Chem.,* 151 (2002) 181-193.

[20] T. Ohno, K. Tokieda, S. Higashida, M. Matsumura, *Appl. Catal. A,* 244 (2003) 383-391.

[21] E. Pramauro, A.B. Prevot, M. Vincenti and R. Gamberini, *Chemosphere,* 36 (1998) 1523-1542.

[22] N. Barrios, P. Sivov, D. Dandrea and O. Nunez, *Int. J. Chem. Kinet.*, 37 (2005) 414-419.

[23] A. Lair, C. Ferronato, J.M. Chovelon, and J.M. Herrmann, *J. Photochem. Photobiol. A Chem.,* 193 (2008) 193-203.

[24] Y. A. Shaban, *Mod. Res. Catal.,* 2 (2013) 6-12.

[25] V. Mahmoodi and J. Sargolzae, *Desalin. Water Treat.,* (2013) doi: 10.1080/19443994.2013.861774.

[26] T. Ohno, K. Tokieda, S. Higashida and M. Matsumura, *Appl. Catal. A Gen.,* 244 (2003) 383-391.

[27] D.S. Cordeiro and P. Corio, *J. Braz. Chem. Soc.*, 20 (2009) 80-87.

[28] J. Theurich, D.W. Bahnemann, R. Vogel, F.E. Ehamed, G. Alhakimi, and I. Rajab, *Res. Chem. lntermed.,* 23 (1997) 247-274.

[29] S. Dass, M. Muneer and K.R. Gopidas, *J. Photochem. Photobiol. A Chem.,* 77(1994) 23-88.

[30] O.T. Woo, W.K. Chung, K.H. Wong, A.T. Chow and P.K. Wong, *J. Hazard. Mater.,*168 (2009) 1192-1199.

[31] S. Saha, B.S. Singh and G. Kulshrestha, *J. Environ. Sci. Health Part B*, 38 (2003) 337-347.

[32] A. Ramesh, S. Sathiyanarayanan and L. Chandran, *Chemosphere*, 68 (2007) 495-500.

[33] S. Saha and G. Kulshrestha, *J. Agric. Food Chem.,* 50 (2002) 4572-4575.

[34] A.B. Pal, S.S. Punia, Y. Ashok, and R.K. Malik, *Ind. J. Weed Sci.,* 38 (2006) 115-118.

[35] J. Fenoll, P. Sabater, G. Navarro, N. Vela, G.P. Lucas and S. Navarro, *J. Environ. Manage.,* 130 (2013) 361-368.

[35a] http://www.epa.gov/oppsrrd1/registration_review/reg_review_status.htm, Docket Number: \EPA-HQ-OPP-2008-0844, assessed on 16th June 2014.

[35b] D. Redlich, N. Shahin, P. Ekici, A. Friess and H. Parlar, *Clean*, 35 (2007) 452-458.

[36] W. Liu, W. Zheng, Y. Ma and K.K. Liu, *J. Environ. Sci. Health Part B,* 41 (2006)623–634.

[37] V. Kitsiou , N. Filippidis, D. Mantzavinos and I. Poulios, *Appl. Catal. B Environ.,* 86 (2009) 27-35.

[38] J. Tang, X. Huang, X. Huang, L. Xiang and Q. Wang, *Environ Earth Sci*., 66 (2012) 441-445.

[39] R. Zabar, T. Komel, J. Fabjan, M.B. Kralj and P. Trebse, *Chemosphere,* 89 (2012) 293-301.

[40] F. Changgen, X. Gang and L. Xia, *J. Rare Earth,* 31 (2013) 44-48.

[41] J.J. Pignatello and Y. Sun, *Water Res.,* 29 (1995) 1837-1844.

[42] K.E. O'Shea, S. Beightol, I. Garcia, M. Aguilar, D.V. Kalen and W.J. Cooper, *J. Photochem. Photobiol. A: Chem.,* 107 (1997) 221-226.

[43] J.K. Konstantinou, T.M. Sakellarides, V.A. Sakkas and T.A. Albanis, *Environ. Sci. Technol.,* 35 (2001) 398-405.

[44] A. Sanjuan, G. Aguirre, M. Alvaro and H. Garcıa, *Water Res.,* 34 (2000) 320-326.

[45] E. Evgenidoua, I. Konstantinou, K. Fytianos, I. Poulios and T. Albanis, *Catal. Today,* 124 (2007) 156-162.

[46] E. Moctezumaa, E. Leyvaa, G. Palestinoa and H. de-Lasa, *J. Photochem. Photobiol. A Chem.,* 186 (2007) 71-84.

[47] D. Vialaton, J.F. Pilichowski, D. Baglio, A.P. Perez, B. Larsen and C. Richard, *J. Agric. Food Chem.,* 49 (2001) 5377-5382.

[48] G. Pliego, J.A. Zazo, S. Blasco, J.A. Casas, and J.J. Rodriguez, *Ind. Eng. Chem. Res.,* 51 (2012) 2888-2896.

[49] T. Katagi, *Rev. Environ. Contam. Toxicol.*, 182 (2004) 1-195.

[50] A.W. Garrison, J.K. Avants and R. D. Miller, *Int. J. Environ. Res. Public Health*, 8 (2011) 3453-3467.

[51] C.W. Thorstensen and O Lode, *J. Environ. Qual.,* 30 (2001) 947-953.

[52] I.S. Kim, J.H. Shim, and Y.T. Suh, *Pest Manag. Sci.,* 59 (2003) 324-330.

[53] T. Zeng and W.A. Arnold, *Environ. Sci. Technol.,* 47 (2013) 6735-6745.

[54] M. A. Estevez, E.L. Periago, E.M. Carballo, J. S. Gandara, J.C. Mejuto and L.G. Rıo, *Agric. Ecosyst. Environ.,* 123 (2008) 247-260.

[55] S. Ahmed, M.G. Rasul, R. Brownb and M.A. Hashib, *J. Environ. Manage.,* 92 (2011) 311-330.

[56] P. Wilhelm and D. Stephan, *J. Photochem. Photobiol. A Chem.,* 185 (2007) 19-25.

[57] http://www.cseindia.org/userfiles/paper_pesticide.pdf, assessed on 22nd April, 2014.

[58] J.S. Thakur, B.T. Rao, A. Rajwanshi, H.K. Parwana and R. Kuma, *Int. J. Environ. Res. Public. Health*, 5 (2008) 399-407.

[59] http://www.soeatlas.org/PDF_Map%20Gallery/SoE%20report%20of%20Punjab.pdf, assessed on 22nd April, 2014.

[59a] http://www.appcb.ap.nic.in/faq/punj.htm, assessed on 22nd April, 2014.

[59b] A. Singh and M.I. Kaur, *J. Hum. Ecol.*, 37 (2012)133-137.

[60] M. Nadal, M. Schuhmacher and J.L. Domingo, *Environ. Pollut.,* 132 (2004) 1-11.

[61] J.J. Nam, H.B. Song, C.K. Eom, H.S. Lee and A. Smith, *Chemosphere,* 50 (2003) 1281-1289.

[62] Z. Cao, J. Liu, Y. Li and M. Ma, *Toxico. Environ. Chem.*, 92 (2010) 707-720.

[63] A. Husam, A.Z. Sameer, H. Adnan, S. Wajih, A. Nisar, G. Bondi and K. Kurunthachalam, *Food Addit. Contam. Part A*, 27 (2010) 869-878.

[64] M. Zheng and M. Fang, *Water, Air, Soil Pollut.,* 11 (2007) 175-189.

[65] B. Liu, A. Kharen and E.S. Aydil, *Applied Mater. Interfaces,* 3 (2011) 4444-4450.

[66] C. Jia and S. Batterman, *Int. J. Environ. Res. Public Health,* 7 (2010) 2903-2939.

[67] Z. Zhang, C.C. Wang and R. Zakaria, J.Y. Ying, *J. Phys. Chem. B,* 1998, *102*, 10871-10878.

[68] M. Anpo, T. Shima, S. Kodama and Y. Kubokawa, *J. Phys. Chem.,* 1987, *91*, 4305-4310.

[69] F. Dong, W. Zhao and Z. Wu, *Nanotechnology,* 19 (2008) 365607-365617.

[70] L. Ge and J. Liu, *J. Phys. Conf. Ser.,* 188 (2009) 012019-0122022.

[71] M.C. Wu, H.C. Liao, Y.C. Cho, C.P. Hsu, T.H. Lin, W.F. Su, A. Sapi, A. Kukovecz, Z. Konya, A. Shchukarev, A. Sarkar, W. Larsson, J.P. Mikkola, M. Mohl, G. Toth, H. Jantunen, A. Valtanen, M. Huuhtanen, R.L. Keiski and K. Kordas, *J. Nanopart. Res.,* 16 (2014) 2143-2154.

[72] C. Wang, L. Yin, L. Zhang, N. Liu, N. Lun and Y. Qi, *Appl. Mater. Interfaces* 2 (2010) 3373-3377.

[73] B. Wen, C. Liu and Y. Liu, *Inorg. Chem. Commun.,* 44 (2005) 6503-6505.

[74] S.S. Mandal and A.J. Bhattacharyya, *Talanta,* 82 (2010) 876-884.

[75] Y. Wang, L. Zhang, K. Deng, X. Chen and Z. Zou, *J. Phys. Chem. C,* 111 (2007) 2709-

2714.

[76] Y. Long, Y. Lu, Y. Huang, Y. Peng, Y. Lu, S.Z. Kang, and J. Mu, *J. Phys. Chem. C,* 113 (2009) 13899-13905.

[77] B. Wang, R. Karthikeyan, X.Y. Lu, J. Xuan, M.K.H. Leung, *J. Hazard. Mater.,*263 (2013) 659-669.

[78] A. Testino, I.R. Bellobono, V. Buscaglia, C. Canevali, M. D'Arienzo, S. Polizzi, R. Scotti, and F. Morazzoni, *J. Am. Chem. Soc.,* 129 (2007) 3564-3575.

[79] H. Zhu, X. Gao, Y. Lan, D. Song, Y. Xi and J. Zhao, *J. Am. Chem. Soc.,* 126 (2004) 8380-8381.

[80] A.T. Antonio, M.A.C. Jacome, S.L.O. Cerros, E.M. Palacios, R.S. Parra, C.A. Chavez, J. Navarete and E.L. Salinas, *Appl. Catal. B: Environ.,* 100 (2010) 47-54.

[81] S.J. Kim, Y.S. Lee, B.H. Kim, S.G. Seo, S.H. Park and S.C. Jung, *Int. J. Photoenergy,* (2012), doi.org/10.1155/2012/901907.

[82] J. Yu, H. Yu, B. Cheng and C. Trapalis, *J. Mol. Catal. A Chem.* 249 (2006) 135-142.

[83] C.K. Lee, C.C. Wang, M.D. Lyu, L.C. Juang, S.S. Liu and S.H. Hung, *J. Colloid. Interf. Sci.,* 316 (2007) 562-569.

[84] F, Dong, W. Zhao and Z. Wu, *Nanotechnology*, 19 (2008) 365607-365617.

[85] H. Yin, T. Lin, C. Yang, Z. Wang, G. Zhu, T. Xu, X. Xie, F. Huang and M. Jiang, *Chem. Eur. J.,* 19 (2013) 13313-13316.

[86] S. K. Parayil, H.S. Kibombo, C.M. Wu, R. Peng, T. Kindle, S. Mishra, S.P. Ahrenkiel, J. Baltrusaitis, N.M. Dimitrijevic, T. Rajh, and R.T. Koodali, *J. Phys. Chem. C*, 117 (2013) 16850-16862.

[87] B. Liu, A. Khare and E.S. Aydil, *Appl. Mater. Interfaces*, 3 (2011) 4444-4450.

[88] X. Ding, X.G. Xu, Q. Chen and L.M. Peng, *Nanotechnology,* 17 (2006) 5423-5427.

[89] X. Si, F. Li, L. Sun, F. Xu, S. Liu, J. Zhang, M. Zhu, L.Z. Ouyang, D. Sun and Y.L. Liu, *J. Phys. Chem. C,* 115 (2011) 9780-9786.

[90] D.V. Bavykina, A.A. Lapkinb, P.K. Plucinskib, L.T. Murcianob, J.M. Friedricha and F.C. Walsh, *Top. Catal.,* 39 (2006) 3-4.

[91] J.Y. Tsai, J.H. Chao and C.H. Lin, *J. Mol. Catal. A Chem.,* 298 (2009) 115-124.

[92] W. Smith, S. Maob, G. Lu, A. Catlett, J. Chen and Y. Zhao, *Chem. Phys. Lett.,* 485 (2010) 171-175.

[93] D. Kong, J.Z.Y. Tan, F. Yang, J. Zeng, X. Zhang, *Appl. Surf. Sci.,* 277 (2013) 105-110.

[94] O. Kerkez and I. Boz, *J. Phys. Chem. Solids*, 75 (2014) 611-618.

[95] Z. Zhao, J. Xu, P.K. Liaw, B. Wu and Y. Wang, *Corros. Sci.,* 84 (2014) 66-73.

[96] H. Zhang, G. Zhao, T. Zhang and F. Teng, *J. Alloy Compd.,* 603 (2014) 35-41.

[97] M.C. Wu, H.C. Liao, Y.C. Cho, C.P. Hsu, T.H. Lin, W.F. Su, A. Sapi, A. Kukovecz, Z. Konya, A. Shchukarev, A. Sarkar, W. Larsson, J.P. Mikkola, M. Mohl, G. Toth, H. Jantunen, A. Valtanen, M. Huuhtanen, R.L. Keiski and K. Kordas, *J. Nanopart. Res.,* 16 (2014) 2143-2154.

[98] C. Wang, L. Yin, L. Zhang, N. Liu, N. Lun, and Y. Qi, *Appl. Mater. Interfaces*, 2(2010) 3373-3377.

[99] W. Zhou and Y. He, *Chem. Eng. J.,* 179 (2012) 412-416.

[100] J. Jitputti, Y. Suzuki and S. Yoshikawa, *Catal. Comm.,* 9 (2008) 1265-1271.

[101] S. Qourzal, N. Barka, M. Tamimi, A. Assabbane, A. Nounah, A. Ihlal and Y.A Ichou, *Mater. Sci. Eng. C,* 29 (2009) 1616-1620

[102] F. Mei, C. Liu, L. Zhang, F. Ren, L. Zhou, W.K. Zhao and Y.L. Fang, *J. Cryst. Growth Des.,* 292 (2006) 87-91.

[103] C. Anderson and A.J. Bard, *J. Phys. Chem.,* 99 (1995) 9882-9885.

[104] T. Torimoto, S. Ito, S. Kuwabata and H. Yoneyama, *Environ. Sci. Technol.,* 30 (1996) 1275-1281.

[105] N. Takeda, T. Torimoto, S. Sampath, S. Kuwabata and H. Yoneyama, *J. Phys. Chem.,* 99 (1995) 9986-9991.

[106] M. Nussbaum and Y. Paz, *Phys. Chem. Chem. Phys.*, 14 (2012) 3392-3399.

2. Preparation and Characterization techniques of Titania nanostructures

This chapter includes the various materials and methods used for synthesis of bare and SiO_2 coated/metal-loaded titania/titanate nanoparticles in different size and shape, various techniques used for their characterization, detailed instrumental techniques used for analyzing the photooxidised/photoreduced samples of the studied compounds and are being described.

2.1 Materials used

Methanol (AR; HPLC), Acetonitrile (HPLC), Sodium hydroxide (AR), 2-Propanol (AR), Nitric acid (AR), Ethanol (AR), Sulfuric acid (AR), Ethyl acetate (AR), Cupric nitrate (AR), Silver nitrate (AR), Chloroauric acid (AR), *m*-Dinitrobenzene (AR), *m*-Nitroaniline (AR), *m*-Phenylenediamine (AR), Naphthalene (AR) and Anthracene (AR) were purchased from Loba Chemie, India. Tetraethylorthosilicate (TEOS) and Cetyltrimethylammonium bromide (CTAB) were obtained from Sigma Aldrich. All the gases (N_2, He, He:N_2::70:30) of high purity were purchased from Sigma Gases and Services, New Delhi, India. Commercially available P25-TiO_2 was obtained as a gift sample from Evonik Corporation, Germany (formerly, Degussa Corporation Germany). Technical grade pesticides viz., Imidacloprid (IMI) and Sulfosulfuron were obtained from Markfed Pvt. Ltd. (India) while Propiconazole, Methyl Parathion (MP) were obtained from Bayer Corpartion India Ltd., as gift samples. HPLC grade water was purchased from Renchem (India). Millipore water (conductivity = 35 ohm^{-1} cm^{-1}) was used for preparing the reaction solutions and washing the catalysts.

2.2 Synthesis of titania/titanate nanostructures of different Sizes and Shapes

2.2.1 Sodium titanate nanotubes (TNT): Commercially available P25-TiO_2 was used as a precursor for the synthesis of this material. It was synthesized by a reported method [1] as follows: 4.73 g of P25-TiO_2 was mixed with 72 ml of 10 N NaOH and subjected to hydrothermal treatment at 130 ^oC in Teflon lined autoclave (80 ml capacity) for 20 h. The slurry was washed repeatedly with 0.1 N HNO_3, followed by water and methanol, and dried in a hot air oven (Navyug Q-5267) at 70-80 ^oC for 3 h.

2.2.2 TiO_2 nanorods (TNR): These nanoparticles were synthesized by autoclaving aqueous slurry (pH= 5.6) of TNT (3.2 g in 64 ml) at 175 ^oC for 48 h [1]. After hydrothermal treatment resulted slurry was filtered, washed with distilled water and methanol, and dried in hot air oven at 70-80 ^oC for 3 h.

2.2.3 Sodium titanate nanorods (TNT(S)): These were prepared [2] by calcining TNT (prepared as per *section-2.2.1*) in an alumina crucibles at 800 ^{o}C (heating rate 5 ^{o}C/min) for 2 h using muffle furnace (Jupiter Scientific).

2.2.4 TiO_2 nanowires (TNW): The TNW were synthesized [3] by dispersing TNT in dilute acid solution at pH~1 for 72 h and then subjecting to hydrothermal treatment at 200 ^{o}C for 72 h. Thereafter, the obtained slurry was washed with water followed by methanol and dried at 70-80 ^{o}C in hot air oven.

2.2.5 Thermally (> 800 ^{o}C) stable anatase TiO_2 nanoparticles (C-2 to C-9): In present study as-prepared TNR particles (*section-2.2.2*) were found to retain its crystal structure, verified by calcinning them in an alumina crucible for 2 h at 200-900 ^{o}C (heating rate 5 ^{o}C/min) using muffle furnace.

2.2.6 Titania nanopolygons (TNP_g): The TNP_g were done by calcinning the Au-loaded TNT at 800 ^{o}C for 2 h. The detailed procedure for Au-loading (specifically used for this section) is described in ***section-2.4.2*** of this chapter.

2.2.7 Silica coated TiO_2 nanoparticles (S-C-5(x)): Silica was coated by sonicating (ultrasonicator Branson-1610) 50 mg of as-prepared C-5 nanoparticles (TNR calcined at 500 ^{o}C as per *section-2.2.5*) in a mixture of ethanol (12 ml) and acetic acid (18.4 ml) for 30 min to ensure its well-dispersion in the media. Thereafter, mixture of ethanol (6.2 ml) and TEOS (10, 20 and 40 µl) was added drop-wise to the above suspension with vigorous stirring, followed by slow addition of concentrated H_2SO_4 (50-100 µl), refluxed at 80-90 ^{o}C for 1 h, washed with successive quantities of ethanol and dried. These catalysts are abbreviated as S-C-5(1), S-C-5(2) and S-C-5(4) thereafter.

2.3 Synthesis of Au-nanoparticles

These nanoparticles were prepared by seed-mediated approach at ~ 0 ^{o}C as reported by our group [4,5]. The Au seeds were first prepared by adding aqueous solution $HAuCl_4$ (0.01 M, 250 µl) to 9.5 ml of aqueous solution of CTAB (0.1 M), followed by addition (600 µl) of aqueous solution of 0.01 M $NaBH_4$ under magnetic stirring for 2 min. The growth solution was prepared by adding $HAuCl_4$ (0.01 M, 500 µl) to 9.5 ml (0.1 M) of aqueous CTAB solution with 55 µl of ascorbic acid (0.1 M). Then 12 µl of Au seed solution was added to it and the resultant nanoparticles obtained were repeatedly washed with water and used further.

2.4 Metal loading

2.4.1 Photodeposition: It was carried out [6,7] in a test tube containing de-aerated 5 ml of aqueous (50% v/v) isopropyl alcohol, 50 mg titania nanoparticles (P25, TNR, TNT, TNT(S) etc.) and required amount of aqueous metal salt ($AgNO_3$, $Cu(NO_3)_2$ and $HAuCl_4.xH_2O$) solution under UV light (125 W Hg arc lamp = 10.4 mW/cm^2) irradiation for 2 h. The metal ions (Au^{+3}, Ag^+ and Cu^{+2}) present in titania slurry were reduced to elemental state by its photoexcited electrons and metal nanodeposits were formed throughout the surface. The catalysts thus obtained were repeatedly washed with water and methanol, dried at 70-80 ^oC and used further for the photocatalytic reactions.

2.4.2 Au-loading onto TNT used for synthesis of TNP_g (section 2.2.6): It was carried out by three methods (i) by adding $HAuCl_4.xH_2O$ (1.2 ml of 0.01 mM aqueous solution = 0.5 wt% of Au) during the preparation of TNT (*section-2.2.1*), which was (ii) irradiated in de-aerated 5 ml of 50% v/v aqueous isopropyl alcohol under UV light (125 W Hg arc lamp) for 2 h, as a result Au^{+3} was reduced [6] to Au^o (TNT- Au^o(P)), and (iii) by mixing of TNT (100 mg) in 3 ml of H_2O with 500 µl spherical Au nanoparticles (NP, size 3-5 nm) under stirring for 2 h followed by drying.

2.5 Characterization

Aforementioned catalysts were characterized by different techniques and are being described as under:

2.5.1 X-Ray Diffraction (XRD): This technique was used in the present research work to study the phase composition, structural variations and crystallinity of the as-prepared samples. Crystallite size was calculated by Scherrer's equation $d = k\lambda/\beta Cos\theta$, where d = crystallite size, λ = X-ray wavelength, k = constant, θ is diffraction angle and β is full width at half maxima of the diffraction line. Stain in the nanoparticles was determined using Williamsons-Hall's model, by calculating the slope of line obtained by plotting ***$\beta Cos\theta$ vs $4Sin\theta$***, where symbols have their usual meaning and units, except θ which was converted in radians. This study was carried out on Panalytical X'-pert Pro, at Sophisticated Analytical Instrumentation Laboratory (SAI-Lab), Thapar University, Patiala, India. The relative percentage of crystal structure was calculated by X'pert High Score Plus software.

The lattice parameters of various crystal structures in as-prepared catalysts were calculated by the following equations:

(a) For Orthorhombic crystal structure:

$$\frac{1}{d^2} = \frac{h^2}{a^2} + \frac{k^2}{b^2} + \frac{l^2}{c^2}$$

(b) For Monoclinic crystal structure:

$$\frac{1}{d^2} = \frac{1}{\sin^2\beta}\left(\frac{h^2}{a^2} + \frac{\sin^2\beta\, k^2}{b^2} + \frac{l^2}{c^2} - \frac{2hl\cos\beta}{ac}\right)$$

Where, $\beta = 90.3000^{\circ}$ (for $Na_2Ti_6O_{13}$, as per ICSD Card No. 01-073-1398)

$= 105.0000^{\circ}$ (for $Na_2Ti_9O_{19}$, as per ICSD Card No. 01-073-2256)

$= 101.9000^{\circ}$ (for $Na_2Ti_3O_7$, as per ICSD Card No. 00-014-0085)

(c) For Rhombohedral crystal structure:

$$\frac{1}{d^2} = \frac{(h^2 + k^2 + l^2)\sin^2\alpha + 2(hk + kl + +hl) - (\cos^2\alpha - \cos\alpha)}{\alpha^2(1 - 3\cos^2 + 3\cos^3)}$$

Where, $\alpha = 90.0000^{\circ}$ (for $NaTiO_2$, as per ICSD card No. 00-016-0251)

(d) For Tetragonal crystal structure:

$$\frac{1}{d^2} = \frac{h^2 + l^2}{a^2} + \frac{l^2}{c^2}$$

The symbols used in above equations for different crystal structures are referred as:

a, b, c	=	lattice parameters which were calculated
h, k, l	=	Miller indices
d	=	spacing and is known as d-spacing

2.5.2 SEM/FE-SEM coupled to EDS: It was used to study the external morphology and relative amount (atom % = at.% or weight % = wt%) of the constituents of as-prepared catalysts. The SEM analysis was done using JSM 7600F at SAI-Labs, Thapar University, Patiala, India; while FE-SEM analysis was carried out on JEOL JSM-6510LV at Sophisticated Analytical Instrumentation Facility (SAIF) center, IIT Bombay, India.

2.5.3 TEM: This technique allows imaging of individual particle and to some extent to evaluate the finest structural details and statistical distribution of sizes and shapes of particles in the sample. Prior to this analysis, samples were dispersed in methanol by sonicating the suspension for ~ 5 h, thereafter a drop of suspension was put on copper grid coated with carbon and analyzed for Tem. This analysis was performed at National Institute for Pharmaceutical Education and Research, Mohali, India; SAIF centre, IIT-Bombay, India and SAIF centre, Panjab University, Chandigarh, India, using Hitachi 7500 (2.0 Å, 120 KV), Phillips CM-200 (2.4 Å, 200 KV) and FEI Tecnai G2 F20 (2.4 Å, 300 KV), respectively.

2.5.4 Zeta potential (ζ): It is an indicator for the stability of a colloidal suspension, and its magnitude reveals the degree of electrostatic repulsion between adjacent, similarly charged particles in dispersion. This study was performed on Brook heaven 7610 using 2.5 ml aqueous TNP slurry (0.13 mg/ml).

2.5.5 Surface Charge: This analysis was performed on Mutek-PCD03pH using 50 ml aqueous slurry (0.6 mg/ml) of different titania/titanate nanostructures at Thapar Center for Industrial research and Development, Yumunanagar, India.

2.5.6 Diffuse Reflectance Spectroscope (DRS): It was performed (Ocean optics 4000USB) to determine the reflectance/adsorption of the as-prepared catalyst in the UV/visible region, and for determination of their Eg. The band gap was calculated [3] using the Tauc equation; $(\alpha h\nu)^n = h\nu - E_g$, where, ν is frequency, h is Plank's constant and n = 0.5 for indirect semiconductor, α is absorption coefficient and E_g is the band gap energy.

2.5.7 Time Resolve Photoluminescence Decay: The time resolve photoluminescence spectra was measured by the pulse excitation method using Nitrogen laser (excitation at 390 nm) pulsed in operation (5-7 ns pulse width) coupled with Tektronix TDS-1012 oscilloscope. The average lifetime (τav), is related to band edge lifetime τ_1 and trapping or defect's states given by the following equation [5],

$$\tau_{av} = (a_1\tau_1 + a_2\tau_2) / a_1 + a_2$$

where, a_1 and a_2 denote the amplitude of band edge excitonic and trapping state emission, respectively.

2.5.8 Raman Spectra: This technique used for structural information of the material was obtained (100 to 800 cm^{-1}) on Renishaw system (2000 spectrometer) using He–Ne laser (operating at 514.5 nm) at SAIF-Jawaharlal Nehru University, New Delhi, India.

2.5.9 Dynamic Light Scattering (DLS): it was used to provide the particle size distribution, carried out with Brookheaven-7610 particle size analyzer using 2 ml of aqueous dispersion of (2 mg/10 ml) of TNT and TNR after 30 min sonication.

2.5.10 Surface Area: The determination BET surface area (S_{BET}) was performed on Smart Sorb 90/91, using 150 mg of sample, preheated at 150 ^oC for 1 h.

2.5.11 FT-IR: This study was carried out in Agilent Carry-600 FT-IR spectrometer by placing the pellet made from sample (~1-2 mg) and 100 mg KBr (dried at 90-100 oC for 3 h).

2.6 Photocatalytic activity

2.6.1 Photooxidation: The rubbed capped tight test tube having aqueous solution of pesticides/PAHs and catalysts was irradiated under UV- or Sun-light and summarized in table 2.1.

2.6.2 Photoreduction: A rubber capped test tube containing de-aerated 50% (v/v) isopropyl alcoholic solution of *m*-Dinitrobenzene (*m*-DNB) was irradiated under UV-light (125 W Hg-arc lamp) using various as-prepared catalysts (Table 2.1).

Table 2.1 Different molecules studied for photooxidation/photoreduction using various catalysts

S. No	Substrate studied	Concentration/ Amount used	Catalyst used; Amount (mg/5ml)
1	IMI	25 and 50 ppm	Bare P25, TNT, TNR, Ag (0.2-1.0 wt%) photodeposited TNT and TNP_g; 2.5
2	Sulfosulfuron	1000 ppm	P25, TNT and TNT(S); 50
3	*m*-DNB	25 µmol	Bare and Au (0.5 and 2.0 wt%) photodeposited P25, TNT and TNT(S); 50
4	MP	50 ppm	P25, TNR (calcined at 200-900 ^oC) and their Au (1 wt%)-photodeposited analogies; 5
5	*Propiconazole	50 ppm	P25, bare and 1 wt% Au-photodeposited TNW; 5
6	Naphthalene	20 ppm	P25, bare and SiO_2 coated C-5; 5
7	Anthracene	20 ppm	-do-

** Also studied under sun-light of flux = 9.2 mW/Cm^2 on 08-06-2014 from 10:00 am to 4:00 pm*

The reaction solutions obtained after photooxidation/photoreduction were analyzed by different techniques and are being described:

2.6.3 UV-Visible Spectrophotometer: The reaction solution having MP, propiconazole, naphthalene and anthracene were analyzed using this instrument **(Champion)**.

2.6.4 High Performance Liquid Chromatography (HPLC): The reaction solution obtained after photooxidation of pesticides (IMI, Sulfosulfuron); reduction of m-DNB were analyzed by HPLC (Agilent LC 1120) technique in reverse phase, at ambient temperature using C-18 column (BDS, Qualigens) of dimensions 250 mm × 4.6 mm, and particle size of 5 µm. The optimized mobile phase and wavelength during the analysis is summarized in Table 2.2.

Table 2.2 The optimized HPLC conditions for studied molecules

S. No	Analyte	Mobile Phase (@1 ml/min)	λ (nm)
1	IMI	acetonitrile : water :: 80:20	270
2	Sulfosulfuron	methanol : water :: 70:30	254
3	*m*-DNB	methanol : water :: 70:30	270

2.6.5 Gas Chromatograph (GC): This technique was used to study CO_2 evolution during the photooxidation of studied pesticides and PAHs. It was determined by injecting 1 ml of gaseous mixture from the reaction vessel (gas tight test tube) into GC (NUCON-5765) equipped with Thermal Conductivity Detector (TCD) and Porapak-Q column having flow of nitrogen (30 ml/min) as carrier gas. Column oven was maintained at 40 ^{o}C while injector and detector were isothermally kept at 70 and 80 ^{o}C, respectively.

2.6.6 GC (45X GC) coupled to Mass Spectrometer (MS, MS-Scion-45P): This technique was used to identify the intermediates formed during the photooxidation of studied pesticides and PAHs. The reaction solution (3 ml) of pesticide and PAHs obtained after photodegradation were prepared by filtering (cellulose filter 0.22 µm), extracting (with ethyl acetate, 3 × 3 ml) and then evaporating to dryness over rota-evaporator (Hedloph). Residue was dissolved in ethyl acetate (1 ml) and injected (1µl) to HP-5MS column (15m × 0.25 mm × 0.25 µm) with flow rate of 1ml/min of Helium gas. The injector and transfer line were isothermally kept at 250 ^{o}C and

275 ^{o}C, respectively. The oven was programmed from 60 ^{o}C to 300 ^{o}C @ 6 ^{o}C/min rise of temperature for MP, naphthalene, anthracene and m-DNB; 60 ^{o}C (5 min hold) to 240 ^{o}C@6 ^{o}C for IMI and propiconazole.

2.6.7 Ion chromatograph (IC): In order to determine the fate of heteroatoms present in IMI, this technique was used by injecting the reation solution in Waters's system equipped with a Waters 501pump, a Waters 431chemical conductivity detector, ion pack Metrosapp A Supp column (250 mm × 4.0 mm, 5 mμ) using methanol: water :: 60:40 as mobile phase @ 0.6 ml min^{-1} at Thapar Center for Industrial Research and Development, Yumunanagar, India.

2.6.8 Liquid Chromatograph-Mass Spectrometer (LC-MS): It was performed by injecting 20 μl of reaction sample in LC-MS (Bruker-300PS) having single-quadruple detector, equipped with C-18 column (Hypersil, 150 mm× 4.6 mm, 5 μm) using a mobile phase of 80:20:: acetonitrile : water at a flow rate of 1 ml/min at SAIF center, Panjab University, Chandigarh, India.

2.6.9 Kinetic Analysis: In present study the degradation of the studied molecules was found to follow pseudo-first order kinetics which is mathematically represented as

$$-\ln(C/C_0) = k \times t$$

Where; C_0 = initial concentration of the molecule, C = concentration of the molecule in solution at any time t, k = apparent rate constant (min^{-1}, obtained from slope of graph plotted $-\ln(C/C_0)$ vs t).

The half-life ($t_{1/2}$) of the studied molecules (wherever applicable) was calculated by the following:

$$t_{1/2} = 0.693/k$$

Where, symbols have their usual meaning.

The dark adsorption studies for naphthalene and anthracene using bare and silica coated catalysts was found to fit in the pseudo-second order kinetics as given below:

$$\frac{t}{q_t} = \frac{1}{k_2 \times (q_e)^2} + \frac{t}{q_e}$$

Where, t = contact time, q_e = adsorption capacity at equilibrium, q_t = adsorption capacity per unit mass of catalyst at time t, k_2 = rate of reaction (g mg^{-1} min^{-1}) and was calculated by intercept of graph between t and t/q_t.

2.7 References

[1] J.N. Nian and H. Teng, *J. Phys. Chem. B,* 110 (2006) 4193-4198.

[2] M. Qamar, C.R. Yoon, H.J. Oh, N.H. Lee, K. Par, D.H. Kim, K.S. Lee, W.J. Lee and S.J. Kim, *Catal. Today,* 131 (2008) 3-14

[3] X. Chen and S.S. Mao, *Chem. Rev.*107 (2007) 2891-2959.

[4] R. Kaur and B. Pal, *J. Mol. Catal. A. Chem.* 355 (2012) 39-43.

[5] S. Kumar, Ghosh and T. Pal, *Chem. Rev.*107 (2007) 4797-4862.

[6] I. S. Grover, S. Singh and B. Pal, *Appl. Surf. Sci.* 280 (2013) 366-372.

[7] I. S. Grover, S. Singh and B. Pal, *RSC Adv.,* 4 (2014) 27704-27709.

3. Preparation, surface morphology, electro-kinetic and photocatalytic properties of titania nanostructures of different shapes

3.1 Introduction

The PCA of TNP is well proven to be influenced [1–10] by the crystal structure, surface area, band gap energy, size, shape, crystallinity and noble metal loading etc. Extensive research is still going on to find out better photoactive materials than mostly used P25 catalyst, possessing limitation of photosensitivity in the UV range and crystal phase selective activity [3,5]. In this context, different TiO_2 shapes and other titania based composite nanostructures have attracted a great deal of research interest [11–15] due to their structural, surface and morphological advantages. For example, lengthy cylindrical titania nanorods, and nanotubes [7–9,12,13] exhibited high photocatalytic activity relative to P25 particles due to better delocalization of excited e^-/h^+ pairs and well developed space charge region that reduced the recombination time of photogenerated charge species.

Nowadays, TNT and TNR morphologies [7–9,12–18] display flexible photoactivity depending on their crystal phase composition, geometric morphology, surface area, thermal treatment and sodium content that generally deteriorate [18] the PCA of TiO_2. For example, Zhu et al. [9], Antonio et al. [14] and Kim et al. [15] found that the TNT without calcinations exhibited decent photocatalytic activity, but many other reports demonstrated almost negligible photoactivity [16–18] when sintered below 300 ^oC. In contrary, higher [3,7,8] and lower [12,13,16–18] PCA of TNR than P25 catalyst is also reported in many photocatalytic reactions. To understand this inconsistency in PCA of TNP, TNT and TNR catalysts, many essential physico and electro-kinetic properties [19,20] such as, surface charge and zeta potential (ζ) responsible for affecting the adsorption or interaction of polar or non-polar reacting substrates, depending upon the net surface charge present over suspended titania particles in photoreaction mixture is needed to study in correlating and fine-tuning the PCA of various TNP catalysts. For instance, a large values of ζ (positive or negative) indicates less agglomeration, i.e. more particles will be available for adsorption of substrate molecules and thus, control the interfacial properties of TNP catalysts and hence, the PCA [19,20]. These electro-kinetic parameters can be tuned by altering the synthetic procedure, varying the surface area depending on the nature and

dimension of photocatalyst and amount of metal loading that may hinder the surface charge distribution and ζ of TiO_2 aqueous dispersion [19–23]. Although, some reports [19,20,24] have demonstrated the effect of metal (Ag, Pd and Cu) doping in either TiO_2/SiO_2 or the metal (Ag and AgNi) core-TiO_2 composites on the development of ζ, yet no information is available regarding the nature of electro-kinetic parameters of coinage metal (Au, Ag and Cu) deposited TNP of different shapes although these M-TNP catalysts have recently been widely used for efficient photocatalytic reactions [3–6,20,24]. In this respect, the present research is aimed to determine the surface area, surface charge and ζ of bare and coinage metal (Ag and Cu) deposited as-prepared hollow porous-TNT and compact rigid-TNR as compared to P25 for the photocatalytic oxidation [25,27–30] of IMI insecticide, used to control the pests in agriculture crops that is toxic to insect's nervous system [26]. This insecticide is being used over varieties of crops throughout the world (half life 40–50 days), with high solubility (550 mg/l) in water [25] causing soil and water contamination and posturing treat to humans [26]. This chapter discusses the possibility to minimize/remove its contamination through a green remediation pathway resembling TiO_2 photocatalysis.

3.2. Experimental section

3.2.1 Synthesis and Characterization of bare and metal (Ag, Cu) loaded TNT and TNR nanoparticles: The bare TNT and TNR were synthesized as per procedures discussed in *section-2.2.1* and *section 2.2.2* of chapter 2, respectively. Metal loading onto these nanoparticles was carried out by photodeposition route as discussed in *section-2.4.1* of chapter-2. These as-prepared catalysts were characterized by XRD (*section-2.5.1*), SEM coupled to EDS (*section-2.5.2*), TEM (*section-2.5.3*), Zeta Potential (*section-2.5.4*), Surface Charge (*section-2.5.5*) and S_{BET} (*section-2.5.10*) techniques, discussed in chapter-2.

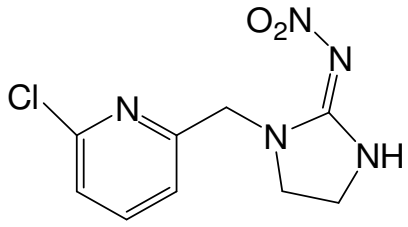

Structure of imidacloprid.

3.2.2 Photocatalytic Activity: Photodegradation of IMI was studied as per procedure given in *section-2.6.1* (chapter-2) by monitoring decrease in concentration of IMI and corresponding CO_2 formation, monitored through HPLC (*section-2.6.2*) and GC (*section-2.6.3) of* chapter 2, respectively.

3.3 Results and discussions

The E_g of TNT, TNR and P25, have been calculated (Fig. 3.1), using the Tauc equation (*section-2.5.7*). The measured E_g for TNR (3.26 eV) and P25 (3.12 eV) are in good agreement [3,7,8] with 3.2 eV of anatase phase of TiO_2. However, E_g (3.43 eV) of TNT was lowered by 0.17-0.44 eV as observed in reported findings [32,33]. The blue shift of E_g ca. 0.31 eV of TNT as compared to 3.12 eV of P25 occurs due to the hydration and quantum size effect of TNT, discussed by Wang et al. [33] in their investigation.

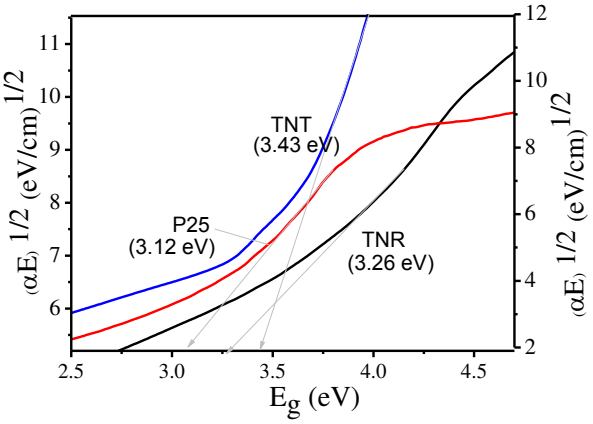

Fig. 3.1 Band gap energy of various catalysts.

The XRD patterns of TNT and TNR in comparison to P25 nanoparticles are shown in Fig. 3.2. The TNT prepared by alkali treatment of P25 show crystallographic planes viz., (110) and (020) corresponding to 2θ = 24.05° and 48.07°, that resemble [31] with diffraction pattern of orthorhombic $Na_2Ti_2O_5{\cdot}H_2O$ [33] crystal structure. The calculated lattice parameters, a = 22.36 Å, b = 3.75 Å and c = 2.99 Å (*section-2.5.1 of chapter-2*) are found to deviate [33] with the literature values a = 19.36 Å, b = 3.78 Å and c = 3.00 Å and could be ascribed to increase in size of TiO_6 octahedral units during acid washing [9]. The $Na_2Ti_2O_5{\cdot}H_2O$ comprise of two dimensional layers in which TiO_6 octahedras combine, and the protons are present in between the layers through the edge sharing [33]. However, all the crystallographic planes of as-prepared TNR (Fig. 3.2) were found to correspond with anatase

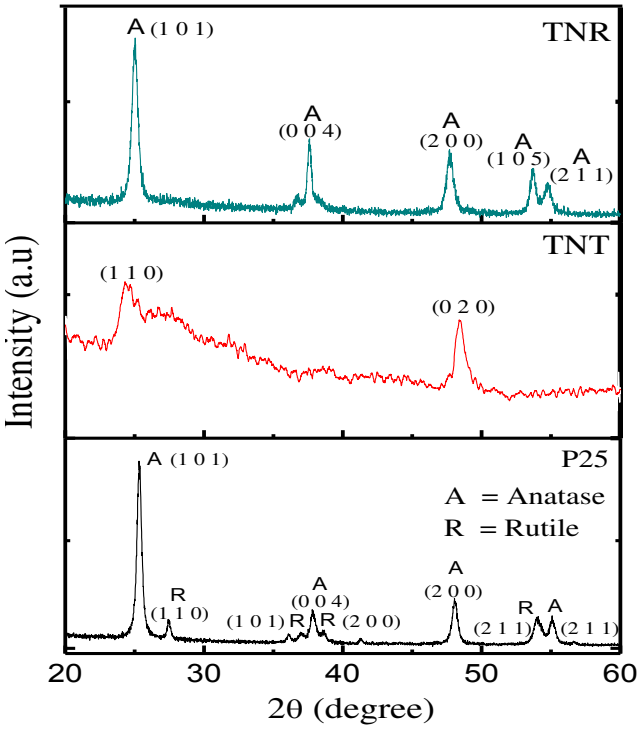

Fig. 3.2 Comparative XRD patterns of various catalysts.

phase (JCPDS 21-1272) and are in accordance with previous reports [3,31]. The lattice parameters calculated (*section-2.5.1 of chapter-2*) for TNR (a = b = 3.80 Å and c = 9.56 Å) are consistent with reported values [3] and confirmed by the presence of anatase phase in TNR catalyst. The hydrothermal treatment of TNT at 175 ^{o}C for 48 h under mild acidic conditions (pH = 5.6, iso-electric point of anatase phase) favour the growth of anatase TNR, because at a pH away from the iso-electric point, the strong electrostatic forces between the anatase nuclei retard its aggregation and hence the crystal growth of TNR [31] particles. It was proposed [31] that during hydrothermal treatment, the TNT structure got ruptured, dissolved and rearranged to form anatase nanocrystals that would join in a way known as "oriented attachment" to form TNR morphology. The TNR particles show intense diffraction lines (Fig. 3.2) indicating high crystallinity of TNR despite being synthesized in a autoclave at 175 ^{o}C as compared to amorphous nature of TNT that exhibited broad XRD peaks.

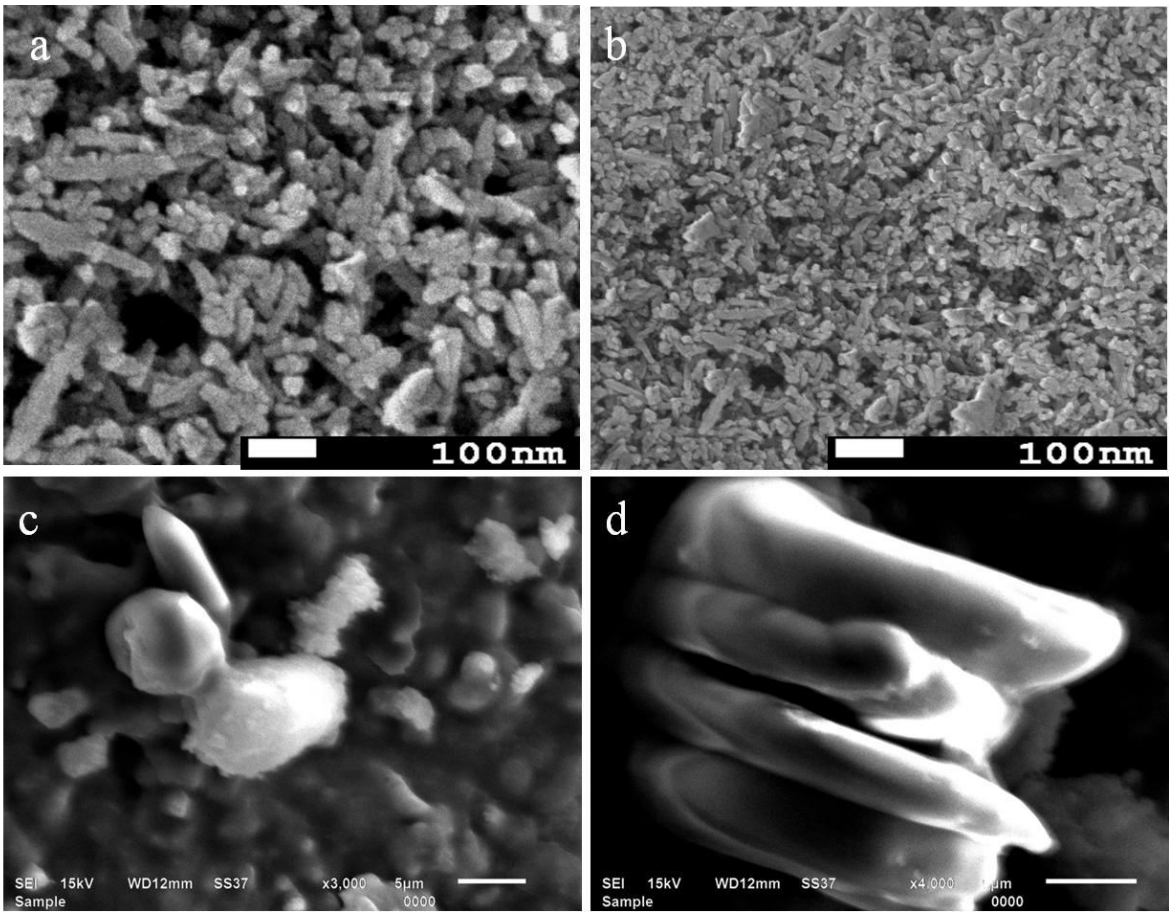

Fig. 3.3 FE-SEM images of (a-b) TNR and (c-d) TNT particles.

The FE-SEM images (Fig. 3.3a-b) with two different resolutions showed uniform distribution of many TNR particles of almost equal size. However, some vertically aligned or broken TNT particles (as noticed in Fig. 3.3c), and few long tubular and bent finger like TNT particles seems to have hollow interior are also observed (Fig. 3.3d). The EDS elemental analysis (Fig. 3.4) established the presence of 39 at.% Ti, 57 at.% O and 3 at.% Na in TNT nanostructures, where Na contamination comes from NaOH treatment of P25 nanoparticles during TNT preparation.

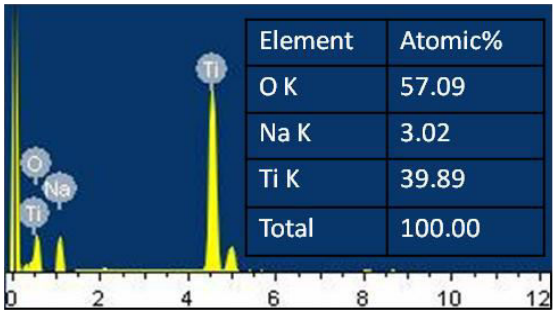

Fig 3.4 EDS elemental analysis of TNT.

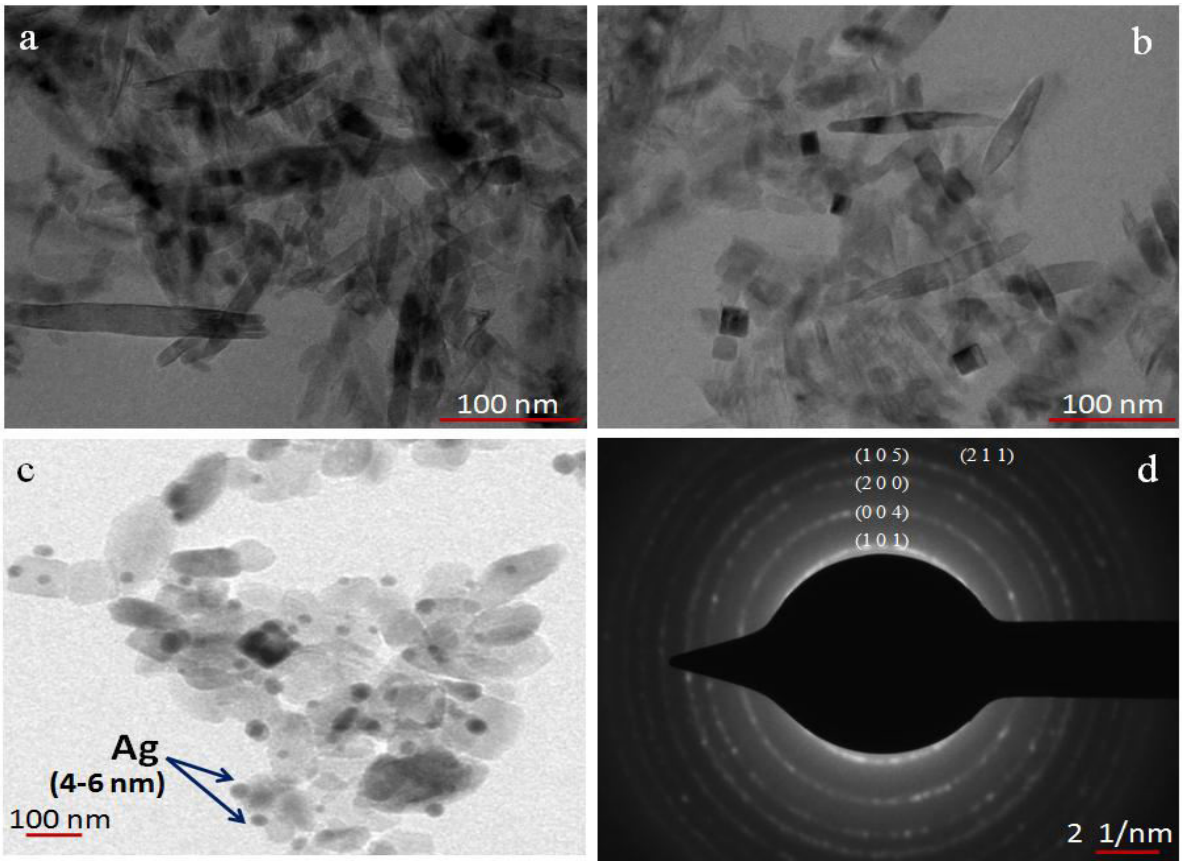

Fig. 3.5 TEM images of TNR (a-b) bare, (c) 1 wt% Ag loaded (d) SAED pattern for bare.

The tem images (Fig. 3.5) reveal the formation of lengthy TNR particles of various dimensions. There are some long and short rice like morphology of TNR particles having diameter 8-13 nm and length 81-134 nm that can be seen in Fig. 3.5 a-b. The average length 104.2 ± 2 nm and

diameter 10 ± 0.1 nm is determined by considering 20 particles. Similar morphology of TNR particles having diameter 6–10 nm but of smaller length 50–70 nm were reported by Christy et al. [34] and Nian et al. [31]. A very fine deposition of Ag nanoparticles (3-5 nm) were present on many TNR particles as can be seen in Fig. 3.5c. The SAED pattern (Fig. 3.5d) displayed the characteristic circular X-ray diffraction rings corresponding to lattice planes ca. (101), (004), (200), (105) and (211) of anatase crystal structure of TNR, and is in accordance with the XRD pattern (Fig. 3.2). The bright and distinct diffraction rings reveals that the TiO_2 nanorods are polycrystalline in nature.

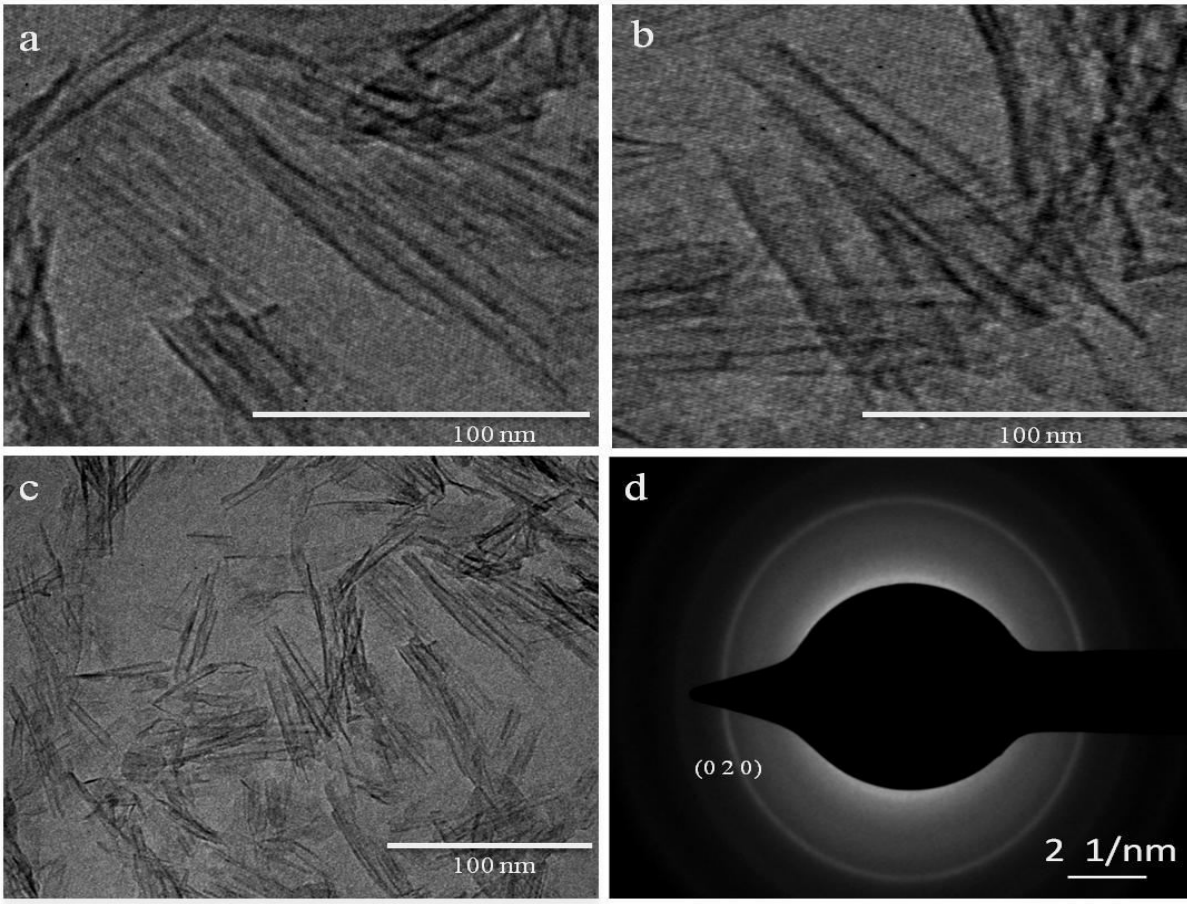

Fig. 3.6 TEM images of (a-c) TNT and (d) its SAED pattern.

The TEM images show the open ended straw like hollow TNT particles (Fig. 3.6) having diameter 9-12 nm and length 82-115 nm. The average diameter of TNT is found to be 10 ± 0.1 nm and length 104.6 ±2 nm, while the wall thickness and internal diameter of TNT are measured to be 1–1.2 nm and 8–13 nm, respectively. Similar types of TNT with a much higher diameter ca.70-100 nm and wall thickness of 14–50 nm were obtained by Hoyer et al. [35], however,

those were unstable at higher temperatures. SAED pattern of TNT (Fig. 3.6d) exhibit a diffuse and fuzzy diffraction ring due to relatively amorphous structure as compared to TNR particles. The lattice plane corresponding to single diffraction ring is indexed to be (020) plane of $Na_2Ti_2O_5$. H_2O nanostructure as observed in XRD pattern in Fig. 3.2.

The S_{BET} (Table 3.1) of as-prepared TNT, TNR in comparison to P25 particles is found to be 176, 79 and 56 m^2g^{-1}, respectively, and is in accordance with difference in their structural morphology and solidity.

Table 3.1. Various physicochemical and electrokinetic parameters of bare and metal deposited titania nanostrutures of different shapes.

Titania catalyst		Surface area (m^2g^{-1})	Conductance (μS)
P25	Bare	56.0	57
	1 wt% Cu	48.1	42
	1 wt% Ag	50.6	39
TNT	Bare	176.0	83
	1 wt% Cu	152.3	46
	1 wt% Ag	162.1	51
TNR	Bare	79.0	56
	1 wt% Ag	69.0	37
	1 wt% Cu	71.2	39

Although, the dimensions of TNT and TNR are same, yet the surface area of the former is around 2.2 times higher than the later, ascribed to its hollow and open ended morphology as observed clearly in TEM images (Fig. 3.6a-c). The decrease in S_{BET} of TNR suggests the collapse of hollow TNT to compact solid and rigid TNR rice like particles during autoclaving at 175 ^oC for 48 h. It has been found that S_{BET} is decreases after photodeposition of 1 wt% Ag and Cu onto TNP of different shapes as can be seen in Table 3.1.

This decrease in S_{BET} can be accounted for the partial surface coverage of TNP surface by Ag and Cu nanodeposits. The Cu deposition onto TNP showed comparatively less reduction in S_{BET} than Ag-TNP, which might be due to the difference in the size of Cu or Ag islands on TNP surface. It is interesting to note that the decrease of S_{BET} due to Ag and Cu deposition over TNT is always higher than Ag/Cu loaded P25 and TNR particles despite having same amount (1 wt%) of metal deposition. This is probably occurs due to blockage of hollow porous surface and open outlet channel to some extent, though we have no such proof to confirm the same. The

adsorption capacity of Ag and Cu may also affect the S_{BET}, since it is reported [36] that adsorption capacity of Cu is more than Ag, thus adsorption of gases (N_2: He:: 70: 30) during BET analysis by 1 wt% Cu-TNP might be more than 1 wt% Ag-TNP, which accounts for higher S_{BET} of the former particles.

The measured surface charge present over different TNP in their aqueous dispersion were found to be +8.82 µequi./g for P25 (pH = 5.8), −1.79 µequi./g for TNT (pH = 6.8) and −6.17 µequi./g for TNR (pH = 6.9) particles. This difference in surface charge of various TNP in the aqueous dispersion could be explained on the basis of difference in surface adsorbed ionic species or surface acidity and basicity [19,22] of TNP, which arises because of hydrothermal treatment of P25 with 0.1 M HNO_3 and 10 M NaOH during preparation [16–19,31] of TNR and TNT particles, respectively. Thus, it is evident that the effective electronic charge on P25 was positive, while it was negative for TNR and TNT particles, and has no influence of the difference in S_{BET} of TNP catalysts. The variation in ζ (-2.8 to -24.8 mV) of different bare and 1 wt% Ag and Cu metal deposited TNP catalysts in their aqueous dispersion are shown in Fig. 3.7. The observed value of ζ -13.5 mV for TNT (pH = 6.85), -22.5 mV for TNR (pH = 6.99) and -2.8 mV for P25 (pH = 5.86) catalysts reveal that their aqueous suspensions (except P25) are quite stable because of electrostatic repulsion between similar charged species. The variation in ζ and surface charge can be explained on the basis of pH and point of zero charge (PZC, around 5.8 for P25 [37]). When TiO_2 is dispersed in water then the surface becomes anionic and thus increase in surface area renders more coverage of hydroxyl groups from H_2O [19], leading to the generation of fewer hydrogen ions in solution and thus increase in pH. If this $pH_{solution} > pH_{PZC}$ then the zeta potential will become negative and vice versa [22]. Since, $pH_{solution}$ of TNT and TNR is more than pH of PZC, hence both have negative ζ values. Furthermore, $pH_{solution}$ of TNR is much more than

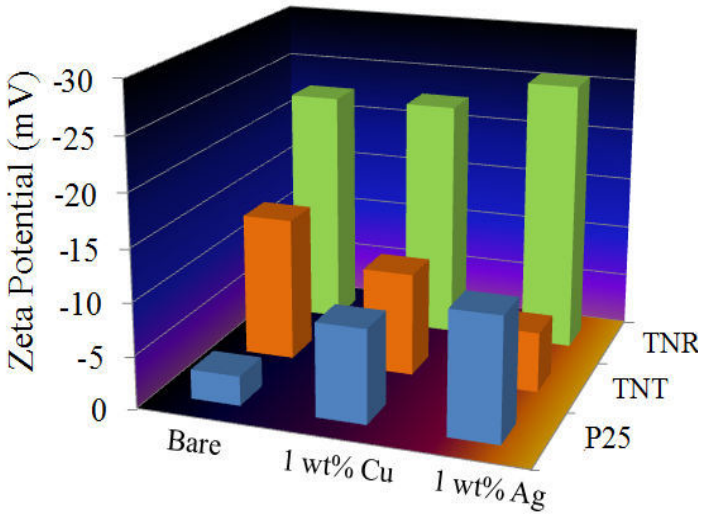

Fig. 3.7 Zeta potential of bare and 1 wt% Ag and Cu photodeposited titania nanoparticles.

$pH_{solution}$ of TNT, hence, its ζ is more negative. However, the ζ (in magnitude) gradually increases (2.8 to 11.7 mV) after 1 wt% deposition of Cu and Ag onto P25 without a notable change in pH (5.92-6.04), while it decreases in case of TNT (pH = 6.53-6.72) from 13.5 to 5.4 mV, after loading the same amount of these metals. Whereas, no notable change in ζ (-22.5 to -24.8 mV) has been noticed for Ag and Cu photodeposited TNR (pH = 6.99–7.09). This variation in ζ, could be justified by the fact that, both the conductance (μS) due to effective electronic charge present over bare P25, TNT and TNR surface in their aqueous dispersion and S_{BET} decreases (Table 3.1) after Cu and Ag loading. As a result, the interactions between Ag and Cu loaded TNP particles and hydroxyl groups may change resulting in changes of $pH_{solution}$ and hence, the ζ value. Other plausible factor might be the formation of some Ag^+ and Cu^+ ions and their hydroxides by atmospheric oxidation of photodeposited metals that may also contribute to the overall electro kinetic properties.

The PCA of various TNP was assessed by the photooxidation of 25 ppm aqueous imidacloprid solution upon exposure of UV irradiation at a different time intervals (Fig. 3.8). Hollow and porous TNT nanostructure possessing largest surface area exhibited highest PCA for the imidacloprid degradation followed by TNR and P25 catalysts. During 40-50 min UV-light irradiation, almost complete photodegradation of 25 ppm IMI by TNT particles occurred as compared to 2 h in case of TNR and P25 catalysts having low photoactivity. The exponentional decrease in concentration of imidacloprid during its photooxidation and simultaneous increase in CO_2 formation with irradiation time indicated degradation kinetics to be first order. The highest photoactivity of TNT could be ascribed to the collective effect of (i) hollow interior and high specific surface area, that favours better adsorption of the

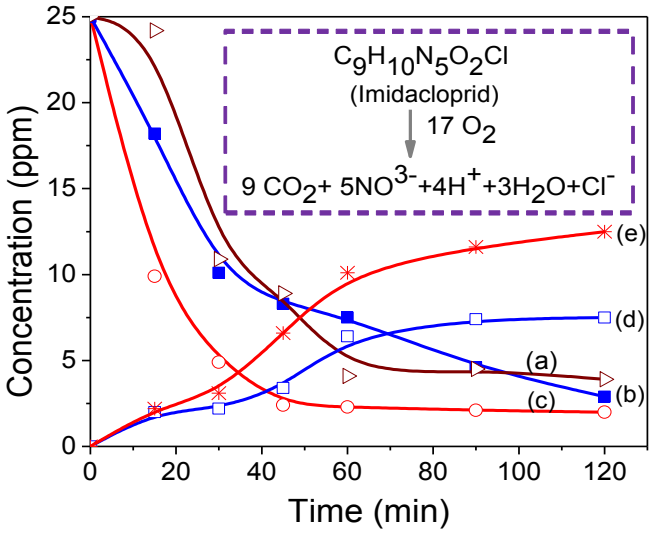

Fig. 3.8 Photodegradation of aqueous suspension of imidacloprid (25 ppm) and (a) P25 (b) TNR, (c) TNT and CO_2 produced by (d) TNR and (e) TNT; inset: expected balanced chemical equation after complete mineralization of imidacloprid

substrate, (ii) the better delocalization of charge carriers along its length, that decreases their recombination, and (iii) the presence of hydrated water in its crystal structure, provoking more number of –OH formation, thus increasing the PCA [3,12,14,15]. Despite having Na content (3 at.%) in its crystal structure which generally reduces [16–18] the photoactivity of TNP, TNT still showed superior degradation of imidacloprid to conventionally best active P25 catalysts [12,14,15]. Being non-ionic in nature, the adsorption of imidacloprid molecules over bare TNP catalyst's surface having different electronic nature of surface charge, does not seem to impart any effect and depends only on the S_{BET}. It has been found that the highest amount (12.5 ppm = 1.42 µmol) of CO_2 produced during 2 h photooxidation of 23 ppm imidacloprid by TNT corresponds to 31.5% of the initial concentration (25 ppm = 0.5 µmol) of imidacloprid utilized and calculations show 4.5 µmol of CO_2 (9 times of initial amount 0.5 µmol, inset Fig. 3.8) expected from its complete photooxidation. Whereas, 18.1% (0.84 µmol) CO_2 formation was found after the photodegradation (2 h) of 21.1 ppm imidacloprid by TNR catalyst. This observed variation in CO_2 formation could be explained on the basis of incomplete decomposition of imidacloprid or the presence of other intermediate photoproducts comprising 53.62% heteroatoms (N, O and Cl) as observed (Fig. 3.9) in HPLC chromatographs. The appearance of unidentified HPLC peaks at retention time = 1.75 and 2.91 min are probably due to the formation [25,27] of intermediates like imidacloprid urea, imidacloprid guanidine, and 6-chloronicotinic acid etc. as detected during photooxidation of imidacloprid by P25 catalyst, although are not confirmed here.

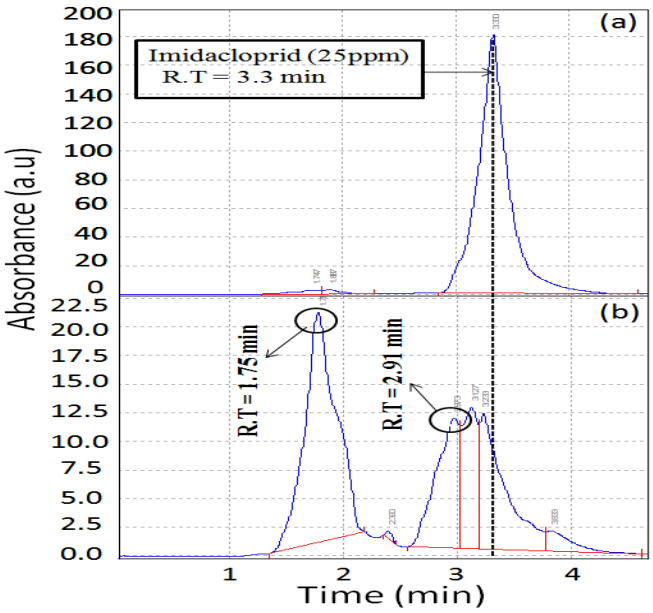

Fig. 3.9 HPLC chromatograph for (a) authentic imidacloprid and (b) its phtooxidation by TNT after 120 min of UV light irradiation.

3.4 Conclusions

In summary, the present research work correlated the crystal phase, surface, structural and electro-kinetic properties of bare, and Ag and Cu deposited TNT (orthorhombic structure) and TNR that were obtained from Degussa P25-TiO_2. By changing the size and shape depending on the preparation conditions, causes the alteration in electronic charge of TiO_2 surface and subsequently, the ζ value is markedly varied in case of different TNP aqueous suspensions. These electro-kinetic parameters could be beneficial for determining dispersion stability of TNP for potential use in metal oxide based nanofluids. The photocatalytic activity of TNT crystals for the photo-oxidation of imidacloprid is found to be superior to the conventional best photoactive P25 owing to its largest surface area and hollow porous surface structure.

3.5 References

[1] J. Wang, X. Liu, R. Li, P. Qiao, L. Xiao and J. Fan, *Catal. Commun.,* 19 (2012) 96–99.

[2] R. Thiruvenkatachari, S. Vigneswaran and S. Moon, *Kor. J. Chem. Eng.,* 25 (2008) 64-72.

[3] N. De la Cruz, R.F. Dantas, J. Gimenez and S. Esplugas, Appl. Catal. B Environ. 130-131 (2013) 249-256.

[4] M.I. litter, *Appl. Catal. B Environ.,* 23 (1999) 89-114.

[5] N. Meng, K.H.L. Michael, Y.C.L. Dennis and K. Sumathy, *Renew. Sust. Energ. Rev.,* 11 (2007) 401-425.

[6] I. Ganesh, A.K. Gupta, P.P. Kumar, P.S.C. Sekhar, K. Radha, G. Padmanabham and G. Sundararajan, *Sci. World J.,* (2013) doi.org/10.1100/2012/127326.

[7] J. Joo, S.G. Kwon, T. Yu, M. Cho, J. Lee, J. Yoon and T. Hyeon, *J. Phys. Chem. B,* 109 (2005) 15297-15302.

[8] W. Yawen, Z. Lizhi, D. Kejian, C. Xinyi and Z. Zhigang, *J. Phys. Chem. C,* 111 (2007) 2709-2714.

[9] J.H.O.S. Pereira, V.J.P. Vilar, M.T. Borges, O. Gonzalez, S. Esplugas and R.A.R. Boaventura, *Sol Energ.* 85 (2011) 2732-2740.

[10] A. Kumar and N. Mathur, *J. Colloid Interface Sci.* 300 (2006) 244-252.

[11] J.L.V. Escoto, Y.D. Chiang, K.C.W. Wu and Y. Yamauchi, *Sci. Technol. Adv. Mater.,* (2013) doi.org/10.1088/1468-6996/13/1/013003.

[12] R.K. Wahi, W.W. Yu, Y. Liu, M.L. Mejia, J.C. Falkner, W. Nolte and V.L. Colvin, *J. Mol. Catal. A Chem.,* 242 (2005) 48-56.

[13] D.P. Macwan, P.N. Dave and S. Chaturvedi, *J. Mater. Sci.,* 46 (2011) 3669-3686.

[14] J.A.T. Antonio, M.A.C. Jacome, S.L.O. Cerros, E.M. Palacios, R.S. Parra, C.A. Chavez, J. Navarete and E.L. Salinas, *Appl. Catal. B Environ.,* 100 (2010) 47-54.

[15] S.J. Kim, Y.S. Lee, B.H. Kim, S.G. Seo, S.H. Park and S.C. Jung, *Int. J. Photoenergy,* (2013) doi.org/10.1155/2012/901907.

[16] M. Qamar, C.R. Yoon, H.J. Oh, N.H. Lee, K. Par, D.H. Kim, K.S. Lee, W.J. Lee and S.J. Kim, *Catal. Today,* 131 (2008) 3–14.

[17] J. Yu, H. Yu, B. Cheng and C. Trapalis, *J. Mol. Catal. A Chem.,* 249 (2006) 135-142.

[18] E. Jr-Morgado, M.A.S. De-Abreu, O.R.C. Pravia, B.A. Marinkovic, P.M. Jardim, F.C. Rizzo and A.S. Araujo, *Solid State Sci.,* 8 (2006) 888-900.

[19] M. Sahu and P. Biswas, *Nanoscale Res. Lett.,* 6 (2011) 441-455.

[20] H.Y. Chuang and D.H. Chen, *Nanotechnology*, 20 (2009) 105704-105714.

[21] J. Ryu and W. Choi, *Environ. Sci. Technol.,* 42 (2008) 294-300.

[22] K. Suttiponparnit, J. Jiang, M. Sahu, S. Suvachittanont, T. Charinpanitkul and P. Biswas, *Nanoscale Res. Lett.,* 6 (2011) 27-35.

[23] N. Mandzy, E. Grulke and T. Druffel, *Powder Technol.,* 160 (2005) 121-126.

[24] C. Hu, Y. Tang, Z. Jiang, Z. Hao, H. Tang and P.K. Wong, *Appl. Catal. A Gen.,* 253 (2003) 389-396.

[25] A. Aguera, E. Almansa, S. Malato, M.I. Maldonado and A.R.F. Alba, *Analusis,* 26 (1998) 245-250.

[26] V. Guzsvany, N. Banic, Z. Papp, F. Gaal and B. Abramovic, React. Kinet. Mech. Catal., 99 (2010) 225-233.

[27] S. Malato, J. Caceres, A. Aguera, M. Mezcua, D. Hernando, J. Vial and A.R.F. Alba, Environ. Sci. Technol., 35 (2001) 4359–4366.

[28] H. Guan, D. Chi, J. Yu and X. Li, *Pest. Biochem. Physiol.,* 92 (2008) 83-91.

[29] R. Zabar, T. Komel, J. Fabjan, M.B. Kralj and P. Trebse, *Chemosphere,* 89 (2012) 293-301.

[30] J. Marugan, M.J.L. Munoz, W. Gernajak and S. Malato, *Ind. Eng. Chem. Res.,* 45 (2005) 8900-8908.

[31] J.N. Nian and H. Teng, *J. Phys. Chem. B,* 110 (2006) 4193-4198.

[32] J.Z. Jin, X. Wang, W. Li, J. Zhang, S. Zhang, X. Guo and Z. Zhang, Dalton Trans., (2003) 3898-3901.

[33] X. Wang, H. He, Y. Chen, J. Zhao and X. Zhang, *Appl.Surf. Sci.,* 258 (2012) 5863-5868.

[34] P.D. Christy, N. Melikechi, N.S.N. Jothi, A.R.B. Suganthi and P. Sagayaraj, *J. Nanopart. Res.,* 12 (2010) 2875-2882.

[35] P. Hoyer, *Langmuir,* 12 (1996) 1411-1413.

[36] T. Nanba, S. Masukawa, J. Uchisawa and A. Obuchi, *Catal. Lett.,* 93 (2004) 195-201.

[37] C. Karunakaran, P. Anilkumar and P. Gomathisankar, *Chem. Cent. J.,* 5 (2011) 31-40.

4. Photocatalytic Activity of Sodium Titanates for m-Dinitrobenzene Reduction and Sulfosulfuron Oxidation

4.1 Introduction

Nanostructures of different geometric shapes of TiO_2 have been recently studied due to their superior optical and photocatalytic properties attributed to their dimensional anisotropy, where the photoexcited e^-/h^+ pair is a key factor in controlling these properties [1-11]. As discussed in *section-1.2.2* of chapter-1 that increased delocalization of charge carriers in elongated nanostructures led to a remarkable decrease in e^-/h^+ recombination probability, hence larger numbers of e^- and h^+ exist on the active sites of the lengthy nanocrystal's surface, resulting in higher photoactivity as compared with spherical nanoparticles. Especially, TiO_2 nanorods and nanotubes are proven to be effective photocatalysts because of the presence of a large number of surface exposed atoms, high specific surface area and higher relaxation lifetime [3,4]. As photocatalysis is an area of intense research activity for finding suitable materials, hence, Ti-O based other materials such as TNT [12-17] and TNT(S) [5,13-15] nanoribbons [17] etc. are found to be of special interest because of their crystalline and scroll structure and therefore, considerably utilized for a wide range of applications, including photocatalysis [13–17].

Several groups found [5,13,15,18-21] that the TNT and TNT(S) may possess better or poorer photocatalytic activity in comparison to P25 catalyst. For instance, Stengl et al. [13] and Song et al. [5] demonstrated the good photooxidation ability of TNT(S) for 4-chlorophenol and chloroform degradation, respectively relative to P25 catalyst. In contrast to this, reports by Yu et al. [15] and Lee et al. [20] conveyed the TNT(S) to be as an inferior photocatalyst to that of P25. Thus, there is a quite inconsistency in the literature reports about its photocatalytic activity. Similarly for TNT, Zhu et al. [21] found that the as-prepared TNT without calcination exhibited decent photocatalytic activity for the oxidation of sulforhodamine, but Yu et al. [15] claimed negligible photoactivity of TNT when sintered below 300 ^oC. One of the important factors responsible for fluctuating photocatalytic activity of the TNT and TNT(S) may be the sodium content [20] which plays a crucial role in crystal phase and morphology as a function of calcination temperatures. Generally, sodium titanates are investigated for their physicochemical properties [22,23] and a little data is available in literature dealing with the photocatalytic activity [13-15] of TNT and TNT(S) that may be a promising photocatalyst in the environmental

applications. Although, the photoxidation ability of TNR and TNT have been revealed in a few reports but no information is available on photoreductive ability and the effect of noble metal loading for the same as a function of relaxation time of photoexcited charge carriers.

The production of amino-derivatives from the corresponding nitro-aromatics has attracted a great deal of interest [24,25] due to their potential use as intermediates for the synthesis of a variety of fine chemicals. Recent reports [24,25] indicate the potential of chemoselective $-NO_2$ group reduction through TiO_2 photocatalysis. Thus, *m*-DNB has been chosen as a model compound to explore the photoreduction activity resulting in two different reduction products, namely *m*-DAB and *m*-NA. Therefore, this chapter is devoted to the preparation of TNT(S) from TNT to study the effect of Au deposition on the photocatalytic reduction of *m*-DNB relative to P25 catalyst under UV-light irradiation, with identification of its photoreduction products. Apart from this, photodegradation of sulfosulfuron herbicide with corresponding evolution of CO_2 is also comparatively tested by TNT, TNT(S) and P25 catalysts because of its enormous use in wheat crop to control troublesome grass weeds P. *minor* [26] whose persistence in soil and water could damage the crops.

4.2 Experimental section

4.2.1 Synthesis and characterization of bare Au-loaded TNT and TNT(S): TNT and TNT(S) were prepared as described in *section-2.2.1* and *section-2.2.3* of chapter 2, respectively. The photodeposition of Au onto P25, TNT and TNT(S) was carried out by the photodeposition method reported in *section-2.4.1* of chapter-2. These as-prepared samples were characterized by XRD (section-2.5.1), SEM coupled to EDS (section-2.5.2), TEM (section-2.5.3), Time resolve decay (section-2.5.7) and S_{BET} (section-2.5.10) techniques which are discussed in chapter-2.

4.2.2 Photocatalytic activity: It was done by analyzing reaction samples obtained after photooxidation of sulfosulfuron (*section-2.6.1*) with HPLC (*section-2.6.4*), GC (*section*-2.6.5) and GC-MS (*section-2.6.6*) techniques as described in chapter-2.

4.3 Results and discussion

The XRD patterns of titania precursor P25, the effect of thermal treatment on as-prepared TNT at different temperatures for the gradual change in crystal phase and TNR formation at 800 ^{o}C are shown in Fig. 4.1. TNT, prepared by hydrothermal alkali treatment, is composed of

orthorhombic crystal structure (Fig. 4.1b) as shown in chapter-3 (*section 3.3*). Upon calcination of TNT at 500 °C for 2 h, peaks at 2θ = 37.7914°, 48.0844° and 55.0144° corresponding to anatase phase appear (Fig. 4.1c). However, upon thermal treatment at 800 °C, the complete conversion of hollow TNT to highly crystalline TNT(S) formation (Fig. 4.1d) occurs. The characteristic peak at 2θ = 24.4945° for monoclinic unit cell of $Na_2Ti_6O_{13}$ with lattice parameters, *a* = 15.3 Å, *b* = 9.03 Å, and *c* = 3.54 Å are in good agreement with the literature report [28] *a* = 15.2 Å, *b* = 9.02 Å, and *c* = 3.52 Å. There are many other crystallographic planes viz., (100), (110), (311), (402) and (020) corresponding to 2θ values of 24.4935°, 26.7589°, 30.0901°, 33.39811° and 48.5410° have also been observed for TNR particles.

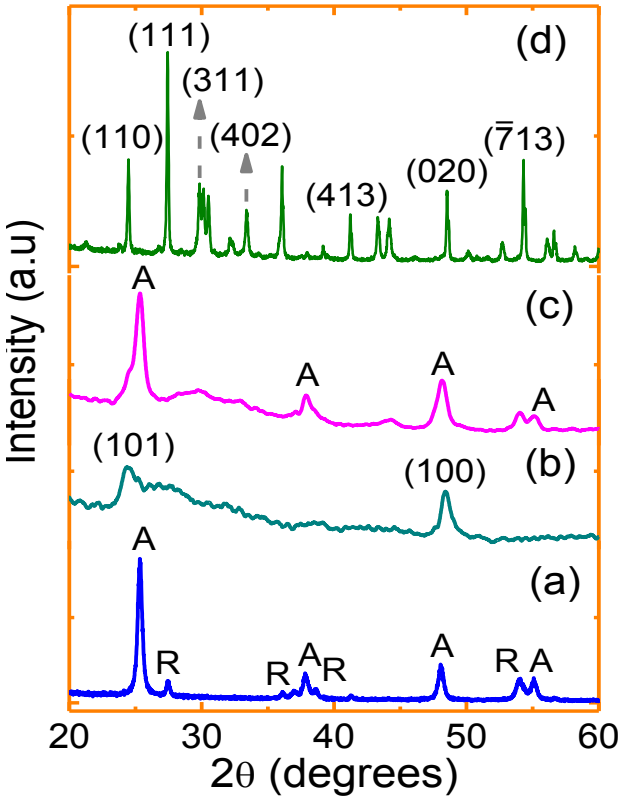

Fig. 4.1 XRD patterns of (a) P25, (b) TNT, (b) TNT calcined at 500 °C and TNT(S).

This structural transformation was explained [14,15] by the condensation of corrugated layers of trititanate having three edge-sharing TiO_6 octahedral units into a $Na_2Ti_6O_{13}$ structure by the connecting corners of opposing octahedra to link the layers together. The distortion in the crystal structure of TNT and TNR is further evidenced by magnetic susceptibility (MSP) measurement, though it has no correlation with the photocatalytic activity. The MSP for TNT(S) (-48.5 m^3/kg) is found to be around 2-times to that of TNT (-28.2 m^3/kg) in comparison to zero of P25, and is attributed [23] to the change in coordination number of lattice O-atoms in their respective crystal structures.

The FE-SEM images of TNT(S) (Fig. 4.2a-b) show the formation of many lengthy nanorods particles of various dimensions aggregated haphazardly. The EDS elemental analysis (Fig. 4.2c-d) confirmed the presence of 39.8 at.% Ti, 57.0 at.% O and 3.0 at.% Na in TNT and 38.4 at% Ti, 58.9 at% O and 2.6 at% Na in TNT(S) nanostructures. The presence of Na

contamination came from NaOH treatment of P25 particles during preparation of nanotubes and nanorods.

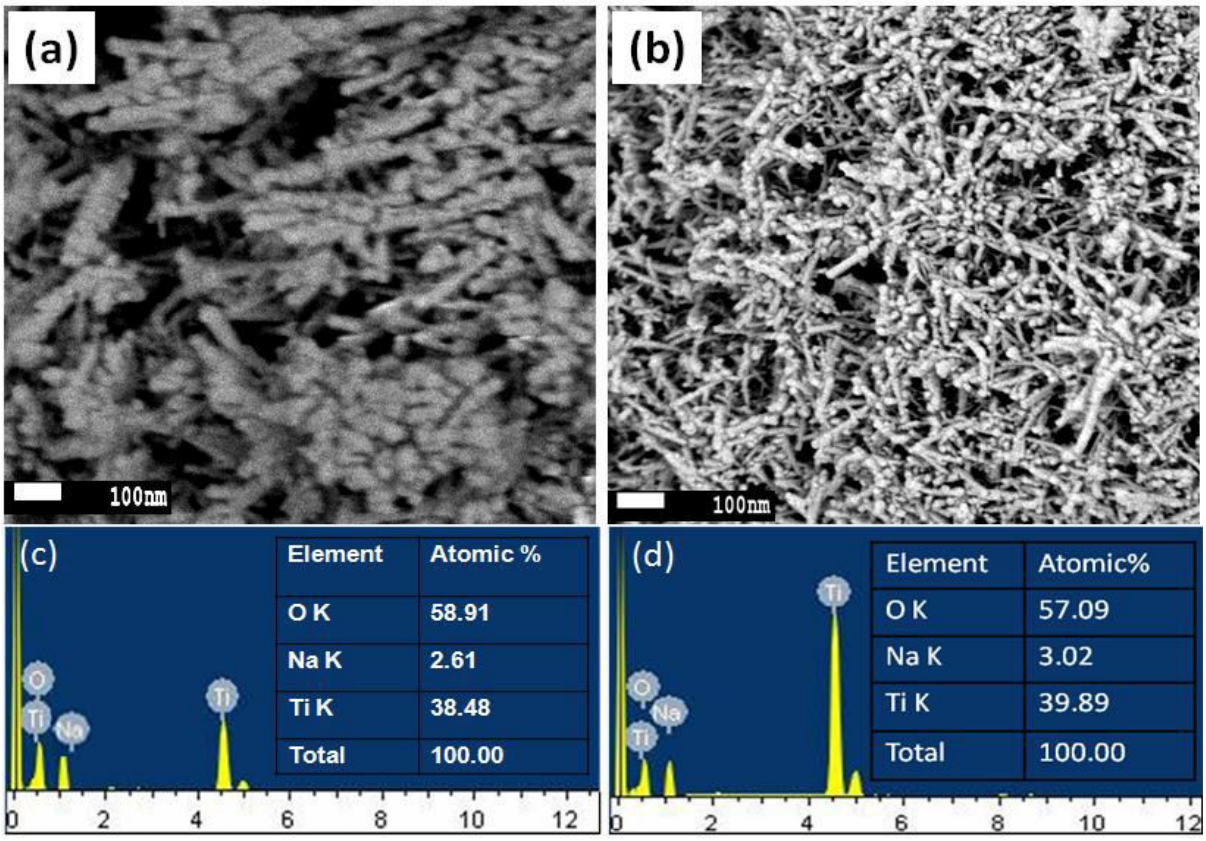

Fig. 4.2 (a and b) SEM images of TNT, EDS elemental analysis of (c) TNT(S) and (d) TNT.

The TEM images for TNT (Fig. 4.3 a-b) show its open ended morphology (already discussed in *section 3.3 of* chapter-3). Whereas, TEM images for TNT(S) (Fig. 4.3c-e), clearly show the formation of long stick like lengthy cylindrical particles of diameter = 25-35 nm and length = 200-500 nm having smooth surface structure. However, very fine Au deposits of narrow size distribution (3-6 nm) on the surface of TNT(S) (Fig. 4.3 e-f) is clearly found for its Au loaded analogy.

The DLS studies (Fig. 4.4 a-b) revealed the particle size of TNT and TNT(S) to be 114-203 nm and 310-745 nm, respectively, which is somewhat higher than ca. from their respective TEM images, attributed to the measurement of hydrodynamic diameter [29]. The S_{BET} of as-prepared TNT(S) (21 m^2g^{-1}) has been found to be less than that found for TNT (176 m^2g^{-1}), and P25 (55 m^2g^{-1}). The large decrease in S_{BET} value for TNT(S) is due to collapse of hollow interior

and dehydration of inter-layered hydroxyl groups of TNT interior surface [15] possessing much larger surface area.

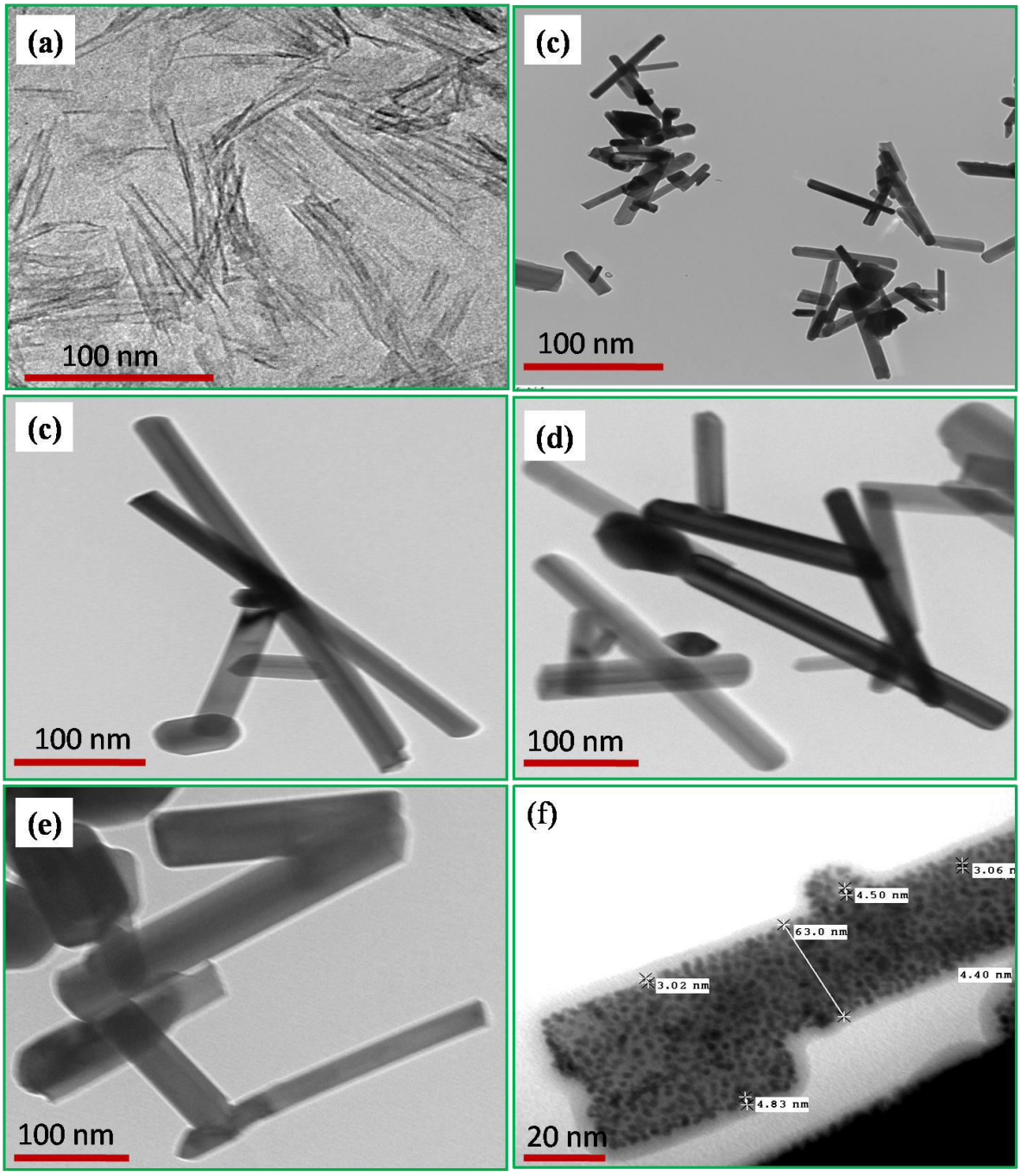

Fig. 4.3 TEM images of (a) TNT, (c-e) TNT(S) and Au-photodeposited TNT(S).

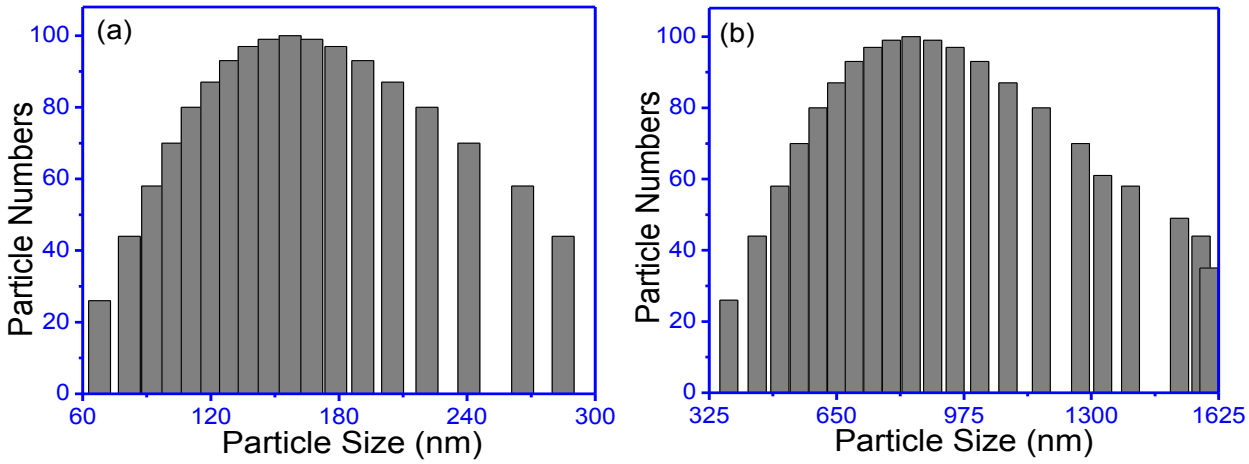

Fig. 4.4 Size distribution plots for (a) TNT and (b) TNT(S) using DLS studies.

The photodeposition of 0.5 wt% Au onto these nanostructures also cause decrease in S_{BET} from 55 to 53.6 m^2g^{-1}, 176 to 172.1 m^2g^{-1} and 21 to 19.8 m^2g^{-1} for P25, TNT and TNT(S) particles, respectively, because of the partial surface coverage with Au deposits. Similar results for the decrease in S_{BET} after deposition of Ag and Cu over titania nanostructures were recently reported by our group [18] (described in chapter-3, *section 3.3*). The solid state absorption spectra of 0.5 wt% Au deposited titania nanostructures show almost no change in the absorption onset, however, a broad peak (500-600 nm) ascribed to the surface Plasmon band [31] of deposited Au nanoparticles is noticed (Fig. 4.5a).

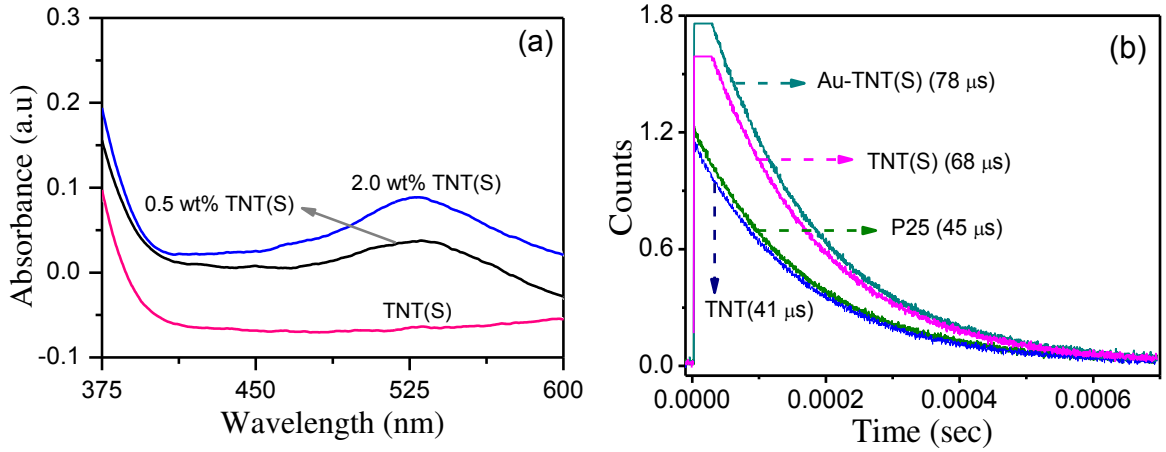

Fig. 4.5 (a) Solid state diffuse absorption spectra Au loaded TNT(S) and (b) time resolve luminescence decay of bare P25, TNT and, bare and 0.5 wt% Au-loaded TNT(S).

It is reported [32] that lengthy nanocrystals display superior photocatalytic activity in comparison to spherical nanoparticles because of better delocalization and reduced recombination rate of photoexcited e^-/h^+ pairs. Hence, before assessing their photoactivity time resolve photoluminescence decay was relatively measured using the pulse excitation method (Fig. 5.5b). The average relaxation time of charge carriers of photoirradiated TNT(S) (68 µs) is found to be around 1.5 times more than that of P25 (45 µs), which is further improved to 78 µs after 0.5 wt% of Au deposition onto TNT(S) particles. As loaded Au co-catalyst acts as a sink for the photogenerated electrons [31,33] the life time of charged specie is notably enhanced. Similar results for increase in recombination time from 10 to 100 µs after 1 wt% Pt loading over TiO_2 were previously reported [34].

It is demonstrated (Fig. 4.6) that *m*-DNB is quantitatively and selectively reduced to *m*-DAB by P25 and TNT(S) particles. TNT particles being hollow in nature and having largest surface area, displayed quite negligible activity for the *m*-DNB reduction. The selective formation (~99%) of *m*-DAB under such mild reaction conditions represent an important advancement in the selective hydrogenation of *m*-DNB. Such selectivity for formation of *m*-DAB formation has been reported but under very high pressure (2.6 Mpa) using 20% w/w Ni/SiO_2 [35]. Although S_{BET} of TNT(S) is several times less than P25, which means less surface -OH groups, but still TNT(S) particles exhibited similar PCA. This fact is verified by the work of Wang et al. [36] who showed that small nanoparticles (6 nm) with high surface area (253 m^2g^{-1}) was not essential for its high PCA, while a particle with higher grain size (11 nm) and less surface area (153 m^2g^{-1}) could exhibit photocatalytic properties. This indicates that the parameters such as crystal structure, presence of sodium, and surface defects etc., might be responsible for have caused better photoactivity of TNT(S) particles. Although, sodium content [15] responsible for decreasing the TiO_2 photoactivity does not hold good for TNT(S) particles, which showed comparable PCA to that of P25 despite having the appreciable amount of sodium

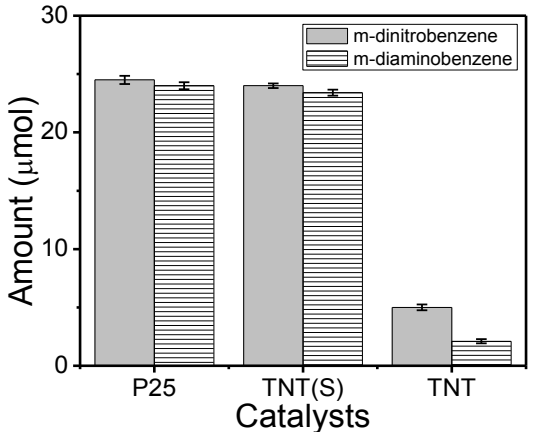

Fig. 4.6 Amount of m-dinitobenzene reduced and m-diaminobenzene produced by bare P25, TNT and TNT(S) after 8 h of UV-light irradiation.

(2.61 at%) in its crystal morphology. The retardation in e^-/h^+ recombination as evidenced by the higher relaxation time, 68 µs as compared to 45 µs for P25 for lengthy crystalline TNT(S) nanocrystals of cylindrical symmetry, probably seems to be responsible for its improved photocatalytic activity.

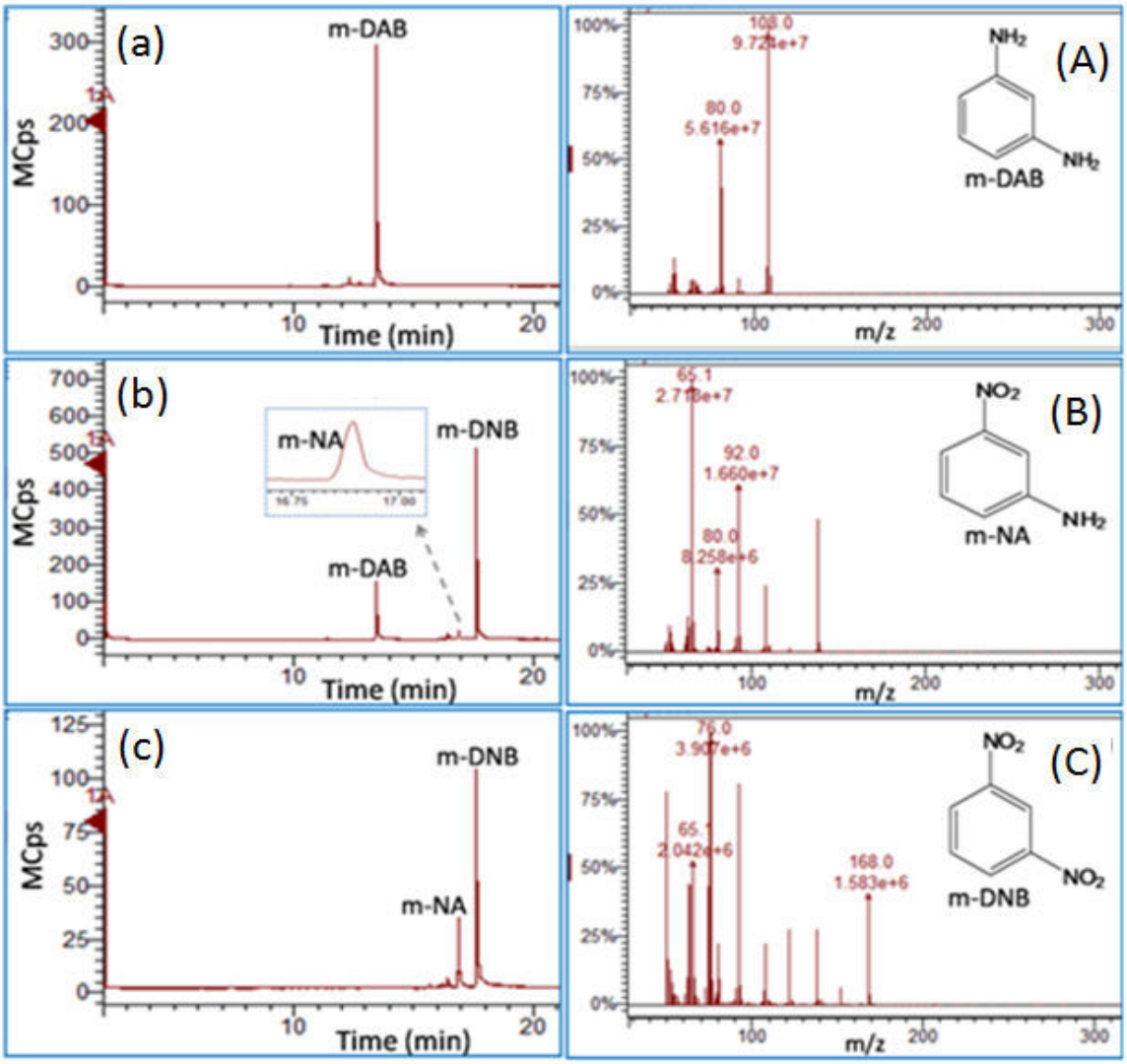

Fig. 4.7 GC -chromatographs after 8 h of photoreduction of m-DNB with (a) bare and Au-loaded (b) 0.5 wt% and (c) 2.0 wt% TNT(S), inset enlarged view, and (A-C) corresponding MS-spectra with respective structural formulas (*inset*).

This selective conversion of *m*-DNB to *m*-DAB using bare TNT(S) is evidenced by the GC-MS chromatographs (Fig. 4.7a), where no peak corresponding to *m*-NA was noticed. However, after 0.5 wt% Au deposition onto P25 and TNT(S) nanoparticles, formation of *m*-NA

along with *m*-DAB was observed (Fig. 4.8a), and the formation of these compounds (by 0.5 wt% Au loaded TNT(S)) was also evidenced by GC-MS analysis (Fig. 4.7b). Moreover, Au loading does not influence the TNT photoactivity except for the enhanced selectivity of *m*-NA production.

This low photoactivity of TNT as compared with TNT(S) can be ascribed to the poor electron mobility through the channel like geometry, lack of crystallinity and deficiency in compactness hindering the conduction and delocalization of photoexcited electrons. The deposited Au nanoparticles have the tendency to capture the photogenerated electrons from titania nanoparticles because of its suitable Fermi level position (0.4 eV vs. NHE) that is more positive than CB position of titania (−0.1 eV vs. NHE) and is thermodynamically favorable, thus favoring the charge separation and hence increases the photoactivity [24–26]. Adsorption of *m*-DNB on Au-TNP can generate a resonance form with a single delocalized positive charge on the ring where only one of the -NO_2 group (scheme-4.1a) might be activated [24].

The deactivation of -NO_2 group is favored by the fact that, Au after capturing the photoproduced electrons from the support acquires partial negative charge, and its interaction with *m*-DNB seems to be permissible with the N-atom of *m*-DNB having positive charge as shown in Scheme 4.1(a). As a result, the resonance of the interacting group is not favorable, and hence it is not activated for the nucleophilic attack. The reduction of other -NO_2 (activated group) to -NH_2 group occurs through the utilization of six electrons (Scheme 4.1a) reported by Flores et al. [37] while photoproduced holes were utilized in

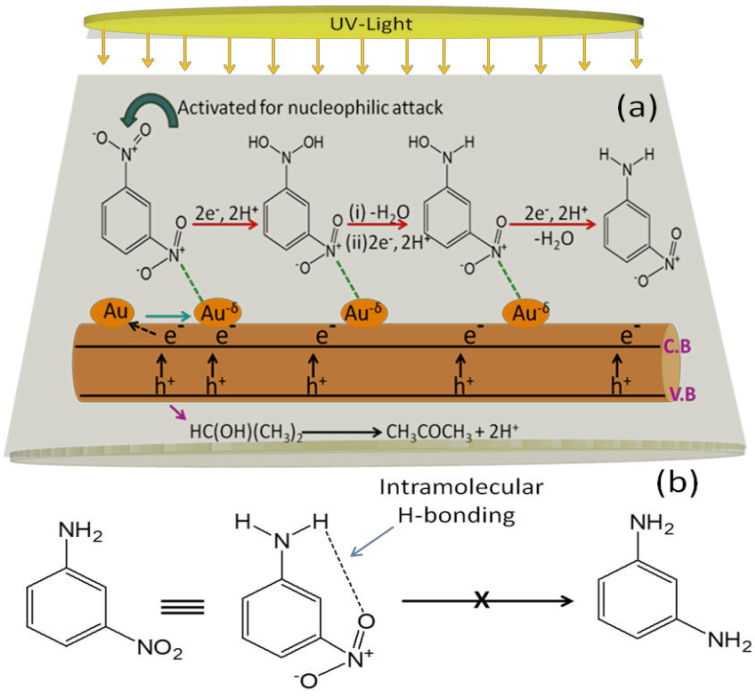

Scheme-4.1 (a) Mechanism for reduction of *m*-DNB to *m*-NA using Au loaded TNT(S) and (b) inhibition of *m*-NA to m-DAB.

oxidation of isopropyl alcohol to acetone (not measured) and the H^+ ions are utilized in the reduction of -NO_2 group.

After the reduction of one -NO_2 to -NH_2 group the other –NO_2 group was expected to be reduced leading to *m*-DNB. Interestingly, with increased reaction time up to 16 h, no such expected observation was observed in the present study (inset Fig. 4.8a). Thus, the high yield and selectivity for *m*-NA formation could probably be due to stabilization of *m*-NA through intra-molecular H-bonding (Scheme 4.1b) that inhibits the reduction of second -NO_2 group.

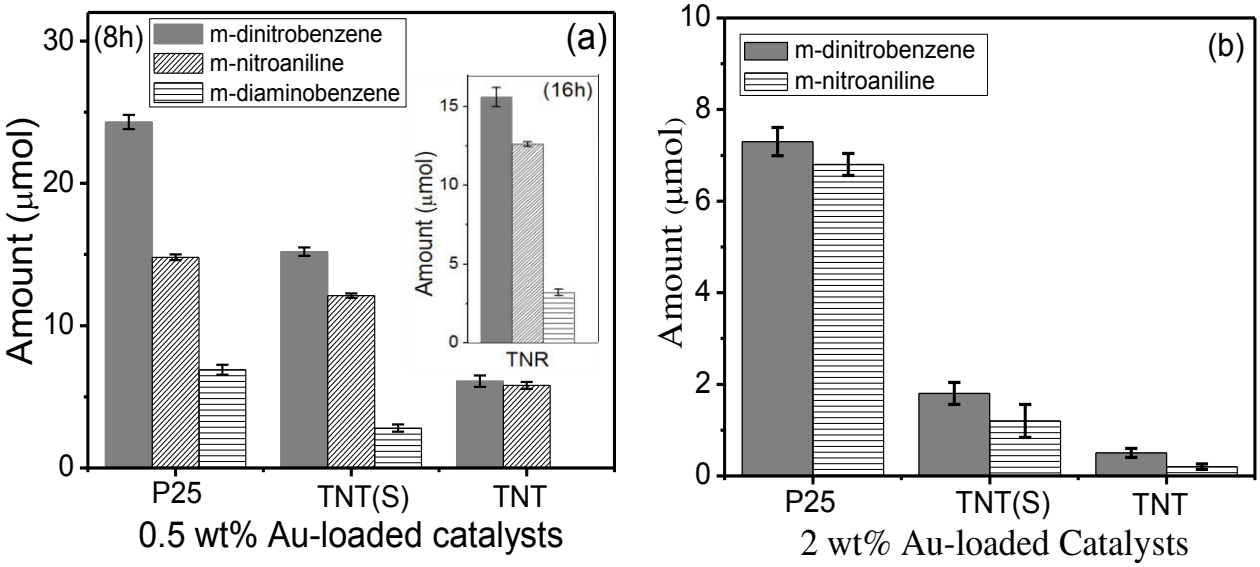

Fig. 4.8 Amount of m-dinitobenzene reduced, m-nitroaniline and m-diaminobenzene produced by Au-loaded catalysts after UV-light irradiation of (a) 8 h; inset 16 h, and (b) 8 h.

Since, the percentage of Au loading is less (0.5 wt%), the complete coverage of the catalyst's surface is not possible, hence, some molecules of *m*-DNB are in direct contact with bare TNT(S) surface leading to the formation of *m*-DAB. However, when the amount of Au loading was increased from 0.5 to 2 wt% decrease in PCA was found, but at the same time selectivity for m-NA formation increases (Fig. 4.8b). This low PCA may be due to more surface coverage by the Au nanodeposits rendering the light reaching to the titania/titanate nanoparticles, hence decreases the e^-/h^+ formation and consequently diminishes the photoreduction of *m*-DNB.

The comparative photooxidation of sulfosulfuron (1000 ppm) by bare TNT to that of TNT(S) and P25, during 5 h of UV-light irradiation is shown in Fig. 4.9. It has been found that the photooxidation efficiency of TNT was around *ca.* 4.8 ± 0.3 and 1.9 ±0.3 times higher than the TNT(S) and P25 after 5 h of light irradiation, respectively and found to be the opposite trend

(TNT(S) = P25 > TNT) to that found in the photoreduction of *m*-DNB (Fig. 4.6). Such high photocatalytic activity of TNT could be accredited to its high surface area (176 m^2 g^{-1}) and hollow interior (Fig. 4.3a-b) providing better adsorption of reacting substrate. However, this observed order of photocatalytic activity (TNT > P25 > TNT(S)) was contrary to that of observed recombination time of photoproduced e^-/h^+ pair (Fig. 4.5b). This could be ascribed to a very thin wall of thickness *ca.* 0.8-1.1 nm for TNT favouring rapid diffusion of e^-/h^+ pairs to its surface, making more number of h^+ available for oxidation of the reacting molecules. On the other hand, the deleterious effect of Na in TNT (3.0 at%) towards the PCA seems to be offset collectively by the S_{BET}, thin wall thickness and hollow interior of TNT. Furthermore, TNT is reported to have layered structure [4,5] so there is a probability of adsorption of water molecules in between these layers through weak vander waals forces of attraction. As a result, more number of oxidative species (•OH) will be produced from the adsorbed water molecules by charge exchange between the conduction and valence band in case of TNT than P25 and TNT(S), having no layered structures. Since, these species are virtually reported to be responsible for oxidation, therefore, TNT has the highest photooxidation activity. However, as the S_{BET} of P25 (56 m^2g^{-1}) is larger than TNT(S) (21 m^2g^{-1}), the water adsorption ability and corresponding formation of oxidative specie during UV-light illumination would be more for the former and hence, its PCA, and is in accordance with photooxidation of IMI as discussed in chapter-3 and -4.

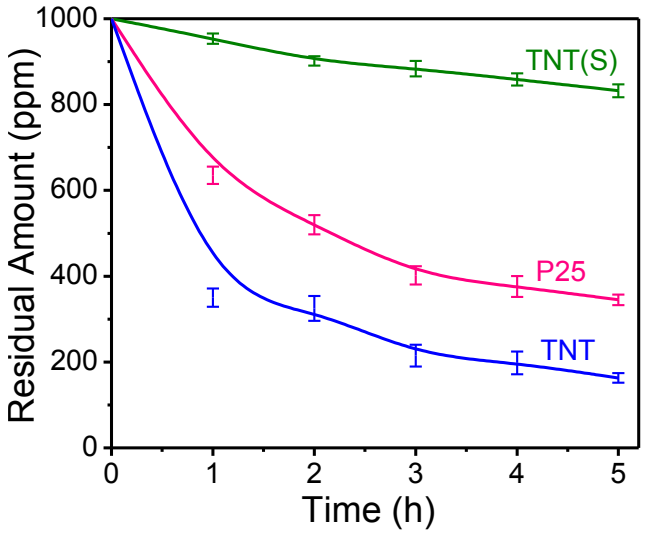

Fig. 4.9 Comparative photocatalytic degradation of sulfosulfuron by P25, TNT, TNT(S).

Although, the amount of remnant sulfosulfuron is found to be very less (158 ± 12 ppm) in comparison to its initial amount (1000 ppm) after 5 h of photooxidation with TNT, yet the complete mineralization of reacting substrate has not been observed, evidenced by the presence of various peaks in HPLC chromatograph (Fig. 4.10). Thus, in-order to determine the actual percentage of herbicide dissipated, CO_2 evolution during its UV-light irradiation in the presence

of bare catalysts was measured (Fig. 4.11), and is found to correlate with the photooxidation activity of catalysts (Fig. 4.10). The highest amount (395 ± 5.6 ppm = 44.8 ± 0.6 µmol) of CO_2 produced during 5 h photooxidation of 842 ± 12 ppm sulfosulfuron by TNT corresponds to 27.8 ± 0.4% of the initial concentration (1000 ppm = 10 µmol) of sulfosulfuron utilized, while 9.6 ± 0.3% (136 ± 4.2 ppm = 15.4 ± 0.5 µmol) of CO_2 found to be produced from 718 ± 11.3 ppm (7.1 ± 0.1 µmol) of sulfosulfuron by P25. The calculation showed that 160 µmol of CO_2 (16 times of initial amount 10 µmol, inset Fig. 4.12) is expected from its complete photooxidation. Whereas, only 6.9 ± 0.2% (10.58± 0.5 µmol) of CO_2 evolution is found after 5 h of photodegradation for 185 ± 9.3 ppm sulfosulfuron by the TNT(S) catalyst. Thus it is evident here that, TNT(S) also exhibited comparable photooxidation activity in relation with P25 in-terms of CO_2 production. This observed variation in CO_2 formation could be explained on the basis of incomplete decomposition of sulfosulfuron or the presence of other intermediate photoproducts comprising 55.31% heteroatoms (N, O and S) that have not been determined in the present study.

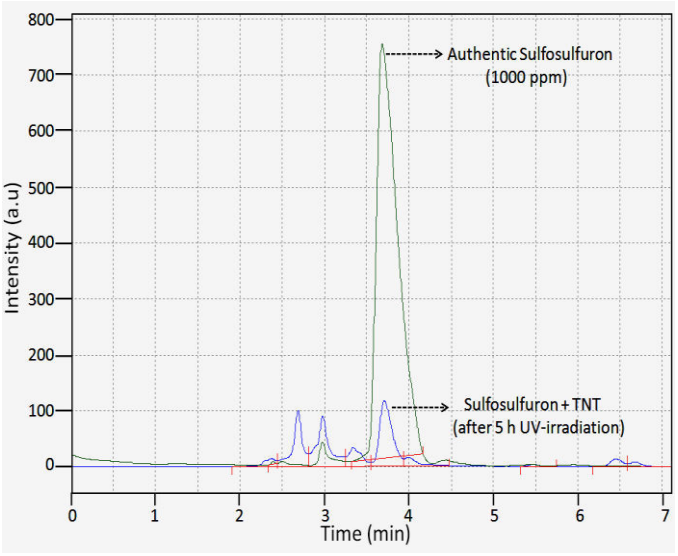

Fig. 4.10 Comparative HPLC chromatograph for authentic sulfosulfuron and after its photooxidation with bare TNT.

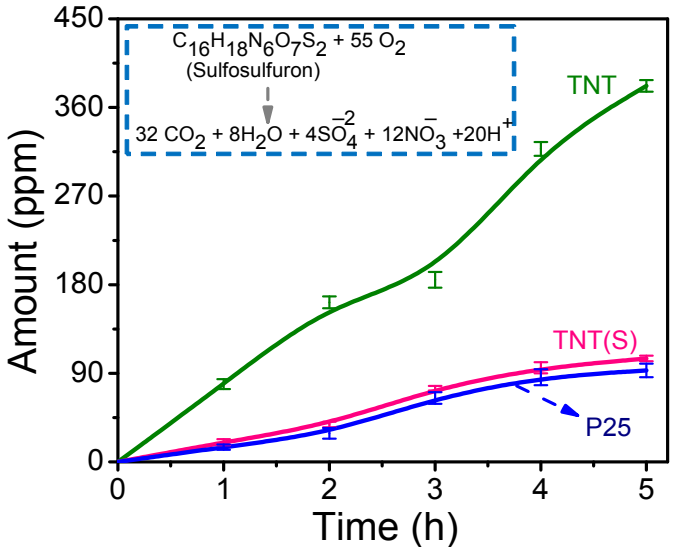

Fig. 4.11 CO_2 formation during photooxidation of sulfosulfuron by various catalysts; inset balanced chemical equation expected after complete mineralization.

4.4 Conclusions

Present chapter demonstrated the synthesis of highly crystalline TNT(S), showing comparable photoredox activity to most active P25. Au-loading onto these as-prepared nanoparticles was found to alter selectivity and product distribution for the reduction of m-DNB to *m*-NA and *m*-DAB. TNT similar to that found in chapter-3 and -4, showed higher PCA for decomposition of sulfosulfuron to CO_2.

4.5 References

[1] Y. Lan, X. Gao, H. Zhu, Z. Zheng, T. Yan, F. Wu, S. P. Ringer and D. Song, *Adv. Funct. Mater.,* 15 (2005) 1310-1318.

[2] J. Joo, S.G. Kwon, T. Yu, M. Cho, J. Lee, J. Yoon and T. Hyeon, *J. Phys. Chem. B,* 109 (2005) 15297-15302.

[3] S. H. Kang, S. H. Choi, M. S. Kang, J. Y. Kim, H. S. Kim, T. Hyeon and Y. E. Sung, *Adv. Mater.* 20 (2008) 54-58.

[4] B. Fei, Z. Deng, J. H. Xin, Y. Zhang and G. Pang, *Nanotechnology,* 17 (2006) 1927-1931.

[5] H. Song, H. Jiang, T. Liu, X. Liu and G. Meng, *Mater. Res. Bull.* 42 (2007) 334-344.

[6] C.C. Chen, D. Fang and Z. Luo, *Rev. Nanosci. Nanotechnol.,* 1 (2012) 229-256.

[7] M. Eagambaram and R. Rajmohan, *J. Biomed. Nanotechnol.* 7 (2011) 225-228.

[8] B. Vidhya and A. Ford, *Nanosci. Nanotechnol. Lett.,* 5 (2013) 980-985.

[9] G. Ping, S. Deng, D. Wang, D. Chen, L. Qin, K. Shu, C. Li, *Nanosci. Nanotechnol. Lett.,* 5 (2013) 785-790.

[10] G.F. Xu, Y. Gao, A. Shiue, C.M. Ma and C.T. Chang, *Nanosci. Nanotechnol. Lett.,* 3 (2011) 778-783.

[11] C.Y. Kuo, S.Y. Lien, Z.S. Wu, F.S. Shieu and C.F. Chen, *Nanosci. Nanotechnol. Lett.,* 3 (2011) 195-199.

[12] T. Kasuga, M. Hiramatsu, A. Hoson, T. Sekino and K. Niihara, *Langmuir,* 14 (1998) 3160-3163.

[13] V. Stengl, S. Bakardjieva, J. Subrt, E. Vecernıkova, L. Szatmary, M. Klementova and V. Balek, *Appl. Catal. B Environ.* 63 (2006) 20-30.

[14] M. Qamar, C.R. Yoon, H.J. Oh, N.H. Lee, K. Par, D.H. Kim, K.S. Lee, W.J. Lee and S.J. Kim, *Catal. Today,* 131 (2008) 3-14.

[15] J. Yu, H. Yu, B. Cheng and C. Trapalis, *J. Mol. Catal. A Chem.,* 249 (2006) 135-142.

[16] J.N. Nian and H. Teng, *J. Phys. Chem. B,* 110 (2006) 4193-4198.

[17] K. Kiatkittipong, C. Ye, J. Scott and R. Amal, *Cryst. Growth Desig.,* 10 (2010) 3618-3625.

[18] I. S. Grover, S. Singh and B. Pal, *Appl. Surf. Sci.,* 280 (2013) 366-372.

[19] G. Potari, D. Madarasz, L. Nagy, B. Laszlo, A. Sapi, A. Oszko, A. Kukovecz, A. Erdohelyi, Z. Konya and J. Kiss, *Langmuir,* 29 (2013) 3061-3072.

[20] C.K. Lee, C.C. Wang, M.D. Lyu, L.C. Juang, S.S. Liu and S.H. Hung, *J. Colloid Interface Sci.,* 316 (2007) 562-569.

[21] H. Zhu, X. Gao, Y. Lan, D. Song, Y. Xi and J. Zhao, *J. Am. Chem. Soc.,*126 (2004) 8380-8381.

[22] E. Jr. Morgado, M.A.S. De-Abreu, O.R.C. Pravia, B.A. Marinkovic, P.M. Jardim, F.C. Rizz and A. S. Araujo, *Solid State Sci.,* 8 (2006) 888-900

[23] Y. Wang, T. Sun, D. Yang, H. Liu, H. Zhang, X. Yao and H. Zhao, *Phys. Chem. Chem. Phys.,* 14 (2012) 2333-2338.

[24] F.C. Lizana, S.G. Quero, H. Idriss and M.A. Keane, *Catal. Sci. Technol.* 1 (2011) 652-661.

[25] F.C. Lizana, S.G. Quero, H. Idriss and M. A. Keane, *J. Catal.,* 268 (2009) 223-234.

[26] S. Sondhia and B. Singhai, *Bull. Environ. Contam. Toxicol.,* 80 (2008) 423-427.

[27] Y.V. Kolenko, K.A. Kovnir, A.T. Gavrilov, A.V. Garshev, J. Frantti, O.I. Lebedev, B.R. Churagulov, G.V. Tendeloo and M. Yoshimura, *J. Phys. Chem. B* 110 (2006) 4030-4038.

[28] J. Yang, Z. Jin, X. Wang, W. Li, J. Zhang, S. Zhang, X. Guo and Z. Zhang, *Dalton Trans.,* (2003) 3898-3901.

[29] T. Ahmad, S. Vaidya, N. Sarkar, S. Ghosh and A.K. Ganguli, *Nanotechnology,* 17 (2006) 1236-1240.

[30] A.F. Thunemann, J. Kegel, J. Polte and F. Emmerling, *Anal. Chem.,* 80 (2008) 5905-5911.

[31] B.J. Borah, A. Yadav and D.K. Dutta, *J. Biomed. Nanotechnol.,* 7 (2011) 152-153.

[32] J. Yang, J.H. Zeng, S.H. Yu, L. Yang, G.E. Zhou and Y.T. Qian, *Chem. Mater.,* 12 (2000) 3259-3263.

[33] P.D. Cozzoli, A. Kornowski and H. Weller, *J. Am. Chem. Soc,.*125 (2003)14539-14538.

[34] A. Yamakata, T.A. Ishibashi and H. Onishi, *J. Phys. Chem. B,* 105 (2001) 7258-7262.

[35] Y.X. Liu, J.X. Chen and J.Y. Zhang, *Chin. J. Chem. Eng.,* 15 (2007) 63-67.

[36] C.C. Wang, Z. Zhang and J.Y. Ying, *Nanostruct. Mater.,* 9 (1997) 583-586.

[37] S.O. Flores, O.R. Bernij, M.A. Valenzuela, I. Corvada, R. Gomez and R. Gutierrez, *Top. Catal.* 44 (2007) 507-511.

5. Photomineralization and mechanistic study of Imidacloprid insecticide by Ag deposited sodium titanate nanotubes

5.1 Introduction

Highly porous monoclinic TNT possessing high surface area, interlayer water molecules, scroll structure, thin wall thickness favoring better charge transport and charge diffusion properties has been studied for the photocatalytic degradation [1-9] of many organic pollutants. Generally, TNT exhibits higher PCA [3-5,7,8] than commercially available most photoactive P25. For instance, Zhu et al. [3] and Antoino et al. [4] showed its 5 and 7 times higher activity than P25 for degradation of sulforhodamine and methyl red dyes, respectively. Literature reports [1-6,10] also support that PCA of TNT is influenced by Na-content in its crystal structure and calcination temperatures. For example, Morgado et al. [6] demonstrated that TNT having 2-5 wt% of Na can show improved PCA for oxidation of rhodamine-B, while Qumar et al. [1] showed its negligible and higher PCA at below and above 300 ^{o}C of calcination temperature, respectively. However, calcination of TNT at > 700-800 ^{o}C transforms it into orthorhombic nanorods with change in Ti-O bond length, having much less surface area and de-hydroxylated surface with a decent PCA [7-9] to that of P25.

This PCA of TNT is well known to be improved loading/intercalating metals (Au, Ag, Pt, Rh, Fe, Ru etc.,) onto/into the TNT particles [11-14]. At the interface of metal-TNT, development of space charge region retards the recombination of excited charge carriers and increases the PCA. For example, Tsai et al. [14] showed improvement in PCA of TNT for photooxidation of CO after incorporation of Au (0.39-2.53 wt%). Hence, TNT despite having Na (generally decrease the activity of TiO_2 catalyst) and high temperature treatment was proven to show better activity than P25 for degradation of dyes, therefore can degrade other large heteroatom(s) containing molecules such as pesticides and has been recently studied by our group [7,8] .

There are varieties of pesticides containing heteroatom(s) that are being used in India, especially in states of Punjab and Haryana. However, under the natural conditions, decomposition of pesticides is slow and incomplete, e.g., IMI. This pesticide has high water solubility (550 mg/l), half-life ($t_{1/2}$) = 40-60 days [7], and degrades to intermediates [15-18] which are sometimes more toxic and persistent than IMI itself, resulting in plausible threat for

ecological system. Therefore, its photocatalytic degradation [15-25] using P25 have been performed, revealing its incomplete mineralization and the presence of heteroatom containing persistent intermediates that may require longer time of light exposure for complete decomposition. As the presence of heteroatom(s) in the intermediate(s) can influence stability of a molecule by phenomenon of *"resonance"*, hence it is worth to study the role of these atoms in the formation/transformation of IMI's intermediates and their final mineralization to the inorganic ions. Hence, present work considers the PCA of bare and Ag-loaded (0.2-1.0 wt%) TNT in relation to P25 for the photo mineralization of IMI to CO_2, including quantitative estimation of the fate of its heteroatoms (N, O and Cl) to inorganic ions and identification of its photoproduced intermediates. A possible mechanistic path way for the mineralization and transformation of IMI's intermediates into one-another, and a chemical mass balanced equation in comparison to its theoretically expected equation after its complete oxidation is being proposed and described in this chapter.

5.2 Experimental section

5.2.1 Synthesis and characterization of bare and Ag-loaded TNT: Bare and Ag (0.2-1.0 wt%) photodeposited TNT was synthesised as per method reported in *section-2.2.1*and *section-2.2.2*, respectively of chapter-2. The morphological analysis was performed by TEM (*section-2.5.3*), technique as described in chapter-2.

5.2.2 Photocatalytic activity: It was carried out as described in *section-2.6.1* of chapter-2. The reaction samples obtained after UV-light illumination were analysed by HPLC (*section-2.6.2*), GC (*section 2.6.3*) and Ion chromatograph (*section-2.6.5*) as described previously in chapter-2. The intermediates identified by GC-MS (*section 2.6.4of chapter-2*) are abbreviated as I-1to I-8.

5.3 Results and discussion

Morphological analysis of TNT (Fig. 5.1 a-b), revealed the formation of open ended straw like nanotubes having length (L) = 80-115 nm and diameter (D) = 8-13 nm, as found in chapter-3 (*section-3.3*). Whereas, Ag nanoparticles of narrow size (3-5 nm) distribution at the surface of many TNT particles are distinctly noticed in many 0.5-Ag-TNT sample.

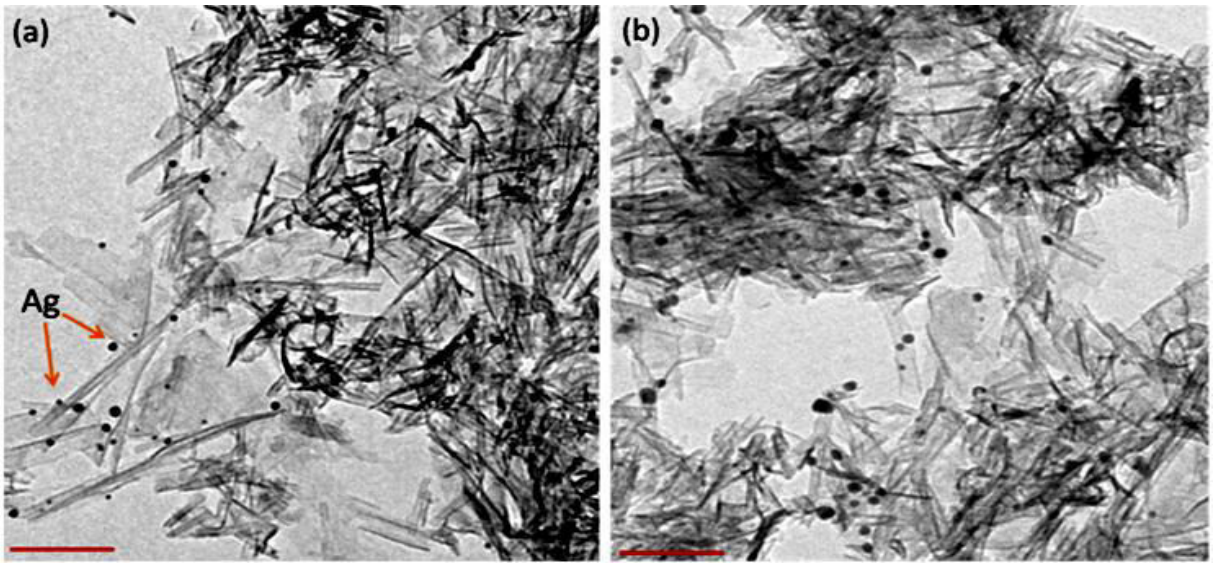

Fig. 5.1 (a and b) TEM images for 0.5 wt% Ag photodeposited sodium titanate nanotubes; scale bar = 100 nm.

Time course PCA of bare and Ag-loaded TNT in relation to P25 is shown in Fig. 5.2. It is observed that TNT exhibited higher activity than P25 and is in consistency with our [7,8] and other reports [3-5]. However, Ag-loading increases the activity of TNT upto 0.5 wt% of its loading and beyond this amount it decreases the activity of TNT for degradation of IMI. Photooxidation of IMI was found to follow pseudo-first order kinetics (section-2.6.6 of chapter-2) with highest value of apparent rate constant (k) of 2.2×10^{-2} min^{-1} for 0.5-Ag-TNT catalyst. The half-life of IMI was found (*section-2.6.6 of chapter-2*) to be only ~32 min by using 0.5-Ag-TNT as a photocatalyst notably much lower in relation with TNT (~103 min) and P25 (~204 min) catalysts, under similar reaction conditions.

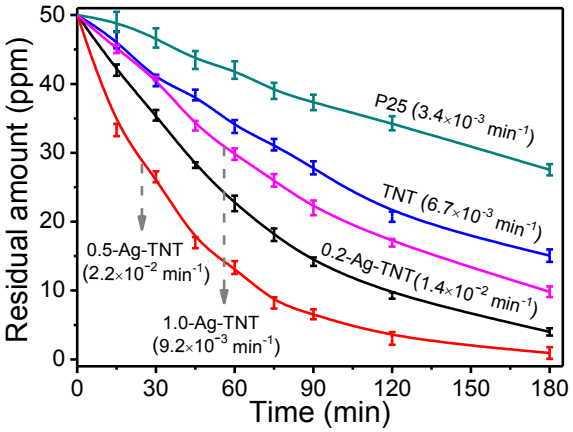

Fig. 5.2 Time course study and pseudo-first order decay constants for photocatalytic degradation of imidacloprid using various catalysts.

Time course GC-MS (Fig. 5.3) analysis showed a gradual decrease in peak height for IMI along with appearance of some new peaks, each belonging to different intermediate. Some of

these intermediates were identified by their mass spectra (Fig. 5.4a-b). There is a complete disappearance of peak corresponding to IMI (at retention time (R_t) = 11.2 min, Fig. 5.3) after 180 min of its photooxidation in presence of 0.5-Ag-TNT catalyst, however it was present while using bare TNT under similar experimental conditions, confirming better activity of the former catalyst.

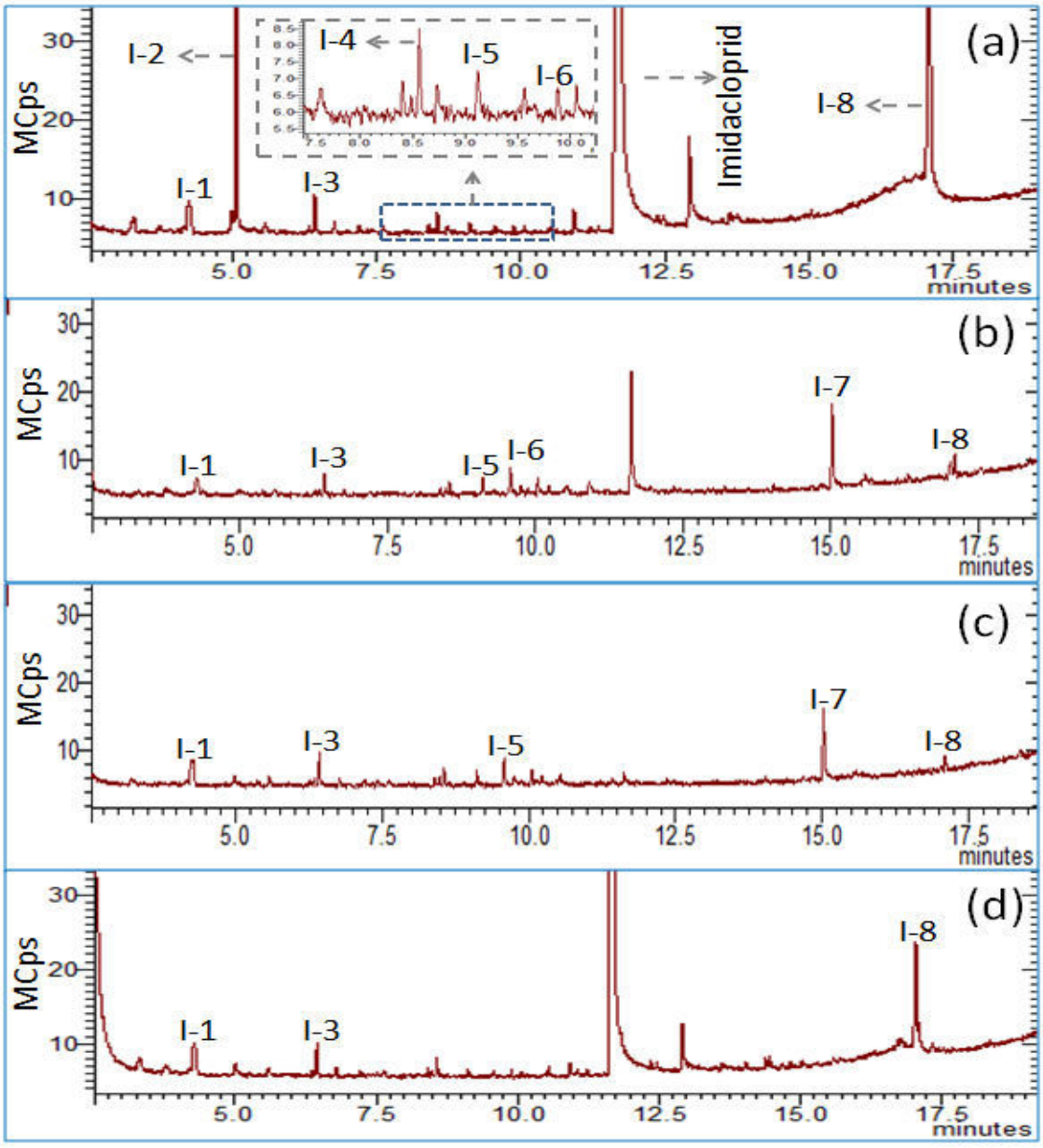

Fig. 5.3 Gas Chromatographs for identified intermediates (I-1 to I-8) obtained after photocatalytic degradation of imidacloprid using 0.5 wt% Ag-photodeposited sodium titanate nanotubes after (a) 30 min, (b) 120 min, (c) 180 min, in comparison to (d) bare sodium titanate nanotubes after 180 min; inset: corresponding enlarged view.

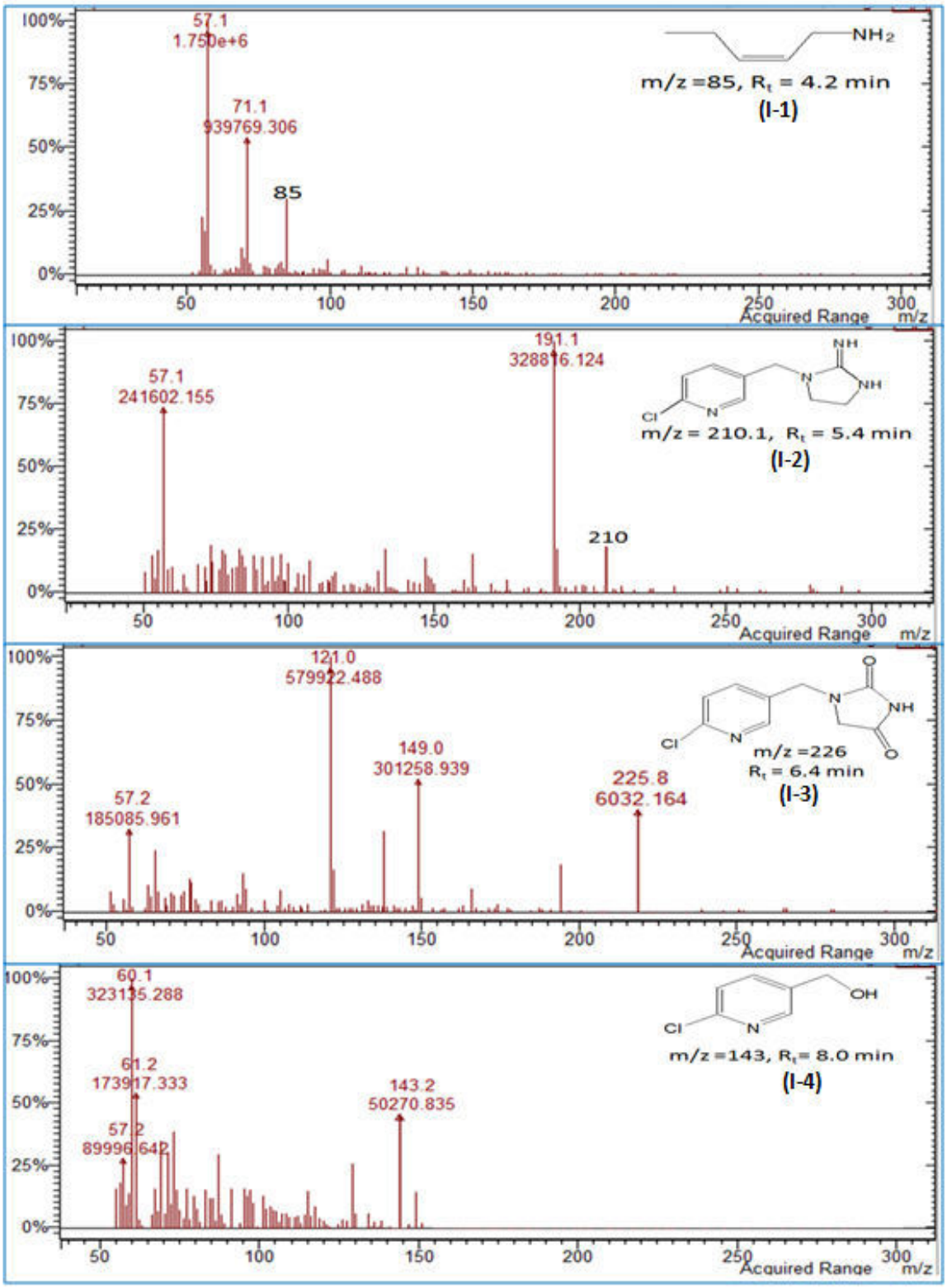

Fig. 5.4a Mass spectrum for identified intermediates (I-1 to I-4); inset: retention time (R_t) as per gas chromatographs, molecular structure and mass/charge ratio (m/z).

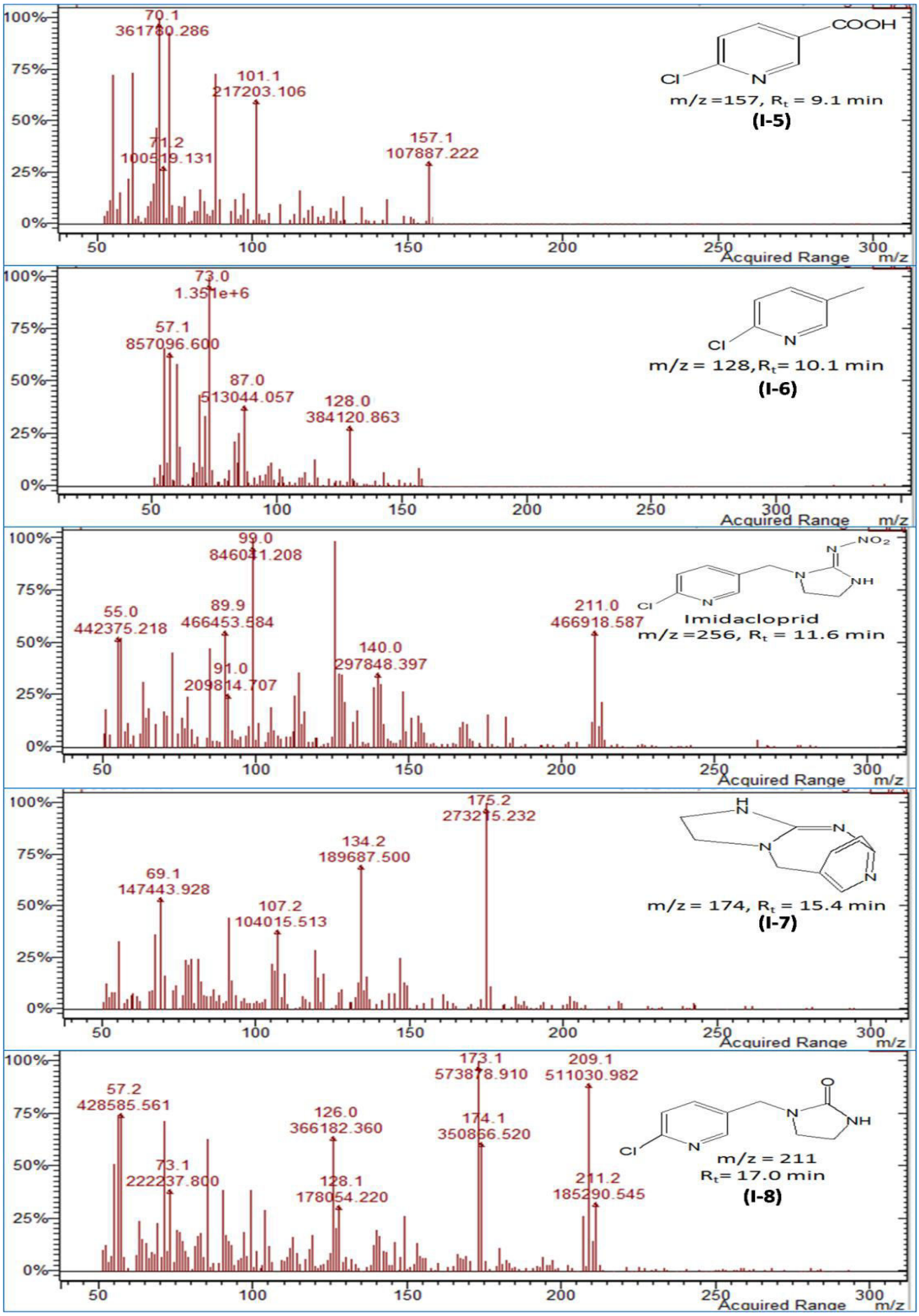

Fig. 5.4b Mass spectrum for identified intermediates (I-5 to I-8); inset: retention time (R_t) as per gas chromatographs, molecular structure and mass/charge ratio (m/z).

The quantitative estimation for CO_2 formation (Fig. 5.5) during degradation of IMI by various catalysts was found to follow trends similar to its photooxidation. The highest amount of CO_2 formation by 0.5-Ag-TNT catalyst of highest pseudo-first order rate constant (2.4×10^{-3} min^{-1}) corresponds to ~70% of its actual mineralization despite of its complete oxidation. This incomplete mineralization of IMI is because of existence of intermediates found (Fig. 5.3 and 5.4a-b) to be present after 180 min of its photooxidation.

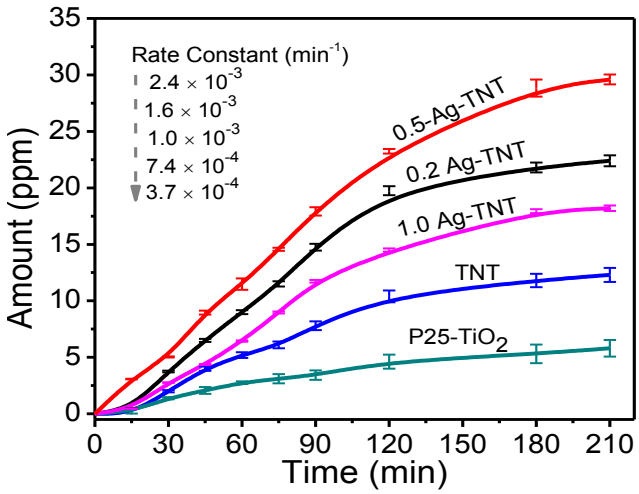

Fig. 5.5 Time course of CO_2 formation during the photooxidation of imidacloprid by different catalysts.

Investigation for the fate of heteroatoms showed that the amount of inorganic ions formed by 0.5-Ag-TNT are higher than that for P25 (Fig. 5.6). It is also noticeable that, amount of inorganic ions increases with increase in time of irradiation, again confirming the mineralization IMI during its photodegradation.

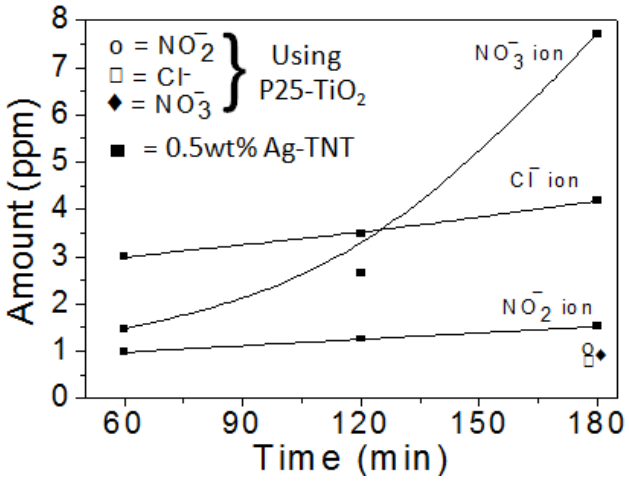

Fig. 5.6 Evolution of inorganic ions during photooxidation of imidacloprid by 0.5 wt% Ag photodeposited TNT and bare P25.

The stoichiometric balanced chemical equation (eq. 5.1) formulated from the obtained results is found to deviate from theoretical equation 5.2, evidencing incomplete mineralization of IMI. The increase in amount of nitrate ion formation with irradiation time is probably due to the mineralization of the imidazole or pyridine substituted ring(s). These results are in correlation with previous report [27] for dissipation of cyrpoconazole, where the nitrogen atoms present in the triazole moiety were found to decompose to nitrate and ammonium ions.

$$C_9H_{10}N_5O_2Cl + \frac{5}{2}O_2 \xrightarrow[h\nu\ (180\ min)]{} 2.88\ CO_2 + 0.04\ NO_2 + 0.62\ NO_3 + 0.6\ Cl + \text{Intermediates}$$

.....eq. 5.1

$$C_9H_{10}N_5O_2Cl + \frac{33}{2}O_2 \longrightarrow 9CO_2 + 5NO_3^- + Cl^- + 6H^+ + 2H_2O$$

.....eq. 5.2

These results suggest that the PCA of TNT with Ag-depositions were enhanced remarkably, certainly, with an optimum amount (0.5 wt%) of the silver. With higher amount of Ag-photodeposition, the metal would rapidly become the recombination center for e^-/h^+ pairs and consequently diminishes the PCA. Moreover, Ag being plasmonic [28] nanostructure supports the formation of resonant surface plasmons in response to a photon flux that in-turn could yield a high concentration of e^-/h^+ pairs in Ag-TNT samples. The formation of such plasmonic nanostructures also allow the selective formation of e^-/h^+ pairs at the interface of Ag-TNT which could readily separate these carriers from each other and easily migrate [28-30,33] to the surface, where they can carry out PCA. As loaded Ag is well known [28,31] to improve the adsorption capacity of TiO_2 for molecular oxygen, therefore, it can scavenge more conduction band electrons by the formation of highly oxidative super oxide radicals. Whereas, h^+ react with absorbed surface -OH group and/or H_2O molecules to form hydroxyl radicals possessing high oxidizability and causing the improved PCA of Ag-loaded TNT nanoparticles.

Since, variety of intermediates are formed during photooxidation of IMI, therefore, various possible attack positions for hydroxyl radical leading to the formation of identified intermediatesare shown in Fig. 5.7a and are being discussed below:

The N-N (at positions N1and N2) and C-N (at C-1) bond (Fig. 5.7a) in IMI yielding intermediates I-2 and I-4 (Fig. 5.7b) appear to be the primary attack sites by hydroxyl radical during its photooxidation. The intermediate I-2 thus formed could be degraded to I-6 via attack of hydroxyl radical on its bridging C-N bond. On the other hand, intermediate I-4 which is a 1^o alcohol could be oxidized to corresponding acid (I-5). Alternatively, the hydrolysis of IMI (Scheme-5.1) could result in the formation of intermediate I-8, and its successive oxidation at C-2 position of imidazole ring result in I-3.

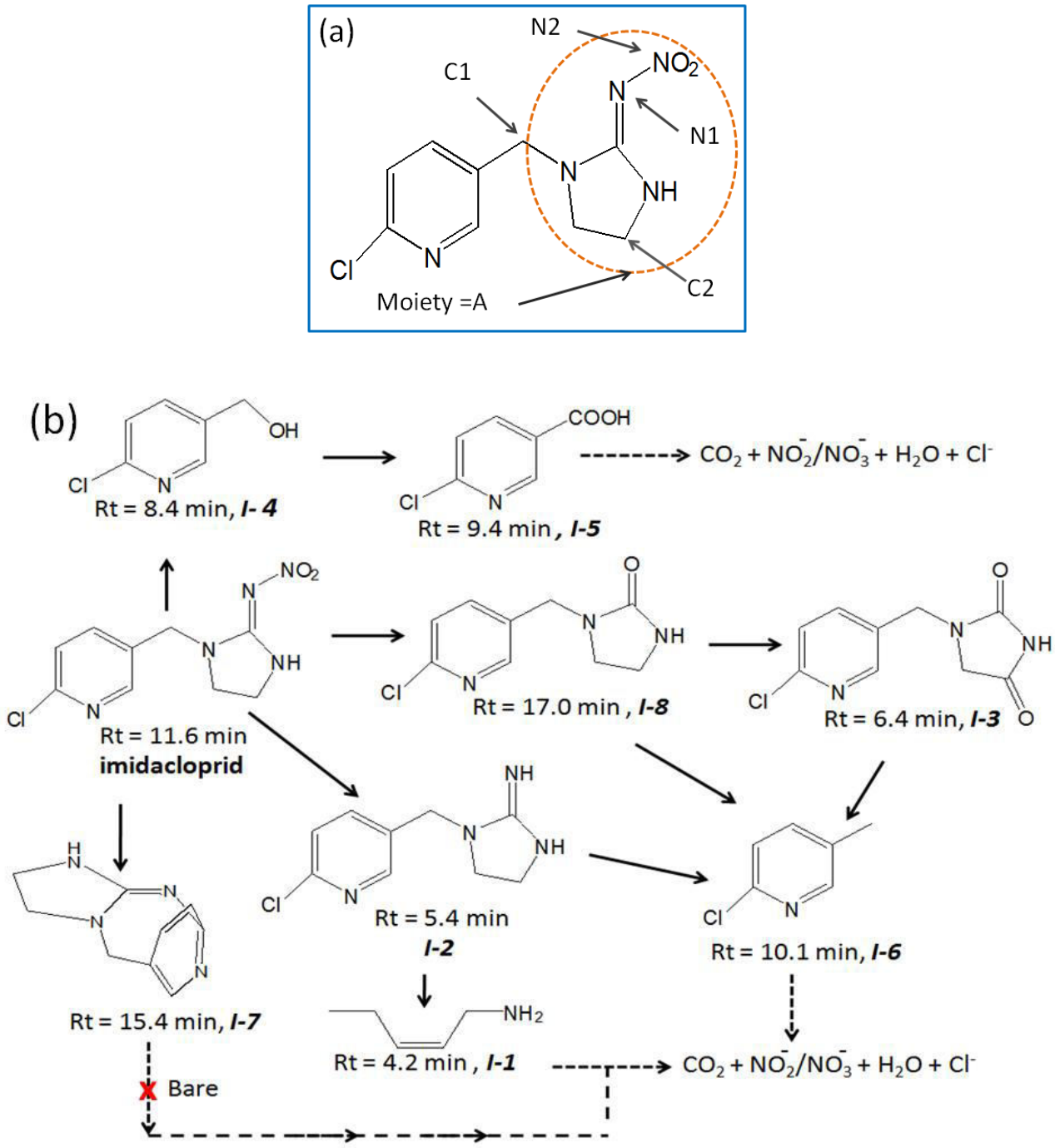

Fig. 5.7 (a) Various attack positions by hydroxyl radicals at imidacloprid and (b) probable pathway proposed for degradation of imidacloprid.

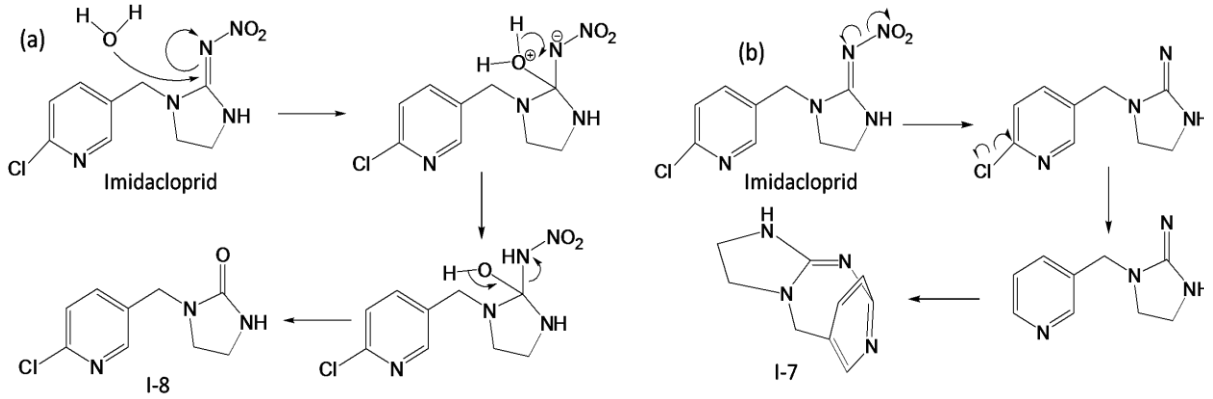

Scheme 5.1 Mechanism for formation of intermediates (a) I-8 and (b) I-7 after photooxodation of imidacloprid.

The formation of intermediate I-6 believed to be via fragmentation of I-3 is reported to be an intermediate product [26] of IMI photooxidation. Interestingly, I-7 formed (Scheme 5.1b) by rearrangement and de-chlorination of IMI was identified in case of Ag-loaded samples, in the present study. This could be attributed to the fact that (i) this intermediate is formed in the bare sample in such a small amount that it remains below the detection limit of GC-MS and (ii) as the samples are analyzed after regular time intervals, during which it may have formed/consumed/transformed into some other product. Since, there is evolution of CO_2 and formation of inorganic ions during the photooxidation of IMI, therefore it is believed that these intermediates further oxidize to smaller compound(s) and eventually got mineralized. Similar to these identified intermediates, previous studies also identified these intermediates [15,18,26] during the photooxidation of IMI by using P25. However, the extent of IMI mineralization [32] was 14-29% which is at-least 1.7 times less than that found in the present study, revealing the improved efficiency of as-prepared catalysts than P25.

In-order to further support the proposed mechanism, kinetic analysis of intermediates was carried out (Fig. 5.8a-c) and because of unavailability of the authentic intermediates, the kinetic data was related to the ratio of peak area at any time ($Area_{(t)}$) to the maximum of peak area ($Area_{(max)}$). Intermediates I-2, I-4 and I-8 appear promptly and after 30 min they reach to maximum concentration before being degraded in turn. Whereas, their corresponding transformed intermediates were found to be at their maximum level after 15-30 min of photooxidation of the parent intermediates. Afterwards, they start disappearing and within 180

min of photooxidation they almost leveled off, except for I-2 and I-5. The existence of these heteroatom containing intermediates (I-3 and I-5) even after complete degradation of IMI, signifies their stability in the reaction solution and are believed to be a cause for the incomplete mineralization for IMI.

5.4 Conclusions

It has been demonstrated in this chapter that Ag-photodeposition improves the PCA of TNT for mineralization of IMI. The formation of a number of identified intermediates revealed the existence of various oxidation routes for decomposition of IMI.

5.5 References

[1] M. Qamar, C.R. Yoon, H.J. Oh, N.H. Lee, K. Park, D.H. Kim, K.S. Lee, W.J. Lee and S.J. Kim, *Catal. Today,* 131 (2008) 3-14.

[2] M. Qamar, C.R. Yoon, H. Jho, D.H. Kim, J.H. Jho, K.S. Lee, W.J. Lee, H.G. Lee and S.J. Kim, *Nanotechnology,* 17 (2006) 5922-5929.

[3] H. Zhu, X. Gao, Y. Lan, D. Song, Y. Xi and J. Zhao, *J. Am. Chem. Soc.,* 126 (2004) 8380-8381.

[4] J.A.T. Antonio, M.A.C. Jacome, S.L.O. Cerros, E.M. Palacios, R.S. Parra, C.A. Chavez, J. Navarete and E.L.Salinas, *Appl. Catal. B Environ.* 100 (2010) 47-54.

[5] G. Potari, D. Madarasz, L. Nagy, B. Laszlo, A. Sapi, A. Oszko, A. Kukovecz, A. Erdohelyi, Z. Konya and J. Kiss, *Langmuir,* 29 (2013) 3061-3072.

[6] E. Jr. Morgado, M.A.S. de-Abreu, O.R.C. Pravia, B.A. Marinkovic, P.M. Jardim, F.C. Rizzo and A.S. Araujo, *Solid State Sci.,* 8 (2006) 888-900.

[7] I.S. Grover, S. Singh and B. Pal, *Appl. Surf. Sci.,* 280 (2013) 366-372.

[8] I.S. Grover, S. Singh and B. Pal, *J.Nanosci. Nanotechnol.,* doi:10.1166/jnn.2014.9072

[9] V. Stengl, S. Bakardjieva, J. Subrt, E. Vecernıkova, L. Szatmary, M. Klementova and V. Balek, *Appl. Catal. B Environ.,* 63 (2005) 20-30.

[10] D.V. Bavykin, J.M. Friedrich and F.C. Walsh, *Adv. Mater.* 18 (2006) 2807-2824.

[11] X. Ding, X.G. Xu, Q. Chen and L.M. Peng, *Nanotechnology,* 17 (2006) 5423-5427.

[12] X. Si, F. Li, L. Sun, F. Xu, S. Liu, J. Zhang, M. Zhu, L.Z. Ouyang, D. Sun and Y.L. Liu, *J. Phys. Chem. C,* 115 (2011) 9780-9786.

[13] D.V. Bavykina, A.A. Lapkinb, P.K. Plucinskib, L.T. Murcianob, J.M. Friedricha and F.C. Walsh, *Top. Catal.,* 39 (2006) 3–4.

[14] J.Y. Tsai, J.H. Chao and C.H. Lin, *J. Mol. Catal. A Chem.,* 298 (2009) 115-124.

[15] V. Guzsvany, N. Banic, Z. Papp, F. Gaal and B. Abramovic, *React. Kinet. Mech. Catal.,* 99 (2010) 225-233.

[16] M.P. Halm, A. Rortais, G. Arnold, J.N. Tasei and S. Rault, *Environ. Sci. Technol.,* 40 (2006) 2448-2454.

[17] P. Medrzycki, R. Montanari, L. Bortolotti, A.G. Sabatini, S. Maini and C. Porrini, *Bull. Insectology,* 56 (2003) 59-62.

[18] H. Wamhoff and V. Schneider, *J. Agric. Food Chem.,* 47 (1999) 1730-1734.

[19] N. Philippidis, S. Sotiropoulos, A. Efstathiou and I. Poulios, *J. Photochem. Photobiol. A Chem.,* 204 (2009)129–136.

[20] J. Marugan, M.J.L. Munoz, W. Gernjak and S. Malato, *Ind. Eng. Chem. Res.* 45 (2006) 8900-8908.

[21] S. Malato, J. Caceres, A. Aguera, M. Mezcua, D. Hernando, J. Vial, A.F. Alba, *Environ. Sci. Technol.,* 35 (2001) 4359-4366.

[22] R. Zabar, T. Komel, J. Fabjan, M.B. Kralj and M. Trebse, *Chemosphere,* 89 (2012) 293-301.

[23] O. Malev, R.S. Klobucar, E. Fabbretti and P. Trebse, *Pest. Biochem. Physiol.,*104 (2012) 178-186.

[24] S.R. Jadhav, V.K. Saharan, D. Pinjari, S. Sonawane, D. Saini and A. Pandit, *J. Hazard. Mater.,* 261 (2013) 139-147.

[25] W.P. Liu, W. Zheng and J.Y. Gan, *J. Agric. Food Chem.,* 50 (2002) 6823-6827.

[26] D. Redlich, N. Shahin, P. Ekici, A. Friess and H. Parlar, *Clean,* 35 (2007) 452-458.

[27] L. Lhomme, S. Brosillon and D. Wolbert, *J. Photochem. Photobiol. A Chem.,* 188 (2007) 34-42.

[28] X. Zhang, Y.L. Chen, R.S. Liu and D.P. Tsai, *Rep. Prog. Phys.,* 76 (2013) 46401-46442.

[29] T.M. Inerbaev, J.D. Hoefelmeyer and D.S. Kilin, *J. Phys. Chem. C,* 117 (2013) 9673-9692.

[30] C. Balasanthiran and J.D. Hoefelmeyer, *Chem. Commun.,* 50 (2014) 5721-5724.

[31] X.Chen and S.S. Mao, *Chem. Rev.,* 107 (2007) 2891-2959.

[32] V. Kitsiou , N. Filippidis, D. Mantzavinos and I. Poulios, *Appl. Catal. B Environ.,* 86 (2009) 27-35.

[33] A. Kumar and N. Mathur, *Appl. Catal. A* 275 (2004) 189-197.

6. Au impregnated sodium titanates and their physico-chemical properties

6.1 Introduction

As discussed in *sections-3.1, -4.1 and -5.1* during the present study and other reports [1-6] indicating that TNT having layered structure, hollow-porous morphology and higher surface area, generally exhibited flexible PCA depending upon sodium content, crystal phase, and sintering temperature. Studies reveal that tubular morphology of TNT particles (with Na-content = 3-5 wt%) was retained when calcined at 200-450 ^{o}C, indicating its thermal stability within this temperature range, showing higher PCA [1,5] than the mostly active P25. However, with further increase in calcination temperature ~ 700-800 ^{o}C, the hollow interior of TNT starts collapsing leading to the formation nanorod shaped particles exhibiting almost similar photoactivity to P25 catalyst [7,8] and is also discussed in chapter-5.

The PCA of TNT was further enhanced with transition metal (Fe, Ni, Pt, Au, Ru etc.) impregnation followed by sintering at 200-450 ^{o}C [9-13]. It has reported [9,11,12,14] that incorporation of metals (Fe, Au, Ni) into hollow interior of TNT facilitates the formation of core-shell structure that improved the lifetime of photoexcited e^{-}/h^{+} pair, hence the photocatalytic activity. For instance, Fe [11] and Au [12] incorporated TNT were reported to 5.0 and 7.6 times more photoactive than bare TNT for the photooxidation of CO and H_2 production, respectively, where no significant change in either morphology or crystal structure was observed. However, the effect of these impregnated metals followed by calcination beyond 450 ^{o}C have been rarely reported, and is expected [15,16] to cause deformations in crystal structure/morphology during calcination. The metal may induce a strain in the crystal structure [15] or decrease the surface free energy [16] of TNT, that may interfere with its crystal growth during calcination. Very recently, a report by Portai et al. [17] demonstrated that calcination of Rh deposited TNT at 600 ^{o}C led to formation of nanoparticles of size ~ 10 nm instead of any elongated morphology like solid TNT(S) formed during calcination of bare TNT [1-6]. In this context, present chapter demonstrates that the calcination of Au photodeposited Au^{3+} and Au nanospheres (3-5 nm) impregnated TNT under atmospheric conditions at ~ 800 ^{o}C for 2 h led to the formation of a variety of geometrical morphologies e.g., nanopolygons like heptagons, hexagons, pentagons, etc. These nanoparticles were found to possess different crystal structures (monoclinic,

orthorhombic and rhombohedral) and phase compositions in comparison to monoclinic TNT(S) particles which are obtained after sintering of orthorhombic TNT without Au loading, under similar conditions. The formation of versatile crystal geometries, allowed to explore the crystal phase dependent photocatalytic activity relative to the mostly studied anatase, anatase-rutile, rutile and brookite TiO_2 phases. Hence, various physicochemical properties of as-prepared titania nanocomposites were briefly investigated for the photooxidation of neurotoxic [18-21] insecticide IMI to plausible intermediate products that mineralize to CO_2 under different periods of UV-light irradiation.

6.2 Experimental

6.2.1 Synthesis of bare and Au-loaded TNT: Bare TNT was synthesized as reported in *section-2.2.1* of chapter-2. The Au-loading was achieved by (i) adding Au^{+3} ions during synthesis of TNT (TNT-Au^{+3}(I)), followed by (ii) irradiation under UV-light (TNT-Au^{o}(P)) and (ii) by stirring with AuNP (TNT-NP(M)), as described in *section-2.4.2* of chapter-2. These Au-loaded TNT particles were calcined at 800 ^{o}C in comparison to its bare analogy (*section-2.2.6*), and are termed by adding **"S"** as suffix in their respective abbreviations i.e., TNT-Au^{+3}(IS), TNT-Au^{o}(PS) and TNT-Au(MS). These as-prepared catalysts were characterized by XRD (*section-2.5.1*), EDS (*section-2.5.2*), TEM (*section-2.5.3*) and S_{BET} (*section-2.5.10*) techniques as described in chapter-2.

6.2.2 Photocatalytic activity: It was assessed by degradation of IMI to CO_2 as per method reported in *section-2.6.1* of chapter-2. The reaction samples were analyzed by HPLC (*section-2.6.4*), GC (*section-2.6.5*) and LC-MS (*section-2.6.8*) techniques and are discussed in chapter-2.

6.3 Results and discussion

The as-prepared TNT was found to possess monoclinic crystal structure for $Na_2Ti_3O_7$ (tritianate, Fig. 6.1a) as evidenced (ICSD card no.00-014-0085) by its characteristic peak at $2\theta = 10.0015^{o}$ for (101) plane. The calcination of bare TNT caused its transformation to nanorod particles of monoclinic $Na_2Ti_6O_{13}$ (hexatitanate, Fig. 6.1b) crystal structure. The TEM image of TNT (Fig. 6.1c) and TNT(S) (Fig. 6.1d) show tubular and rod like morphology and their corresponding SAED patterns Fig. 6.1c (inset) and Fig. 6.1d (inset) indicates their amorphous and crystalline nature, respectively, and are in accordance with their respective XRD.

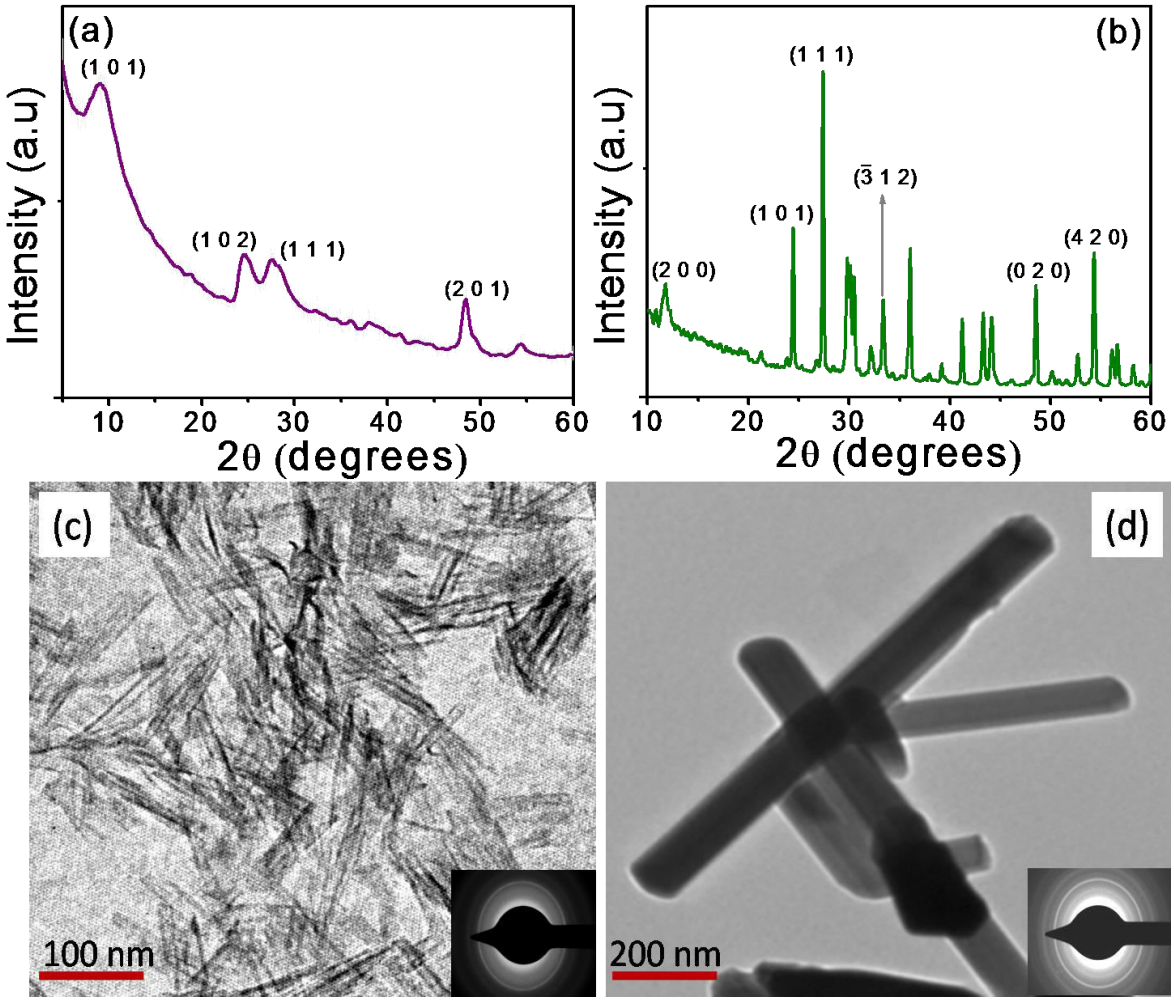

Fig. 6.1 Comparative XRD pattern of TNT (a) before and (b) after calcination at 800 °C, with their corresponding TEM images (c and d) and SAED patterns (insets).

The XRD pattern (Fig. 6.2a) of sample TNT-Au^{+3}(I) is found to be almost similar to TNT (Fig. 6.1a). Whereas, TNT-Au^{+3}(I) sample after calcination (TNT-Au^{+3}(IS), Fig. 6.2b) was found to be a mixture of well crystalline, strained $Na_2Ti_9O_{19}$ (nonatitanate, ICSD Card No. 01-073-2256), $Na_2Ti_6O_{13}$ (hexatitanate) and $NaTiO_2$ (monotitanate, ICSD Card No. 00-016-0251) crystal structures (Table 6.1). Interestingly, deviation in lattice parameters (Table 6.1) and shift in characteristic peaks for nonatitanate ($2\theta = 24.71^{\circ}$ to 24.81°), hexatitanate ($2\theta = 11.84^{\circ}$ to 11.92°), and monotitanate ($2\theta = 40.67^{\circ}$ to 40.72°) were found corresponding to (110), (200) and (104) plane, respectively. These deviations in 2θ and lattice parameters might be due to exchange of Na^{+} ions by Au^{+3} ions. For a 6-fold coordinated ion the radius of Na^{+} ions (1.12 Å) is more than

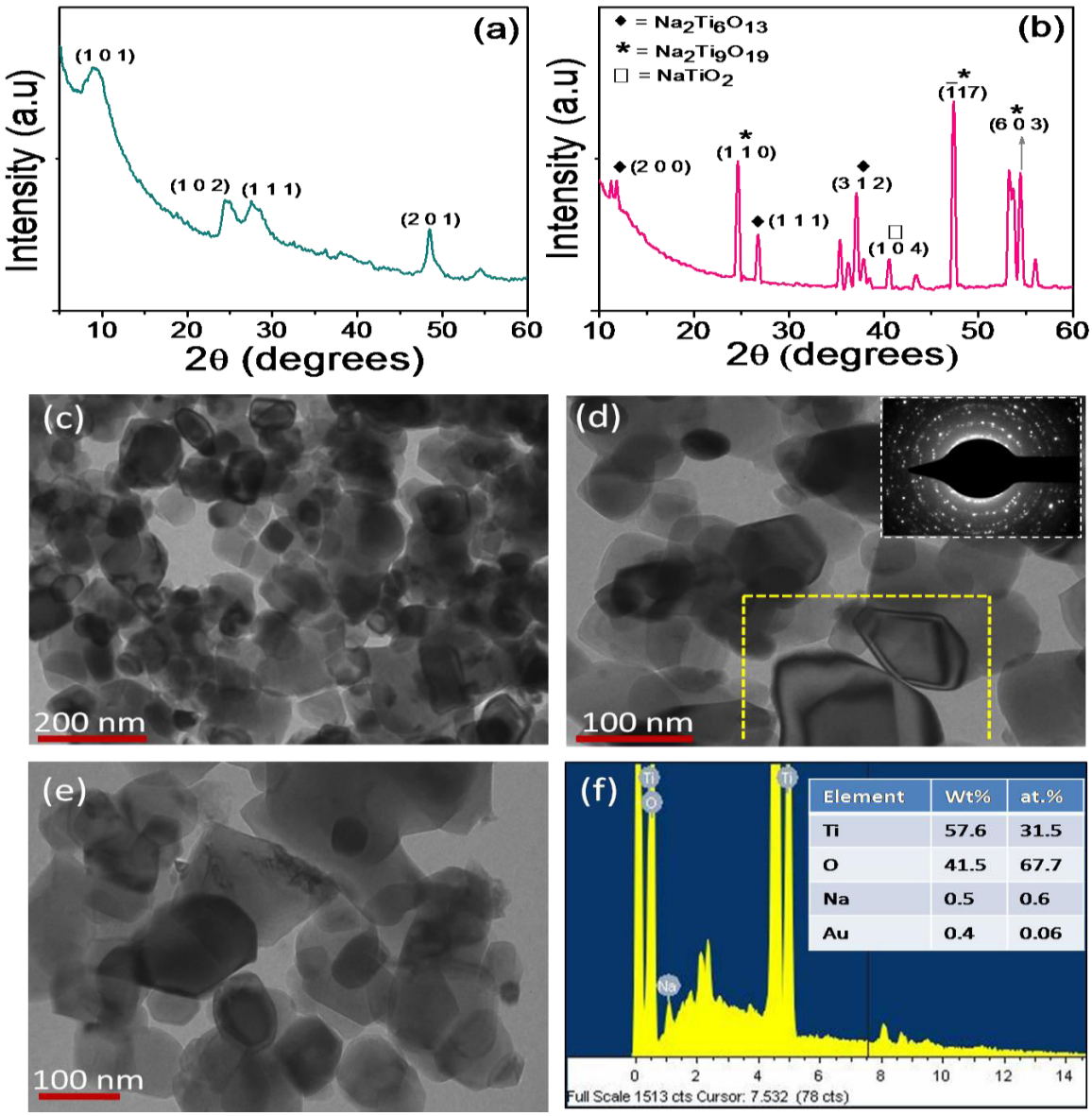

Fig. 6.2 XRD pattern of 0.5 wt% Au-insitu-sodium titanate nanotubes (a) before and (b) after calcination at 800 °C, with TEM images of later one (c-e) and its corresponding SAED pattern (inset), and (f) its EDS pattern

radius of Au^{+3} (0.85 Å), hence the exchange of the former with the later ion resulted in the compression strain ca. 6.9×10^{-3} in crystal structure of TNT-Au^{+3} (I), and subsequently causing variation in physico-chemical parameters (Table 6.1). The morphology (Fig. 6.2c-d) of TNT-Au^{+3}(IS) is entirely different from TNT(S) revealing it to be of asymmetric nanopolygons, with its SAED pattern (inset Fig. 6.2d) exhibiting crystalline nature as found in XRD pattern.

Table 6.1. Various physico-chemical parameters of different as-prepared nanostructures.

Various catalysts	Chemical composition (crystal structure %)	Lattice parameters (Å) Calculated (reported)			EDX analysis Elements (wt%)				Compression Strain	Average relaxation time (μS)
		a	b	c	Na	Ti	O	Au		
TNT	$Na_2Ti_3O_7$	8.4	3.7	9.0	3.02	57	39	--	7.4×10^{-4}	41
	(monoclinic)	(8.5)	(3.8)	(9.1)						
TNT(S)	$Na_2Ti_6O_{13}$	15.2	3.7	9.1	2.61	58.9	38.4	--	1.5×10^{-4}	68
	(monoclinic)	(15.1)	(3.7)	(9.1)						
TNT-Au^{+3} (IS)	$Na_2Ti_9O_{19}$	12.2	3.7	15.7	0.15	60.6	38.9	0.3	1.5×10^{-3}	64
	(monoclinic, 95%)	(12.2)	(3.7)	(15.6)						
	$NaTiO_2$	2.9	3.0	16.2					1.1×10^{-3}	
	(rhombohedral, 5%)	(3.0)	(3.0)	(16.2)						
TNT-Au^0(PS)	TiO_2 (Anatase, 78%)	12.2	3.7	15.6	0.24	59.5	39.7	0.4	2.4×10^{-2}	81
		(12.2)	(3.5)	(15.6)						
	TiO_2 (Rutile, 22%)	3.0	3.0	16.2					2.8×10^{-2}	
		(2.8)	(2.9)	(16.2)						
TNT-NP(MS)	$Na_2Ti_9O_{19}$	12.2	3.7	15.6	0.57	57.8	41.5	0.04	0.9×10^{-4}	71
	(monoclinic, 26%)	(12.2)	(3.7)	(15.6)						
	$NaTiO_2$	3.0	3.0	16.1					0.1×10^{-4}	
	(rhombohedral, 46%)	(3.0)	(3.0)	(16.2)						
	$Na_2Ti_3O_7$	19.3	3.7	3.0					0.2×10^{-4}	
	(orthorhombic, 28%)	(19.3)	(3.7)	(3.0)						

The presence of Au in TNT-Au^{+3}(IS) is further confirmed by EDS pattern (Fig. 6.2f), where 0.4 wt% of Au was found to be present along with Na (0.5 wt%), Ti (57.6 wt%) and O (41.5 wt%). The measured S_{BET} of TNT-Au^{+3}(I) (160 m^2g^{-1}) was found to decrease to 28 m^2g^{-1} after its (TNT-Au^{+3}(IS)) sintering that can be ascribed to the formation of highly crystalline particles, solid particles.

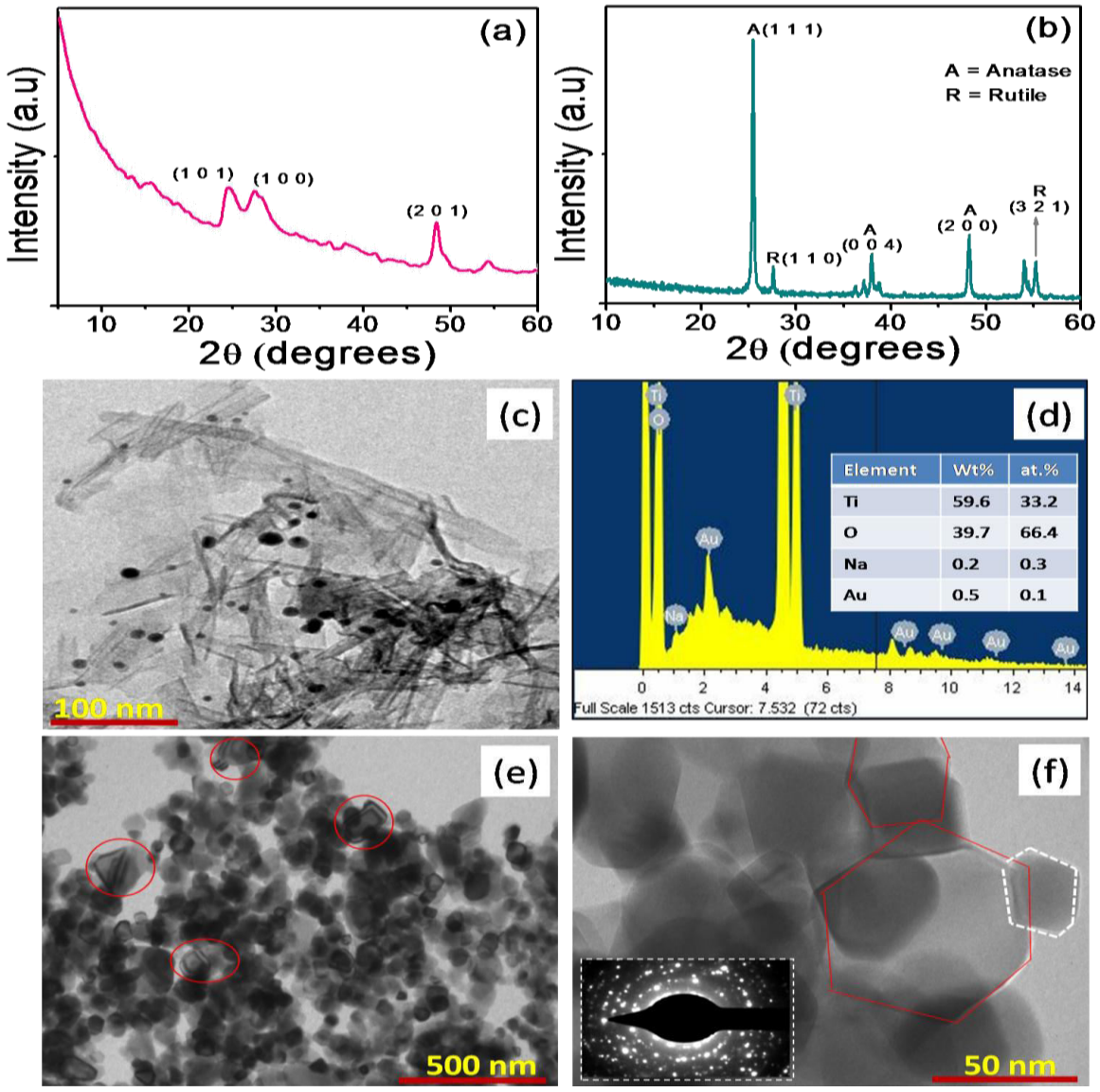

Fig. 6.3 Comparative XRD pattern of 0.5 wt% Au-photodeposited-TNT (a) before and (b) after calcination at 800 °C, (c) TEM image of the former and (d) its corresponding EDS pattern, (e-f) TEM of the later (e-f) and its subsequent SAED pattern (inset).

On the other hand, XRD pattern (Fig. 6.3a) of TNT-Au^{o} (P) correspond to $H_2Ti_3O_7$. H_2O (trititanic acid) [22]. Whereas, the sample TNT-Au^{o}(PS) (Fig. 6.3b) is found to be a mixture of anatase and rutile phase (Table 6.1), as revealed by their reported [1-6] characteristic peaks. The formation of trititanic acid instead of trititanate could be ascribed to the exchange of Na^{+} ions by the photoproduced H^{+} ions, during photodeposition of Au. The H^{+} ions could be easily replaced by Na^{+} ions due to (i) weaker vander-walls forces of attraction between Na^{+} with $Ti_3O_7^{-2}$ layers, (ii) longer bond length of Na-O (2 Å) in $Na_2Ti_3O_7.H_2O$ than H-O (1 Å) in $H_2Ti_3O_7.H_2O$, and (iii) lower elution strength of the Na^{+} ions than H^{+} ions favoring their exchange. However, small deviations has been found in lattice parameters for TNT-Au^{o}(PS) having anatase (ICDS card number: 00-001-0562) and rutile (ICDS card number: 00-01-1292) phases (Table 6.1) in comparison to their standard values. This is believed to be, due to incorporation of Au^{+3} ions in-between octahedral layers of TiO_6 in TNT that got deposited during UV- illumination resulting a strain into the crystal structure (Table 6.1) and altering the lattice parameters.

The TEM image (Fig. 6.3c) of TNT-Au^{0}(P) shows the deposition of Au-nanoparticles particles of size 10-15 nm onto TNT, while the EDS pattern (Fig. 6.3d) of the same confirm the presence of Au (0.5 wt%) in the sample. The sample TNT-Au^{o}(PS) found to be composed of fragmented nanocrystals of size 50-60 nm (Fig. 6.3e), with more number of boat type nanoparticles (circled in Fig. 6.3e), than that found for TNT-Au^{+3}(IS). Moreover, its obtained SAED pattern clearly show the well defined spotted circular rings (inset Fig. 6.3f), indicating TNT-Au^{o}(PS) sample to be crystalline and is consistent with its XRD pattern. The S_{BET} for TNT-Au^{o}(P) (156 m^2g^{-1}) was found to be less (~ 1.2 times) than TNT (176 m^2g^{-1}) and is in accordance with our previous report [6], showing decrease in S_{BET} after photodeposition of Ag and Cu onto TNR, P25 and TNT. However, S_{BET} = 39 m^2g^{-1} for TNT-Au^{o}(PS) was higher than that of TNT-Au^{+3}(IS) that could be rationalized due to its small particle size of former than later, reflected through their respective TEM images.

The XRD pattern (Fig. 6.4b) of TNT-NP(MS) suggests it to be a mixture of $Na_2Ti_3O_7.H_2O$, $Na_2Ti_9O_{19}$ and $NaTiO_2$ crystal structures and thw well consistency of ca. lattice parameters to that of reported values (ICSD card no. 01-072-0148 and 01-089-0802) indicate it to be almost strain free (Table 6.1). It might be because due to negligible probability of exchange of Na^{+} ions by AuNP with much larger radius (3-5 nm). The absence of strain in the

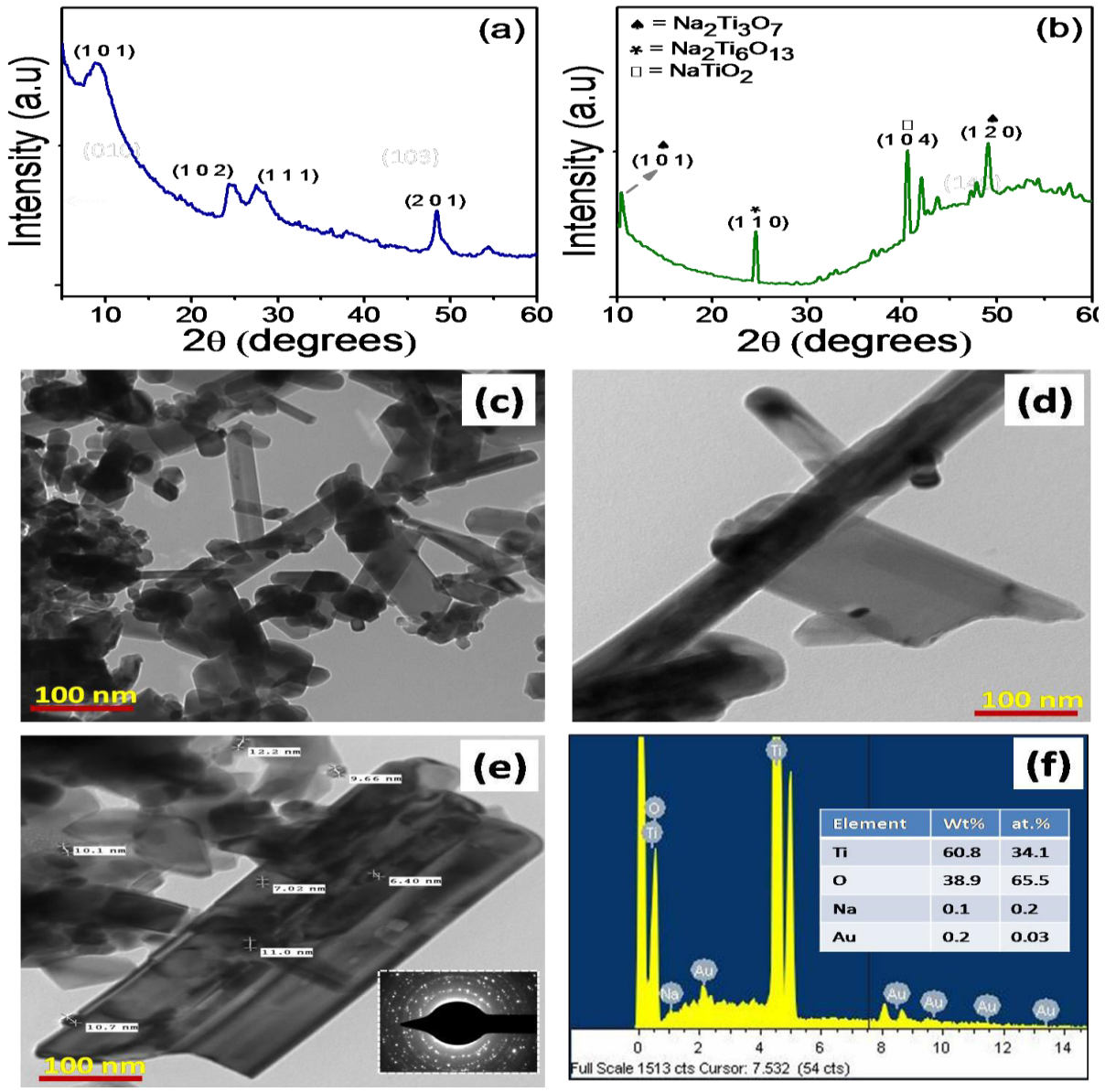

Fig. 6.4 XRD pattern of 0.05 wt% Au-nanosphers-TNT (a) before and (b) after calcination at 800 °C, with TEM images of the later (c-e) with its corresponding SAED pattern (inset) and (f) EDS pattern.

crystal structure of TNT-NP(M) sample also supports the assumption that Na^{+} ions in TNT- Au^{+3}(I) and TNT-Au^{o}(P) samples got exchanged by Au^{+3} ions, resulting in strained crystal structures of TNT-Au^{+3}(IS) and TNT-Au^{o}(PS) (Table 6.1). Moreover, the sample TNT-NP(MS) (Fig. 6.4c-d) was found to be a mixture of nanorods and broken distorted particles, having its SAED pattern *(inset* Fig. 6.4e) in agreement to XRD pattern. The presence of Au in TNT-

NP(MS) was also confirmed by the EDS analysis (Fig. 6.4f). The S_{BET} of TNT-NP(M) and TNT-NP(MS) was found to decrease from 165 to 32 m^2g^{-1}, revealing loading of AuNP cause the growth of smaller fragmented particles possessing higher surface area.

The observed diverseness in the morphology of TNT-Au^{+3}(IS) and TNT-Au^{o}(PS) in comparison to TNT(S) is probably due to induced compression strain (Table 6.1) (C_{strain}) in their crystal structures. This C_{strain} produced in the crystal structure of TNT after the exchange of Na^{+} ions with Au^{+3} ions is believed to inhibit the nucleation growth of TNT during its calcintion at 800 ^{o}C. The formation of smaller particles of size 50-60 nm for TNT-Au^{o}(PS) with more number of boat type particles (insets and circled portion of Fig. 6.3e-f) TNT-Au^{+3}(IS) (65-75 nm in Fig. 6.2c and 6.2d) can be ascribed to higher C_{strain} (around twenty five times) for the former than the later (Table 6.1), this might cause inhibition in the nucleation growth during thermal treatment resulting in small size and boat type particles. This fact is in-turn was further confirmed from the negligible C_{strain} in crystal structure of the TNT-NP(MS) (Table 6.1) transforming most of TNT particles into nanorods. However, some broken particles of TNT-NP(MS) are also formed, because of the Au-loading at the surface of TNT, decreasing the surface energy and interfering with the crystal growth during calcination, though we have not calculated the same. This work is in agreement with the report of Portai et al. [17], showing the formation of smaller nanoparticles (~ 10 nm) after the post thermal treatment of Rh-impregnated TNT particles.

As discussed in chapter-5 that Au-loading alters the life time of excited charge carriers and hence PCA, therefore, τ_{av} for catalysts presented in this chapter were also measured. It was found that τ_{av} for charge carriers of photoirradiated TNT(S) (68 μs) is ~1.8 times more than that of TNT (41 μs) and was further improved (Table 6.1) after Au-loading and calcinations, and was found to be highest for TNT-Au^{o}(PS) (81 μs) catalyst.

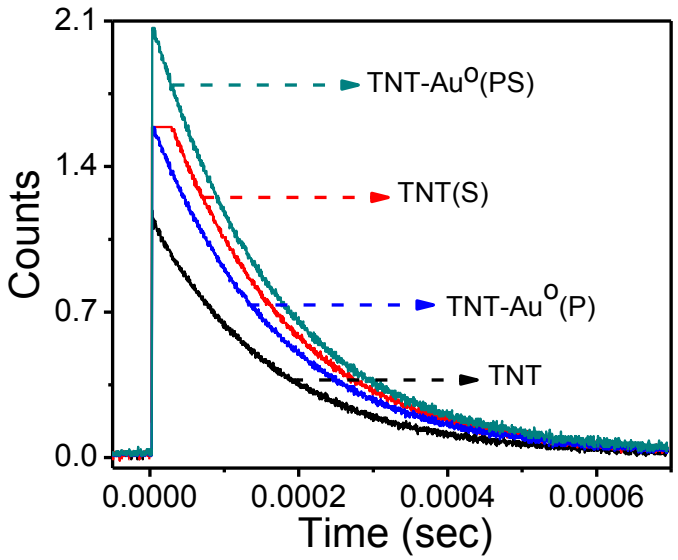

Fig. 6.5 Time resolve luminescence decay of bare and 0.5 wt% Au-photodeposited TNT (before and after calcinations).

This increase in τ_{av} is because of the deposits of Au as co-catalyst on the support acting as a sink for the photogenerated electrons [23] enhancing the life time of charge species (Table 6.1) and is in correlation with the results obtained for Au-loaded TNT(S) (chapter-5, *section 5.3*).

It has been found (Fig. 6.6) that the hollow and porous TNT exhibits highest photocatalytic activity among the bare nanocrystals, whereas Au-loading onto TNT always increased the PCA as evidenced by the ca. rate constants (Table 6.1). The highest PCA of TNT is attributed to its structural parameters as discussed previously (chapter-3, *section 3.3*). However, among various as-prepared bare and Au-loaded catalysts, the sample TNT-Au^{o}(PS) is found to be most photoactive ($k = 8.9\times10^{-3}$ min^{-1}) than the most photoactive P25. Such high PCA is due to the presence of Au along with the photoactive anatase and rutile phases (Table 6.1) resulting into high τ_{av} (81 μs) i.e., increase in the charge separation efficiency and thereby improved photoactivity.

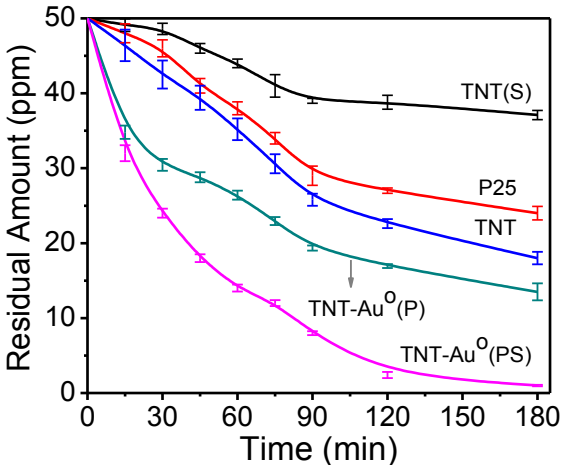

Fig. 6.6 Photocatalytic degradation of imidacloprid with P25 in comparison to bare and various Au-loaded TNT, before and after calcination.

The LC chromatographs (Fig. 6.7) indicate decrease in peak height of the imidacloprid (retention time R_t = 2.05 min) after 180 min of its photooxidation under UV-light irradiation using TNT-Au(PS) with simultaneous appearance of many new peaks at R_t = 1.6, 1.9, 2.3 and 2.5 min. LC-MS analysis confirmed the formation of various intermediate products (Fig. 6.8), and were identified as compound A viz., 1-(6-chloropyridin-3-yl)methyl)imidazolidin-2-imine (R_t=1.6 min), compound B viz., (Z)-N-(1-((6-chloropyridin-3-yl)methyl)-5-hydroxyimidazolidin-2-ylidene) nitramide (R_t = 2.3 min), and the compound C (R_t = 2.5 min) is found to be (Z)-N-(1-((6-chloropyridin-3-yl)methyl)-4-hydroxyimidazolidin-2-ylidene)nitramide. The compound, D and E corresponding to R_t = 1.93 min in the chromatograph were not successfully identified.

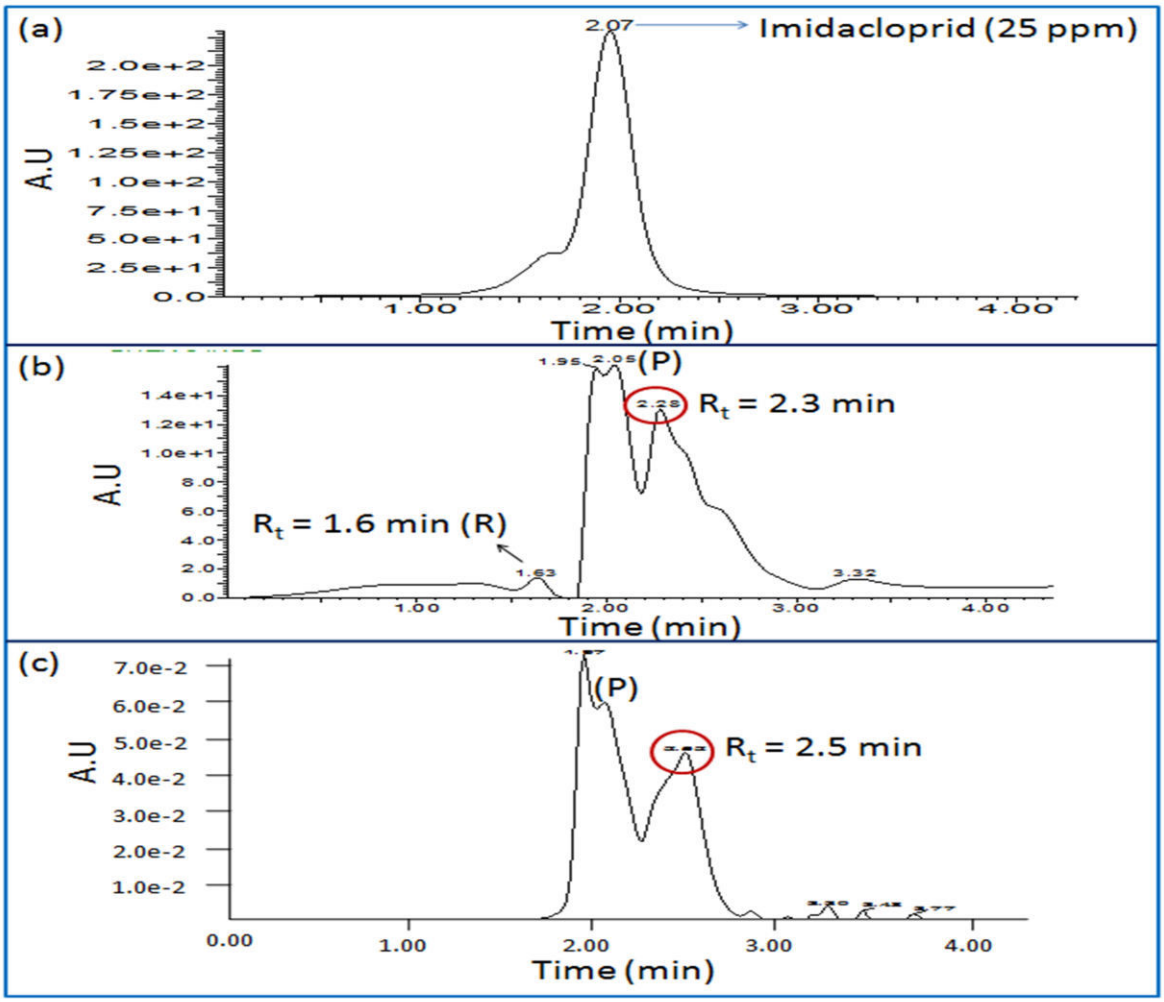

Fig 6.7: LC chromatographs of (a) authentic imidacloprid, and its photooxidation with (b) TNT(S) and (c) TNT-Au^{+3}(I), after 180 min of UV-irradiation.

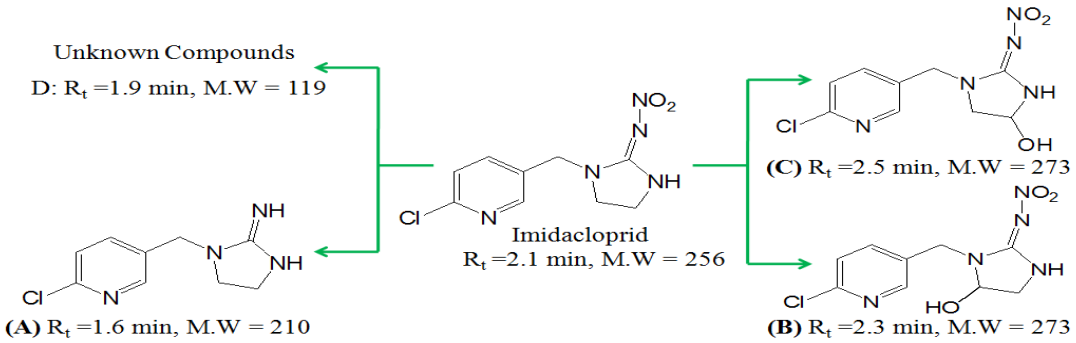

Fig. 6.8 Schematic representation for structural formulae corresponding to different retention time (R_t) and molecular weights (M.wt) of some identified/unidentified compounds.

The gradual photocatalytic detoxification of imidacloprid resulted in its mineralization to CO_2 and inorganic ions such as nitrate, chloride and nitrate ions as described in *section 4.3 of* chapter-4. As can be seen in Fig. 6.9, CO_2 evolution increases with time of UV-light irradiation, and was highest (25.7 ppm = 3.1 µmol) in case of TNT-Au^0(PS) photocatalyst, showing 34.4 % of IMI's mineralization from 97.2% (48.6 ppm) of its photodegradation, In contrast to this, only 15.3% (11.5 ppm =1.38 µmol of CO_2) of mineralization was found from 31.5 ppm (0.71 µmol) of IMI by bare TNT. This indicates incomplete mineralization of IMI and is ascribed to the formation of heteroatom containing intermediates (discussed in chapter-4, *section-4.3*).

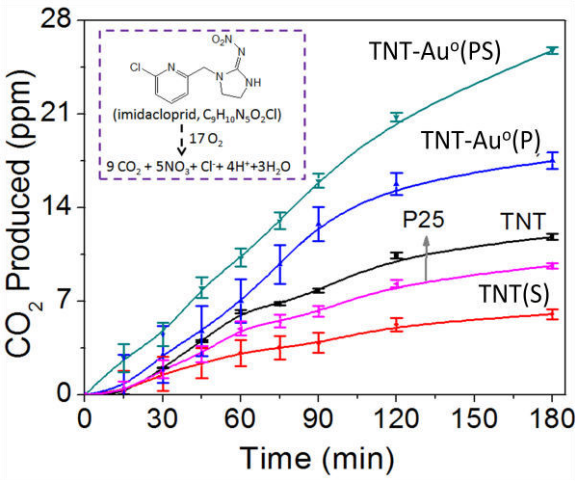

Fig. 6.9 Amount of CO_2 produced by photodegradation of imidacloprid at various time intervals with P25 in-comparison to bare and various Au-loaded TNT (before and after calcination), inset; balanced chemical equation for complete mineralization of imidacloprid.

6.4 Conclusions:

It is demonstrated in this chapter that presence of Au interferes with the growth of TNT(S) during calcination of TNT at 800 ^{o}C and led to the formation of other morphologies and crystal structures. Among a variety of as-prepared catalysts, TNT-Au^o(PS) having anatase and rutile phases exhibited superior PCA for the mineralization of IMI to CO_2 than the most photoactive P25, owing to higher lifetime of charge carriers.

6.5 References:

[1] C.K. Lee, C.C. Wang, M.D. Lyu, L.C. Juang, S.S. Liu and S.H. Hung, *J. Colloid Interface Sci.,* 316 (2007) 562-569.

[2] J. Yu, H. Yu, B. Chenga and C. Trapalis, *J. Mol. Catal. A Chem.,* 249 (2006)135-142.

[3] M. Qamar, C.R. Yoon, H.J. Oh, N.H. Lee, K. Park, D.H. Kim, K.S. Lee, W.J. Lee and S.J. Kim, *Catal. Today,* 131 (2008) 3-14.

[4] M. Qamar, C.R. Yoon, H. Jho, D.H. Kim, J.H. Jho, K.S. Lee, W.J. Lee, H.G. Lee and S.J.

Kim, *Nanotechnology,* 17 (2006) 5922-5929.

[5] E. Morgado Jr., M.A.S. de-Abreu, O.R.C. Pravia, B.A. Marinkovic, P.M. Jardim, F.C. Rizzo and A.S. Araujo, *Solid State Sci.,* 8 (2006) 888-900.

[6] I.S. Grover, S. Singh and B. Pal, *Appl. Surf. Sci.,* 280 (2013) 366-372.

[7] V. Stengl, S. Bakardjieva, J. Subrt, E. Vecernıkova, L. Szatmary, M. Klementova and V. Balek, *Appl. Catal. B Environ.,* 63 (2005) 20-30.

[8] H. Song, H. Jiang, T. Liu, X. Liu and G. Meng, *Mater. Res. Bull.,* 42 (2007) 334-344.

[9] X. Ding, X.G. Xu, Q. Chen and L.M. Peng, *Nanotechnology,* 17 (2006) 5423-5427.

[10] X. Si, F. Li, L. Sun, F. Xu, S. Liu, J. Zhang, M. Zhu, L.Z. Ouyang, D. Sun and Y.L. Liu, *J. Phys. Chem. C,* 115 (2011) 9780-9786.

[11] M.I. litter, *Appl. Catal. B Environ.,* 23 (1999) 89-114.

[12] J.Y. Tsai, J.H. Chao and C.H. Lin, *J. Mol. Catal. A Chem.,* 298 (2009)115-124.

[13] D.V. Bavykina, A.A. Lapkinb, P.K. Plucinskib, L.T. Murcianob, J.M. Friedricha and F.C. Walsh, *Top. Catal.,* 39 (2006) 3-4.

[14] J.S. Jang, S. H. Choi, D.H. Kim, J.W. Jang, K.S. Lee and J.S. Lee, *J. Phys. Chem.C,* 113 (2009) 8990-8996.

[15] S. Mandl, G. Thorwarth, B. Stritzker and B. Rauschenbach, *Surf. Coat. Technol.,* 200 (2005) 589-593.

[16] M.S.J. Marshall and M.R. Castell, *Phys. Rev. Lett.,* 160 (2009) 146102-146016.

[17] G. Potari, D. Madarasz, L. Nagy, B. Laszlo, A. Sapi, A. Oszko, A. Kukovecz, A. Erdohelyi, Z. Konya, and J. Kiss, *Langmuir,* 29 (2013) 3061-3072.

[18] J. Tang, X. Huang, X. Huang, L. Xiang and Q. Wang, *Environ. Earth Sci.,* 66 (2012) 441-445.

[19] V. Kitsiou, N. Filippidis, D. Mantzavinos and I. Poulios, *Appl. Catal. B Environ.,* 86 (2009) 27-35.

[20] W.A. Donald, M.G. Leeming and R.A.J. O-Hair, *Int. J. Mass Spectrom.,* 316 (2012) 91-99.

[21] M.L.D. Arciprete, L.S. Juanes, A.A. Sanz, R. Vicente, A.M. Amat, J.P. Furlong, D.O. Martire and M.C. Gonzalez, *Photochem. Photobiol. Sci.,* 8 (2009) 1016-1023.

[22] J.Z. Jin, X. Wang, W. Li, J. Zhang, S. Zhang, X. Guo and Z. Zhang, *Dalton Trans.,* (2003) 3898-3901.

[23] R. Kaur and B. Pal, *J. Mol. Catal. A Chem.,* 355 (2012) 39-43.

7. High temperature synthesis of anatase TiO_2 and its improved photocatalytic activity for degradation of Methyl Parathion

7.1 Introduction

Anatase TiO_2 (TiO_2(A)) crystals because of their better surface properties, adsorptive affinity and greater rate of hole trapping efficiency have proven [1–8] to exhibit better PCA than the well-known TiO_2 rutile (TiO_2(R)) phase. Moreover, because of a relative dissimilarity between the geometry of TiO_2(A) (tetragonal) and TiO_2(R) (distorted tetragonal) that originates from different arrangement of TiO_6 octahedral units, TiO_2(A) is reported to deliver higher PCA [1,2,8] than TiO_2(R) because of its indirect band gap character and presence of more hydroxylated groups on its surface. TiO_2(R) phase shows its importance in case of P25 powder, a mixture of 70% anatase and 30% rutile, where it acts as an electron sink; hence, showing superior PCA [1,2,9] than its pure phase alone. The use of P25 as a self-cleaning agent in building materials require a high temperature treatment [7,10] during preparation of ceramic materials and for proper adherence to the TiO_2 (mixed/coated) surface. This causes a TiO_2(A)-to-TiO_2(R) phase transformation with a notable decrease in PCA because of formation of less-photoactive TiO_2(R) phase [1–10] at > 600–700 ^oC. Therefore, highly crystalline TiO_2(A) is required without deterioration of photoactivity at high temperatures, high crystallinity leads to fewer surface defects [7–10] acting as recombination sites for charge carriers and consequently enhances the PCA.

Various attempts [11-17] have been made to resist the TiO_2(A)-to-TiO_2(R) conversion at > 600 ^oC, and this was achieved through surface modification with metal oxides (such as Al_2O_3, NiO, and ZnO) causing this phase transformation. However, the formation of secondary impure phases (such as Al_2TiO_5, and $NiTiO_3$) resulted in a decrease of photoactivity [16,17] which remains a major concern for this technique. Although reports [1,2] exist for the preparation of pure anatase TiO_2 at ambient conditions through a variety of routes, it still showed only moderate activity because of its poor crystallinity and amorphous nature. Hence, for the best efficiency, a pure and stable TiO_2(A) phase at higher temperature (> 600 ^oC) without reduction in its PCA is highly desirable. The present study reveals that as-prepared TiO_2 nanorods retains the anatase crystal phase (~100%) by calcination at elevated temperatures (800–900 ^oC) and showed ~2-11 times better PCA than conventional P25 calcined at the same temperature when used for

photooxidation of MP, a pesticide used [18,19] widely in agricultural fields. Moreover, the effect of Au deposition on the complete decomposition of MP by this crystalline TiO_2(A) phase during UV-light irradiation is discussed in terms of CO_2 evolution and intermediate photoproducts formation by GC–MS analysis.

7.2 Experimental section

7.2.1 Synthesis of bare and Au loaded TiO_2 nanoparticles, characterization and photocatalytic activity: Thermally stable bare anatase TiO_2 nanoparticles were prepared by method reported in *section-2.2.5* of chapter-2. Au-loading was done by photodeposition method (*section-2.4.1,* chapter-2). The catalysts were characterized by XRD (*section-2.5.1*), TEM (*section-2.5.3*), Diffuse Reflectance Spectrophotometer (*section-2.5.6*), Raman Spectroscopy (*section-2.5.8*) and S_{BET} (*section-2.5.10*) and the techniques discussed in chapter-2. The PCA of bare and Au-loaded TNP was assessed by degrading MP (*section-2.6.1*) under UV-light, and the reaction samples were analyzed by UV-visible spectrophotometer (*section-2.6.3*), GC (*section-2.6.5*) and GC-MS (*section-2.6.6*) as described in chapter-2.

7.3 Results and discussion

The XRD analysis (Fig. 7.1a) of the samples (C-2 to C-9) clearly showed the existence of TiO_2(A) as a major phase, as revealed by its characteristic peaks (ICSD card no.: 00-002-0387). With a gradual increase in calcination temperature (200–900 ^oC), there is a noticeable increase in intensity, sharpness and a decrease in broadness for the (101) peak at $2\theta = 25.3^o$ of TiO_2(A). In contrast, calcination of P25 at 800 ^oC resulted in complete transformation of the TiO_2(A) to the TiO_2(R) phase, as evidenced (Fig. 7.2) by its characteristic (110) peak at $2\theta = 27.5^o$ (ICDS:card no.: 00-001-1292). It is also seen that some small peaks (at $2\theta = 27.6^o$) for a brookite phase (ICDS: card no.: 00-002-0514) were also present in C-2 to C-7 samples, and a new small peak for the (110) plane of TiO_2(R) appears for C-9 sample (Fig. 7.1b).

The co-existence of a small amount of brookite phase (1.8–0.18%) ca. similar to that of reported method (*section-2.5.1*, chapter-2) for TiO_2(A) (Table 7.1) could be the cause [7,21,22] of its thermal stability, as the presence of brookite phase [21] obtained by hydrolysis of tertrabutyl titanate in the presence of surfactant imparted thermal stability (> 700 ^oC) to TiO_2(A). The mean crystalline sizes of TiO_2(A) calculated using the Scherrer equation [1] increases in the range of 16–40 nm with increase in calcination temperatures from 200–900 ^oC (Table 7.1), indicating its gradual crystal growth [1,2,23] during thermal treatment. This is in

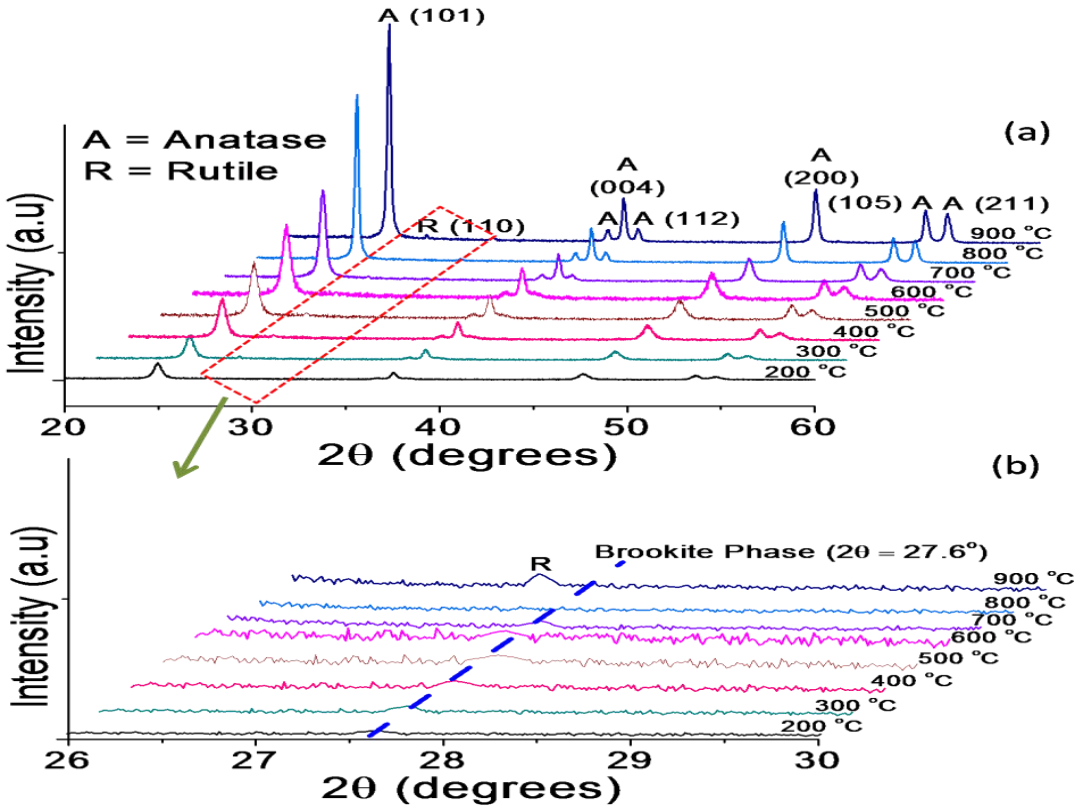

Fig. 7.1 XRD pattern for anatase TiO_2 (a) calcined at different temperatures and (b) their magnified (2θ = 26-30°) view.

good agreement with the recent report of Kang et al. [10] showing TiO_2(A) having crystallites > 14 nm was retained (> 96%) even after calcination at 900 °C. However, some reports [24,25] have also indicated TiO_2(A) size < 14 nm to be thermodynamically more stable than TiO_2(R) and resist towards the conventional anatase-to-rutile transformation.

This crystal phase transformation was further confirmed by Raman spectra of four samples (C-2, C-5, C-8 and C-9; Fig. 7.3). Three less-intense and broad peaks

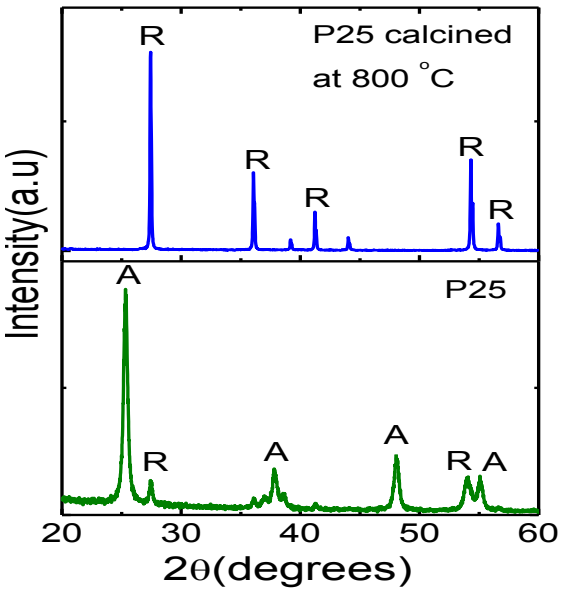

Fig. 7.2 Comparative XRD patterns; where A = anatase and R = Rutile.

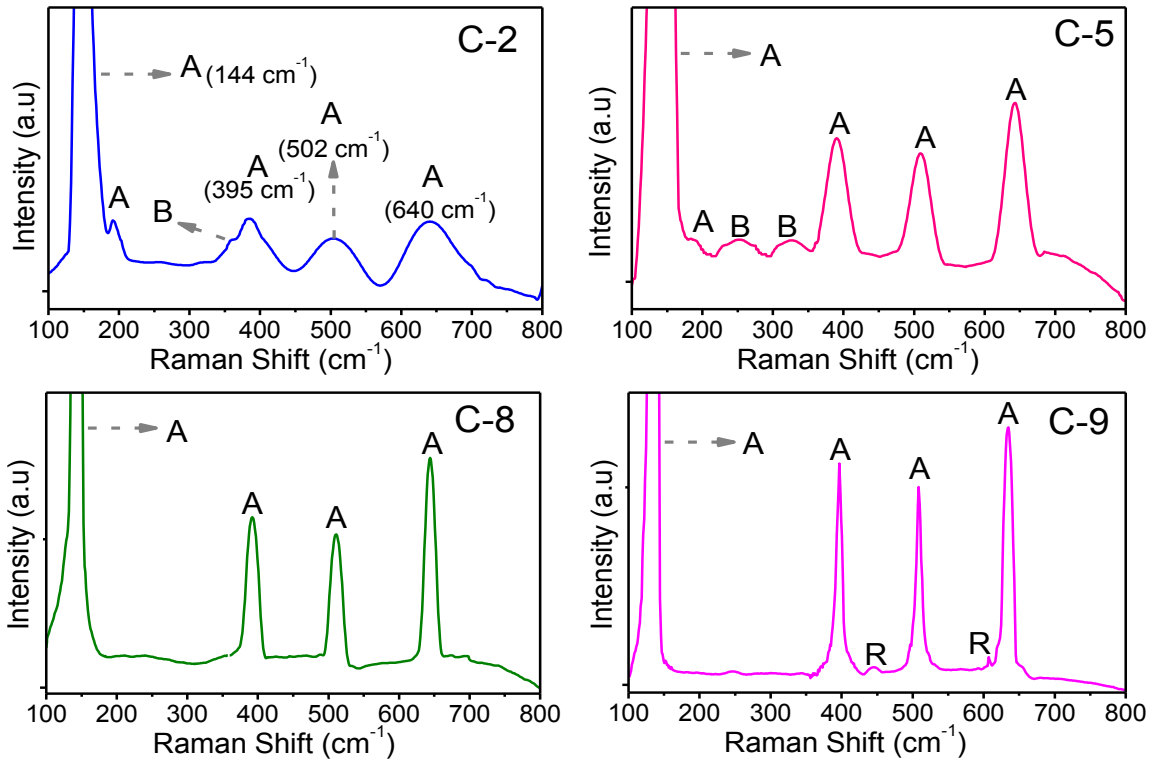

Fig. 7.3 Raman spectra of various calcined TiO_2 samples where A = Anatase, B = Brookite and R = Rutile phase.

at 247, 318 and 366 cm^{-1} for C-2 and C-5 (Fig. 7.3) samples corresponding [21] to A1g, B1g and B2g Raman vibration modes were due to the formation of small amount (1.8–0.18%, Table 7.1) of brookite phase. However, the sample C-8 (Fig. 7.3) displayed only four intense and sharp peaks for Raman active vibration modes at 144, 395, 513 and 639 cm^{-1}, characteristic of TiO_2(A) [17,21]. Interestingly, two very small peaks at 447 and 610 cm^{-1} for C-9 catalyst, due to growth of a negligible amount (0.9%) of rutile phase were observed, along with four intense peaks (namely at 144, 395, 513 and 639 cm^{-1}) for TiO_2(A), as seen in Fig.7.3d. This clearly confirms the retention [26] of the crystalline anatase phase of TiO_2 at > 800 ^oC and is in agreement with the XRD study.

The morphological study of C-2 (Fig. 7.4a) revealed rice-like nanorods with a length (L) = 81-134 nm and diameter (D) = 8-13 nm (presented in chapter-3, s*ection 3.3*). With a gradual increment in calcination temperatures from 200 to 500 ^oC and at 800 ^oC, fragmentation causes alteration in morphology, from nanorods to a mixture of irregularly shaped particles (60-70 nm),

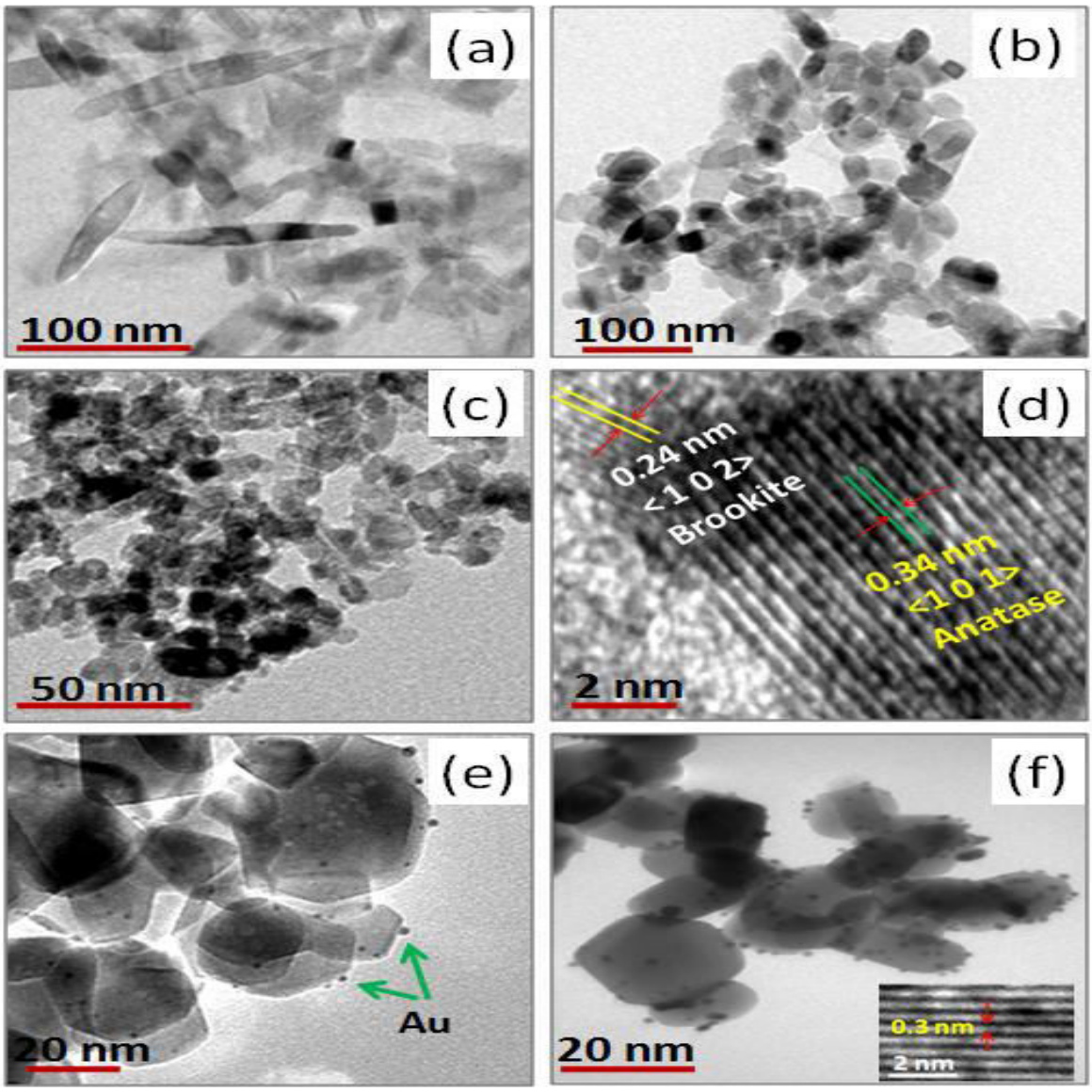

Fig. 7.4 HR-TEM images for calcined TiO2 samples (a) C-2, (b and c) C-5, (d) lattice fringes of C-5 and (e and f) Au-C-8 with its lattice fringe (inset).

a few distorted rod-like shapes (L = 60-110 nm and D = 7-12 nm) (Fig.7.4b–c) and nanopolygons of size ~95–115 nm, (Fig. 7.4e-f).

Although there was no significant change in the morphology of P25 and P25(R), there was an increase in size from 30–50 nm to 70–80 nm, respectively (Fig. 7.5). Due to the thermal fragmentation of C-5 and C-8 samples, a few new particles with fresh, smooth surfaces, having fewer surface defects and more surface exposed atoms were formed; thus, they may show [1,2] better photocatalytic performance. This shape transformation is accompanied by decrease

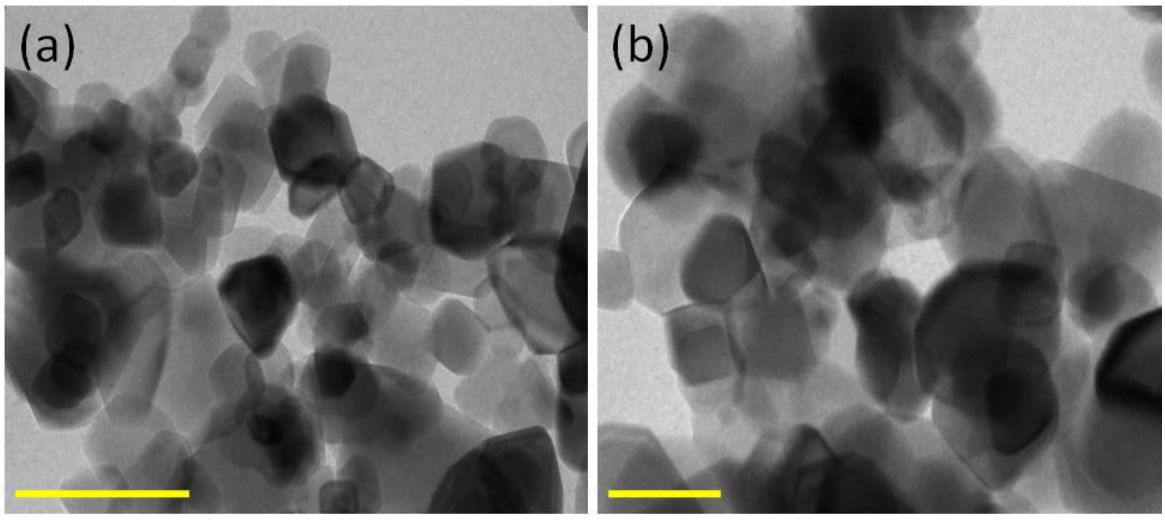

Fig. 7.5 TEM images for P25 (a) before and (b) after calcinations at 800 ^{o}C, scale bar is 100 nm

(Table 7.1) in the S_{BET} from 79 m^2 g^{-1} to 57 m^2 g^{-1} and then to 31m^2 g^{-1} for C-2, C-5 and C-8 samples, respectively. The increased particle size and decreased S_{BET}, attributed to their crystal growth during calcinations, is in good agreement with reported [1,2,23] results. The presence of characteristic lattice fringes at 0.24 nm and 0.34 nm, corresponding to the brookite and TiO_2(A) phase (Fig. 7.3d), confirms the existence of both crystal phases in the C-5 catalyst. However, for C-8, a characteristic lattice fringe at 0.3 nm belonging to TiO_2(A) [1,2,7,20] indicates the formation of a pure anatase phase, as shown by XRD and Raman spectras studies. The TEM images of Au-C-8 (Fig.7.3e-f) showed many Au-deposited TiO_2 nanoparticles having a uniform deposition of Au nanoparticles (with narrow size distribution of 4-6 nm) over its surface. During the preparation of such stable and pure anatase TiO_2, no surfactant or other chemical reagent (except NaOH and HNO_3) was added [16,17] which could hamper the PCA, hence, the present technique could be useful for optimizing the photoactivity in many applications.

The plots of $(\alpha h\nu$ or $\alpha E)^{1/2}$ versus band gap energy (E_g) for TiO_2 in Fig. 7.6 revealed that E_g for P25 (3.1 eV) and C-2 (3.21 eV) are consistent with the reported values [1,20] which are also described in chapter-3 (*section 3.3*) and that upon its calcination at 900 ^{o}C, E_g was reduced by 0.16 eV. As the particle and crystallite size of as-prepared samples are found to increase

gradually with rise in calcination temperatures, the decrease in E_g values [1,20,21] is probably due to a quantum size effect.

The time course of photocatalytic oxidation for MP by various titania catalysts calcined at different temperatures relative to bare P25 and P25(R) is shown in Fig.7.7a. It can be seen that anatase–rutile mixed phases of P25 exhibited higher activity (inset, Fig. 7.7b) than rutile TiO_2 (showing the least activity among the studied photocatalysts), and 1 wt% Au loading onto P25 and C-8 catalysts further improved the MP degradation. The photooxidation of MP followed a linear relationship with irradiation time and decayed exponentially with increased calcination temperatures of C-2 to C-9, indicating pseudo-first order kinetics.

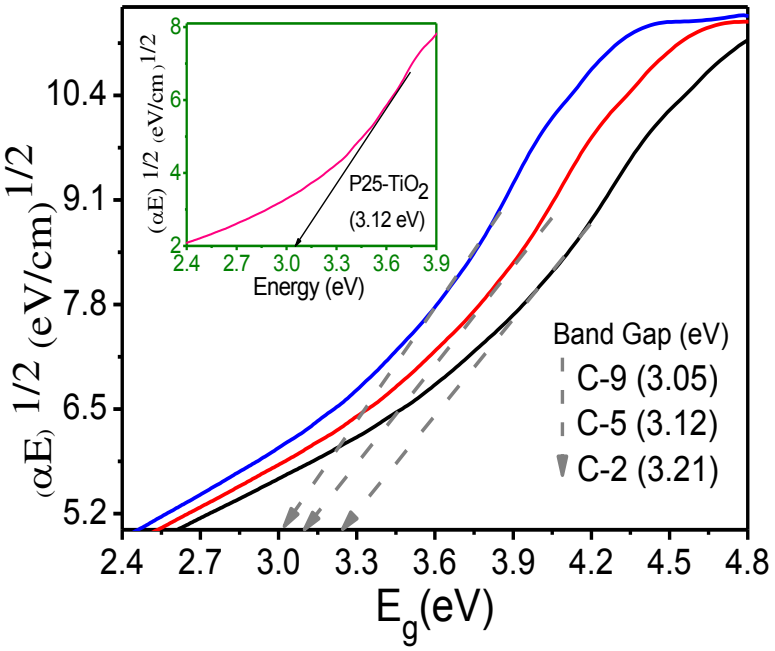

Fig. 7.6 Band gap energy of various TiO_2 samples as compared to (inset) P25-TiO_2 catalyst.

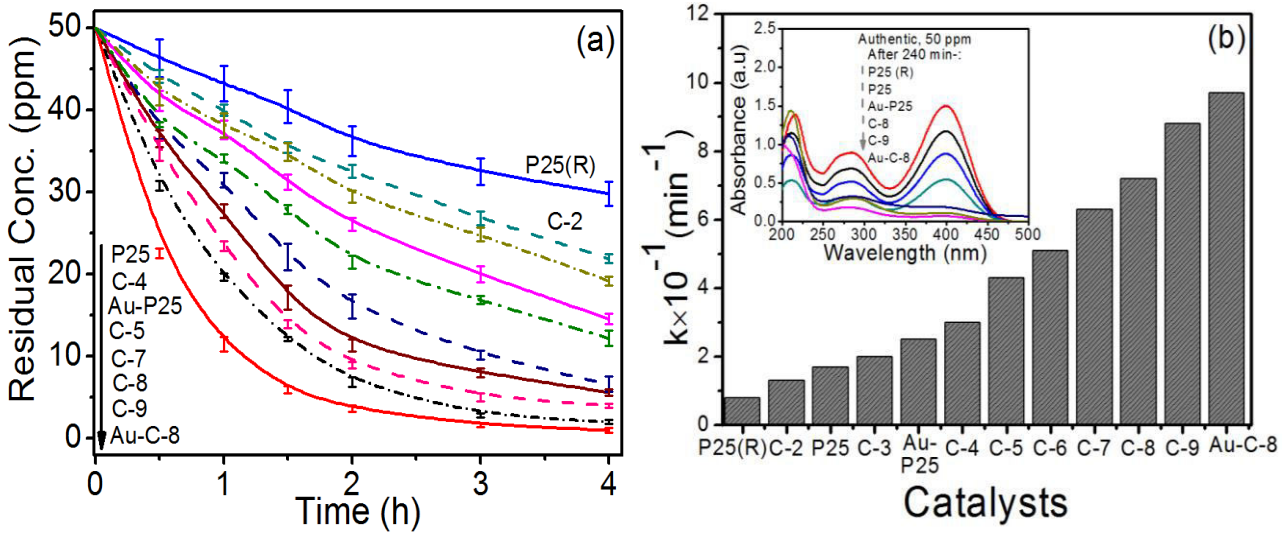

Fig. 7.7 (a) Time course of methyl parathion photooxidation by different calcined and 1wt% Au-deposited TiO_2 catalysts, and (b) their apparent rate constants; *inset*: absorption spectra for photooxidation of methyl parathion).

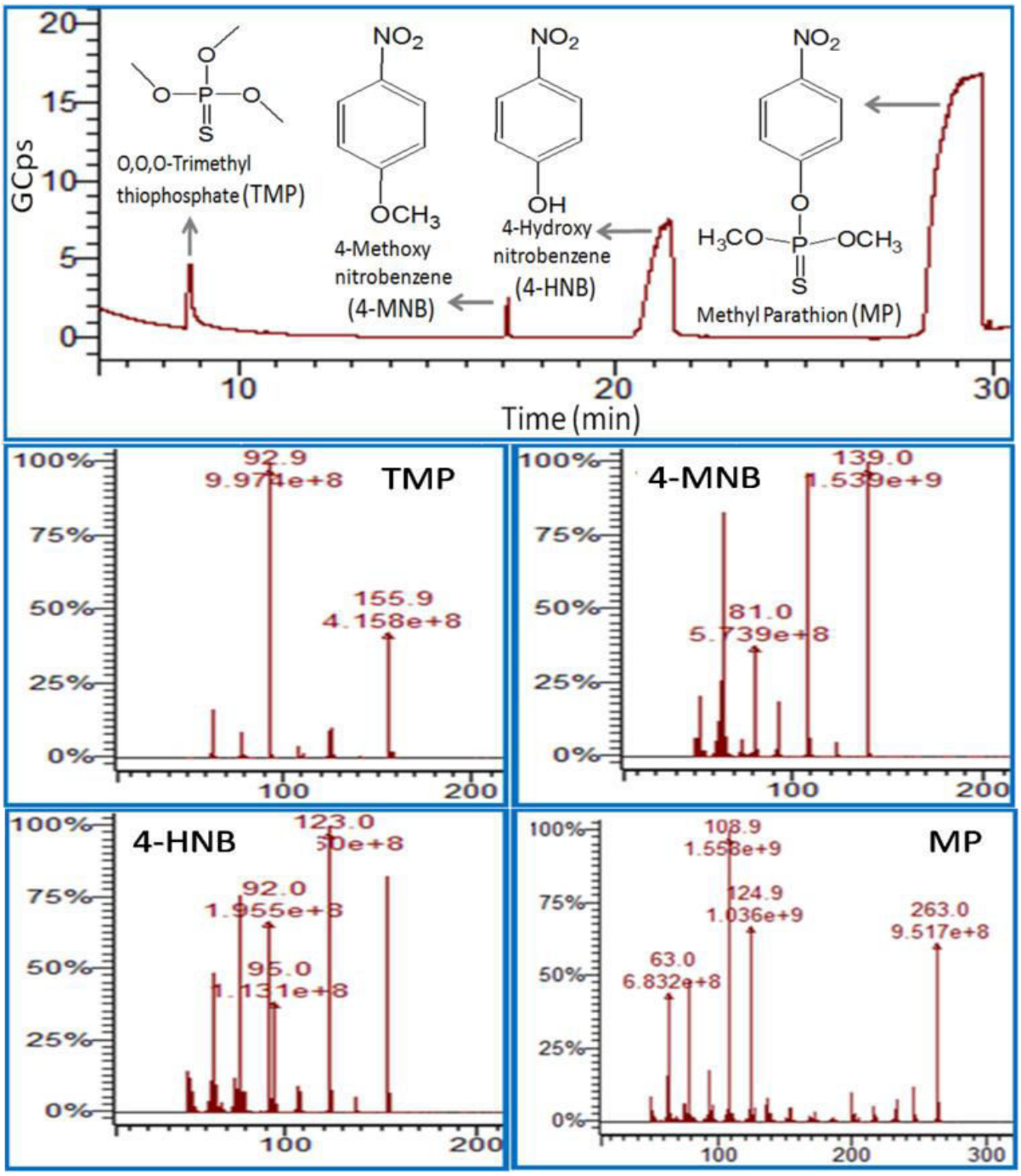

Fig. 7.8 (a) Time course of methyl parathion photooxidation by different calcined and 1wt% Au-deposited TiO_2 catalysts, and (b) their apparent rate constants; *inset*: absorption spectra for photooxidation of methyl parathion)

The apparent rate constant (k) obtained from time course graph gradually increased from 1.3×10^{-1} min^{-1} for C-2 to 8.8×10^{-1} min^{-1} for C-9 and is the highest (9.7×10^{-1} min^{-1}) for the Au-C-8 catalyst. By comparison, the MP degradation efficiency exhibited by P25 ($k = 2.6 \times 10^{-1}$

min^{-1}) is greatly reduced for P25(R) ($k = 0.78 \times 10^{-1}$ min^{-1}), revealing higher (2–11 times) PCA of C-2 to C-9 catalysts as compared with the most active P25 catalyst.

After 120 min of UV irradiation, although Au-C-8 catalyst displayed complete degradation of MP (47.1 ± 0.4 ppm), incomplete mineralization occurs because of the formation of many smaller intermediate photoproducts, as revealed by GC-MS analysis (Fig.7.8), which showed the formation of 4-hydroxynitrobenzene (m/z = 140), 4-methoxynitrobezene (m/z = 139) and O,O,O-trimethyl thiophosphate (m/z = 155) intermediates. This indicated that a longer irradiation time is needed to further decompose these intermediate products into smaller molecules so that products can be completely mineralized to CO_2 and H_2O.

The time course of CO_2 formation (Fig. 7.9) during photooxidation of MP by various titania catalysts showed a steady increase in CO_2 concentration with light irradiation. We noticed that the trends of CO_2 formation exhibited by different catalysts are similar to the MP photooxidation (Fig. 7.7), in which superior catalytic activity of the calcined titania (C-3 to C-9) samples was observed compared with bare P25 and P25(R) catalysts. The highest amount (178 ppm) of CO_2 formed corresponds to ~ 25% by the Au-C-8 catalyst, followed by C-9 catalyst (156.2 ppm), indicating a 22% mineralization of MP during 4 h UV irradiation.

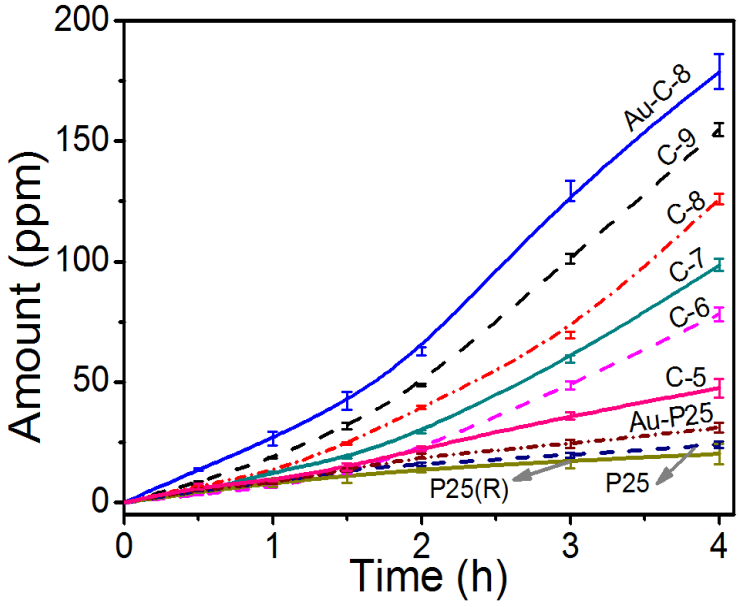

Fig. 7.9 CO_2 formation rate during photooxidation of methyl parathion by different TiO_2 catalysts.

The presence of crystalline TiO_2(A) phase in calcined catalysts is believed to be the cause for their higher PCA [1–10] as compared with pure rutile TiO_2, in which existence of the dominantly (110) planes are reported to act as better reduction sites than oxidation sites [5]. It was reported by Yu et al. [26] that an increase in crystallinity of TiO_2(A) by calcining at > 100 ^oC causes its enhanced PCA as compared with P25. The presence of interfacial contact between crystalline TiO_2(A) and brookite phases in C-2 to C-9 is expected to facilitate the migration

[21,27] of photoexcited holes from the anatase to the brookite phase due to higher valance band edge of the former (3.1 eV vs NHE) than the latter (3.0 eV vs NHE), resulting in their higher efficiency for MP oxidation. However, in case of P25, transfer of only electrons from TiO_2(A) to TiO_2(R) phase occurs, resulting in less suppression of charge recombination process than at the anatase-brookite TiO_2 interface [21] hence, lower photoactivity was shown by P25 as compared with the as-prepared calcined titania samples.

A detrimental influence [1,2,16,24] from increased crystallite size (16–40 nm) and decreased S_{BET} (from 79 to 31 $m^2\ g^{-1}$) on the photocatalytic activity of calcined catalysts was not observed. As a result, the enhanced photoactivity of C-2 to C-9 catalysts can be ascribed to the increasing crystallinity that generally reduces the defect sites for relaxation of photoproduced e^-/h^+ pairs [1,2,11-17] in TiO_2(A).

This photoactivity could also be correlated with the rate constant per unit surface area (k_1) in Table 7.1, where $k_1 = 0.283 \times 10^{-1}\ min^{-1}m^{-2}g$ for C-9 is higher than $k_1 = 0.016 \times 10^{-1}\ min^{-1}m^{-2}g$ for C-2, $k_1 = 0.04 \times 10^{-1}\ min^{-1}m^{-2}g$ for P25 and $k_1 = 0.013 \times 10^{-1}\ min^{-1}\ m^{-2}g$ for P25(R) catalysts. Thus, despite the decrease in surface area with increased calcination temperatures, the photoactivity per unit surface area is increased relative to that of the P25 catalyst. Therefore, it can be emphasized that improvement in crystallinity [7] diminishes the recombination of excited charge carriers, resulting in enhanced photoactivity. Moreover, there is a notable and significant increase in intensity of (101) planes with increasing calcination temperatures. This causes more (101) surface faces that serve as adsorption sites of electron-scavenging O_2 molecules, which facilitates the formation of more oxidative superoxide radicals [9] and are responsible for the highest activity of the C-9 catalyst. The Au-loading notably improves the photocatalytic activity owing to the rapid charge transfer, and the Fermi energy level equilibrium at the Au–TiO_2 interface suppressing [1,2,23,28] the charge recombination process, thereby enhancing the PCA.

7.4 Conclusions

It is conveyed through this chapter that hydrothermally prepared TiO_2 nanorods retain its anatse phase after calcination at > 800 ^oC in comaparison to P25, which is completely transformed to rutile phase, and exhibited enhanced decay constant than P25 for decomposition of MP to CO_2.

7.5 References

[1] X. Chen and S.S. Mao, *Chem. Rev.,* 107 (2007) 2891-2959.

[2] A. Kudo and Y. Miseki, *Chem. Soc. Rev.,* 38 (2009) 253-278.

[3] J. Yan, G. Wu, N. Guan, L. Li, Z. Lib and X. Cao, *Phys. Chem. Chem. Phys.,* 15 (2013) 10978-10988.

[4] J.C. Yu, J. Lin, D. Lo and S.K. Lam, *Langmuir,* 16 (2000) 7304-7308.

[5] N. Wu1, J. Wang, D.N. Tafen, H. Wang, J. G. Zheng, J.P. Lewis, X. Liu, S.S. Leonard and A. Manivannan, *J. Am. Chem. Soc.,* 132 (2010) 6679-6685.

[6] G.S. Herman, Z. Dohnalek, N. Ruzycki and U. Diebold, *J. Phys. Chem.* B, 107 (2003) 2788-2795.

[7] W. Li, Y. Bai, C. Liu, Z. Yang, X. Feng, X. Lu, N.K.V.D. Laak and K.Y. Chan, *Environ. Sci. Technol.,* 43 (2009) 5423-5428.

[8] T. Luttrell, S. Halpegamage, J. Tao, A. Kramer, E. Sutter and M. Batzill, *Sci. Rep.,* 4 (2014) 4043-4050.

[9] D.C. Hurum, A.G. Agrios, K.A. Gray, T. Rajh and M.C. Thurnauer, *J. Phys. Chem. B,* 107 (2003) 4545-4549.

[10] C. Kang, L. Jing, T. Guo, H. Cui, J. Zhou and H. Fu, *J. Phys. Chem.* C, 113(2009)1006-1013.

[11] R. Arroyo, G. Cordoba, J. Padilla and V. H. Lara, *Mater. Lett.,* 54 (2002) 397- 402.

[12] S. Sabale, A. Bandgar, H. Wang, K. Gurav, J.H. Kim and S.H. Pawar, *Met.Mater. Int.,* 19 (2013) 483-488.

[13] H. Zhang and J.F. Banfield, *J. Phys. Chem. B,* 104 (2000) 3481-3487.

[14] M.S.P. Francisco and V.R. Mastelaro, *Chem. Mater.,* 14 (2002) 2514-2518.

[15] D.J. Reidy, J.D. Holmes, C. Nagle and M.A. Morris, *J. Mater. Chem.* 15 (2005) 3494-3500.

[16] S.C. Pillai, P. Periyat, R. George, D.E. McCormack, M.K. Seery, H. Hayden, J. Colreavy, D. Corr and S.J. Hinder, *J. Phys. Chem. C,* 111 (2007) 1605-1611.

[17] C. Kang, L. Jing, T. Guo, H. Cui, J. Zhou and H. Fu, *J. Phys. Chem. C*, 113 (2009) 1006-1013.

[18] E. Moctezumaa, E. Leyvaa, G. Palestinoa, H. de-Lasa, *J. Photochem. Photobiol. A Chem.,* 186 (2007) 71-84.

[19] I.K. Konstantinou, T.M. Sakellarides, V.A. Akkas and T.A. Albanis, *Environ. Sci. Technol.,* 35 (2001) 398-405.

[20] I. S. Grover, S. Singh and B. Pal, *Appl. Surf. Sci.,* 280 (2013) 366-372.

[21] G. Tian, H. Fu, L. Jing, B. Xin and K. Pan, *J. Phys. Chem. C,* 112 (2008) 3083-3089.

[22] Y. Hu, H. L. Tsai and C.L. Huang, *J. Eur. Ceram. Soc.,* 23 (2003) 691-696.

[23] I.S. Grover, S. Singh and B. Pal, *J. Nanosci. Nanotechnol., (2014) doi:*10.1166/jnn.2014.9072.

[24] A.S. Barnard and H. Xu, *ACS Nano,* 2 (2008) 2237-2242.

[25] H. Zhan and J. F. Banfield, *J. Mater. Chem.,* 8 (1998) 2073-2076.

[26] J.C. Yu, J. Yu, W. Ho, Z. Jiang and L. Zhang, *Chem. Mater.,* 14 (2002) 3808-3816.

[27] W. Li, C. Liu, Y. Zhou, Y. Bai, X. Feng, Z. Yang, L. Lu, X. Lu and K.Y. Chan, *J. Phys. Chem. C,* 112 (2008) 20539-20545.

[28] X. Zhang, Y.L. Chen, R.S. Liu and D.P. Tsai, *Rep. Prog. Phys.,* 76 (2013) 46401-46442.

8. Influence of SiO_2 coating over TiO_2 nanoparticles for photooxidation of some polycyclic aromatic hydrocarbons

8.1 Introduction

Heterogeneous photocatalysis using TiO_2 as a photocatalyst has shown a high potential [1-5] for degradation of many organic contaminants because of its low cost, low toxicity, high stability, and high photoefficiency compared with other photocatalysts. However, less S_{BET} of TiO_2, causing less adsorption of reacting molecules on its surface is disadvantageous towards its high PCA. Within this context, modification of TiO_2 through its attachment with inert compounds specifically with SiO_2 has drawn increasing research interest [6-13] to increase the S_{BET} and PCA. The larger band gap and relative location of the Fermi level of SiO_2 to that of TiO_2 suggest [8,14,15] that the complete over-coating of the later by the former should hinder the transport of photoproduced charge carriers (e^-/h^+) from the TiO_2, where they are formed, to the surface, thus enhancing their recombination and blocking photoactivity.

Interestingly, presence of SiO_2 in its nanocomposite with TiO_2 necessarily may not show the deleterious effect for the PCA. But in-fact it assisted to bring significant enhancement in the PCA for TiO_2. The relevant examples includes the photooxidation of β-naphthol [16], methylene blue [17], rhodamine-6G [13], propyzamide [18] and propionaldehyde [19]. However, most of the studies for nanocomposite of SiO_2 and TiO_2 exhibit the use of P25 [7,11-15], and few have demonstrated other TiO_2 shapes and crystal structures [6,8-10]. Since, by manipulating both of these parameters, life time of photoexcited charge carriers and hence PCA [1-5] can be remarkably improved. Therefore, by selecting appropriate shape and phase of TNP and thereafter coating it with SiO_2, the PCA can be enhanced that could be utilized for the degradation of pollutants such as PAHs. Toward this end, C-5 nanoparticles which were found (*section-7.3*, chapter-7) to be composed of almost pure anatase phase and mixed morphologies (nanorods and nanopolygons) exhibiting much higher PCA than P25, were modified with SiO_2 and comparatively studied with bare P25 for the degradation of naphthalene and anthracene to CO_2 along with determination of their photoproduced intermediates.

8.2 Experimental section

*8.2.1 Preparation, characterization and photocatalytic activity for silica coated TiO_2 nanoparticles***:** The C-5 particles (*section-2.2.5*) were synthesized and coated (*section-2.2.7*) with

SiO_2 by method as reported chapter-2. These as-prepared catalysts were characterized by EDS (*section-2.5.2*), TEM (*section-2.5.3*), DRS (*section-2.5.9*), S_{BET} (*section-2.5.10*) and FT-IR (*section-2.5.11*) techniques, and are described in chapter-2. The PCA of these catalysts were performed by photooxidation of naphthalene and anthracene (*section-2.6.1*of chapter-2). The reaction samples were analyzed by UV-Vis. spectrophotometer (*section-2.6.3*), GC (*section-2.6.5*) and GC-MS (*section-2.6.6*) techniques and are described previously in chapter-2.

8.3 Results and discussion

The DRS (Fig. 8.1a) for bare C-5 particles in comparison to its nanocomposite with SiO_2 showed a decrease in absorption of UV-light from S-C-5(1) to S-C-5(4), indicating the coverage of SiO_2 on C-5 surface restraining the absorption of UV light. The peaks observed in FT-IR spectra of as-prepared samples (Fig. 8.1b) at 678 and 505 cm^{-1} could be attributed for symmetric stretching of O–Ti–O bond and bending vibration of Ti–O bond, respectively. Whereas, a new distinct and strong peak at 1081 cm^{-1} observed for silica coated samples can be assigned to the asymmetric Si–O–Si stretching indicating the presence of SiO_2 in coated as-prepared C-5 samples. An absorption peak at 950 cm^{-1} in the nanocomposites of SiO_2 and C-5, indicate the Ti–O–Si bond formation [9] which becomes more and more intense with increase in amount of silica precursor (10-40 µl/50 mg of catalyst) indicating towards the growth of silica layer on the C-5 particles.

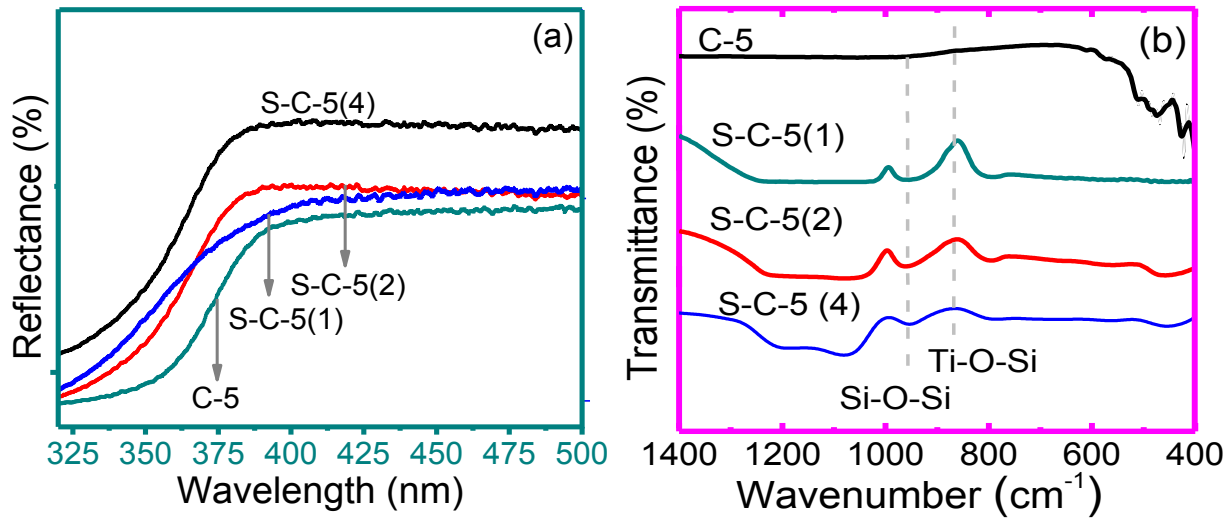

Fig. 8.1 (a) Diffuse Reflectance spectra and (b) FT-IR spectra of as-prepared catalysts.

The HR-TEM analysis revealed the morphology of the samples S-C-5(2) (Fig. 8.2) and S-C-5(4) (Fig. 8.3) to be of mixture of nanorods (diameter = 7-12 nm and length = 60-110 nm)

and nanopolygon (diameter = 60-70 nm) like particles, as shown in section 7.3 of chapter-7. The sample S-C-5(2) show (Fig. 8.2a-c) layer of SiO_2 (thickness ~12 nm) around the clumped TiO_2 nanoparticles, and EDS pattern (Fig. 8.2d) further confirms the presence of Si (0.81 at.%) in the sample. In case of sample S-C-5(4) (Fig. 8.3 a-c), due to over-coating with SiO_2, the C-5 particles are surrounded by SiO_2 matrix with amount of Si = 4.39 at.%, as confirmed by EDS pattern (Fig. 8.4d).

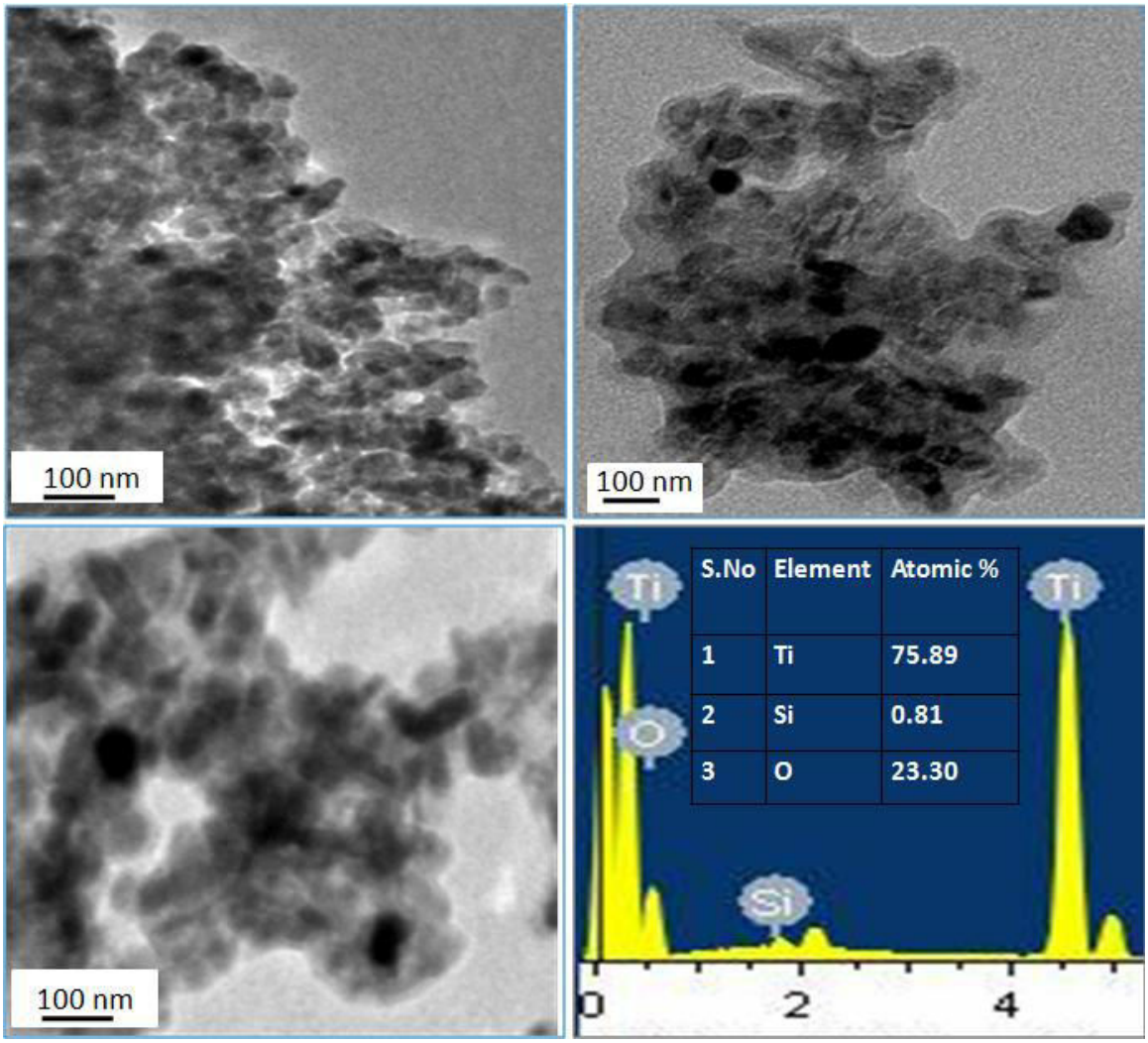

Fig. 8.2 (a-c) HR-TEM images for S-C-5(2) and (d) EDS pattern.

Since, surface area of the catalyst is well known to affect the adsorption and photocatalytic activity, therefore before assessing the comparative PCA of the as-prepared catalysts, their S_{BET} and dark adsorption of the reacting substrates were analyzed. It has been found that, the trend for decreasing S_{BET} to be S-C-5 (4) (235 m^2g^{-1}) > S-C-5(2) (194 m^2g^{-1})

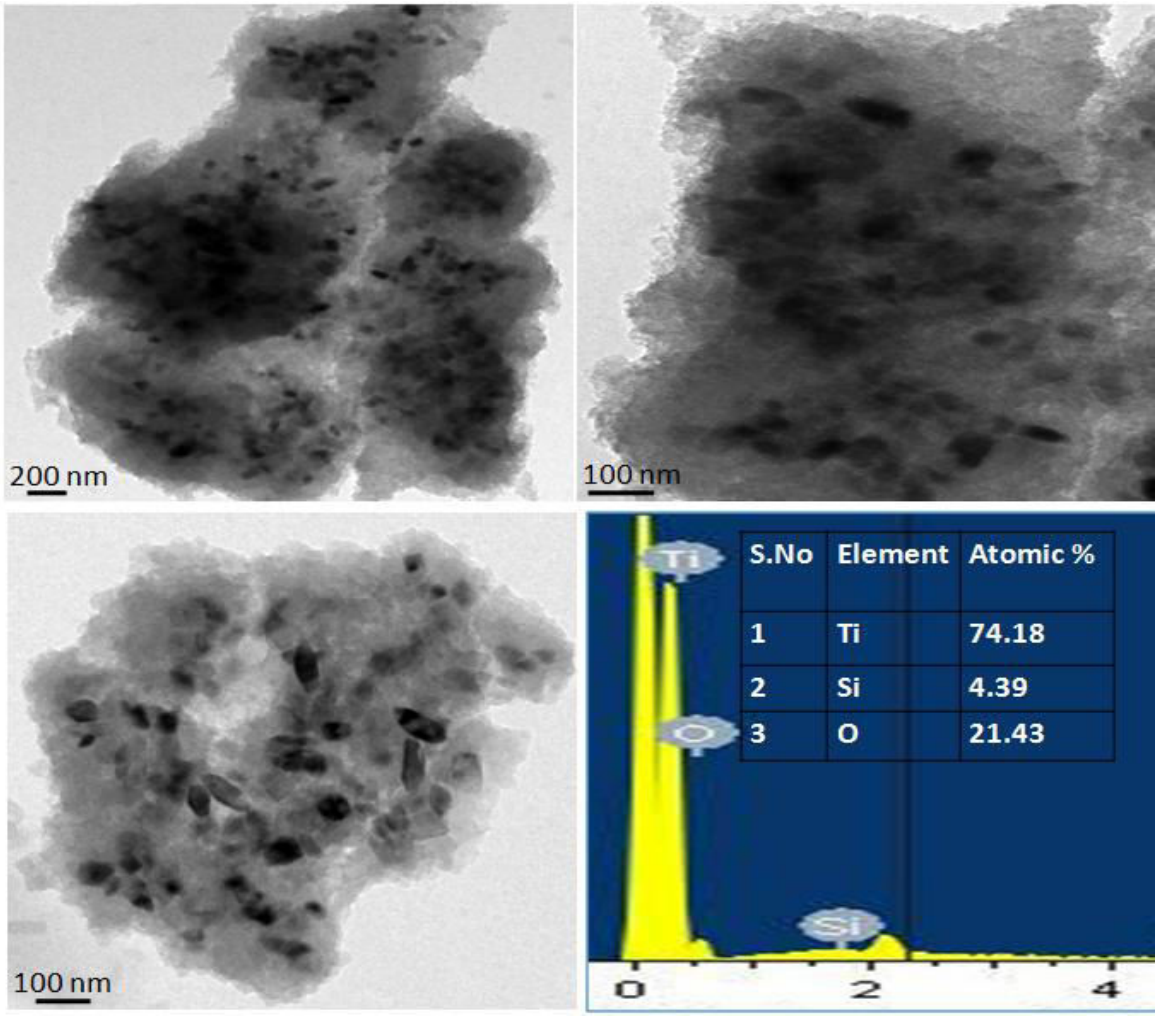

Fig. 8.3 (a-c) HR-TEM images for S-C-5(4) and (d) its EDS pattern.

> S-C-5(1) (134 m^2g^{-1}) > C-5 (79 m^2g^{-1}) and apparent rate constants of pseudo-second order kinetics (k_1) for dark adsorption of the naphthalene (Fig. 8.4a) and anthracene (Fig. 8.4b) are similar, where S-C-5(4) having highest S_{BET} exhibit highest values for k_1 (naphthalene = 5.9 × 10^{-1} g $mg^{-1}min^{-1}$ and anthracene = 6.5 ×10^{-1} g $mg^{-1}min^{-1}$), thus emphasizing the role of increased S_{BET} for facilitating adsorption of reacting molecules and is in correlation with previous reports [7, 11,12] for SiO_2 coated P25 and/or spherical TiO_2 [6,9,10]. Interestingly, for both of reacting molecules, the adsorption equilibrium is attained in initial 5 minutes, thereafter the surface of catalyst becomes saturated and subsequently it follows an exponentional behavior.

However, trends for the photooxidation of naphthalene (Fig. 8.4a) and anthracene (Fig. 8.4b) are not in correlation with the trends expected from the dark adsorption studies. The

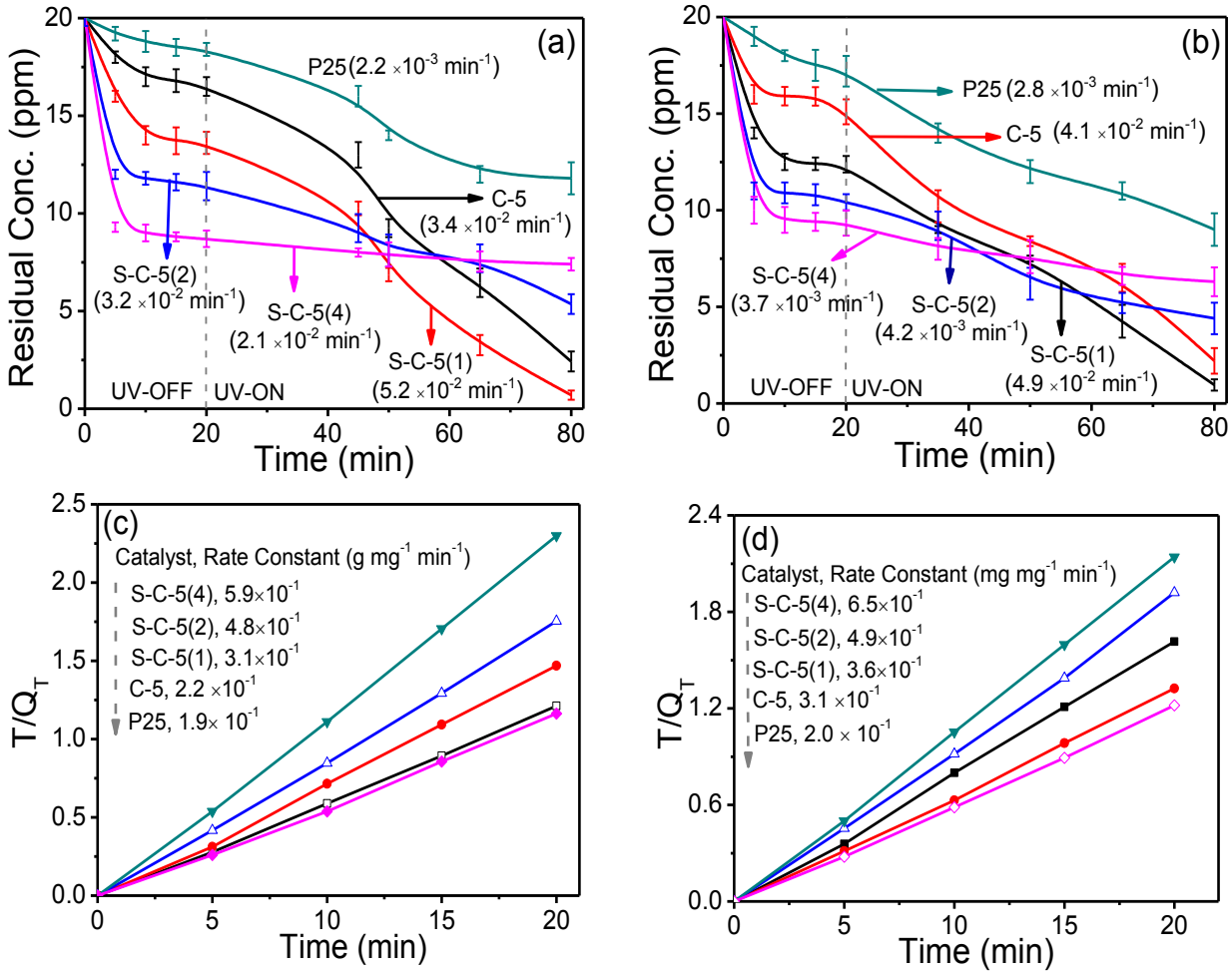

Fig. 8.4 Photodegradation of (a) naphthalene, (b) anthracene; inset: pseudo first order rate constants; pseudo second order dark adsorption kinetics for (c) naphthalene and (d) anthracene.

degradation for both these substrates were found to follow pseudo first order kinetics, where S-C-5(1) catalyst showed highest value of apparent rate constant (k) for photooxidation of naphthalene (5.2×10^{-2} min^{-1}) and for anthracene (4.9×10^{-2} min^{-1}).

Although, almost complete degradation of naphthalene and anthracene was observed with S-C-5(1) catalyst, yet it was not completely mineralized as reflected by their GC-MS analysis (Fig. 8.5), showing the formation of 1-napthol and 1,4-naphthalenedione, and the formation of 1-hydroxy-9-10-anthracenedione; 9,10-anthracenedione intermediates after 60 min of their photooxidation respectively, indicating requirement of more time for their complete mineralization.

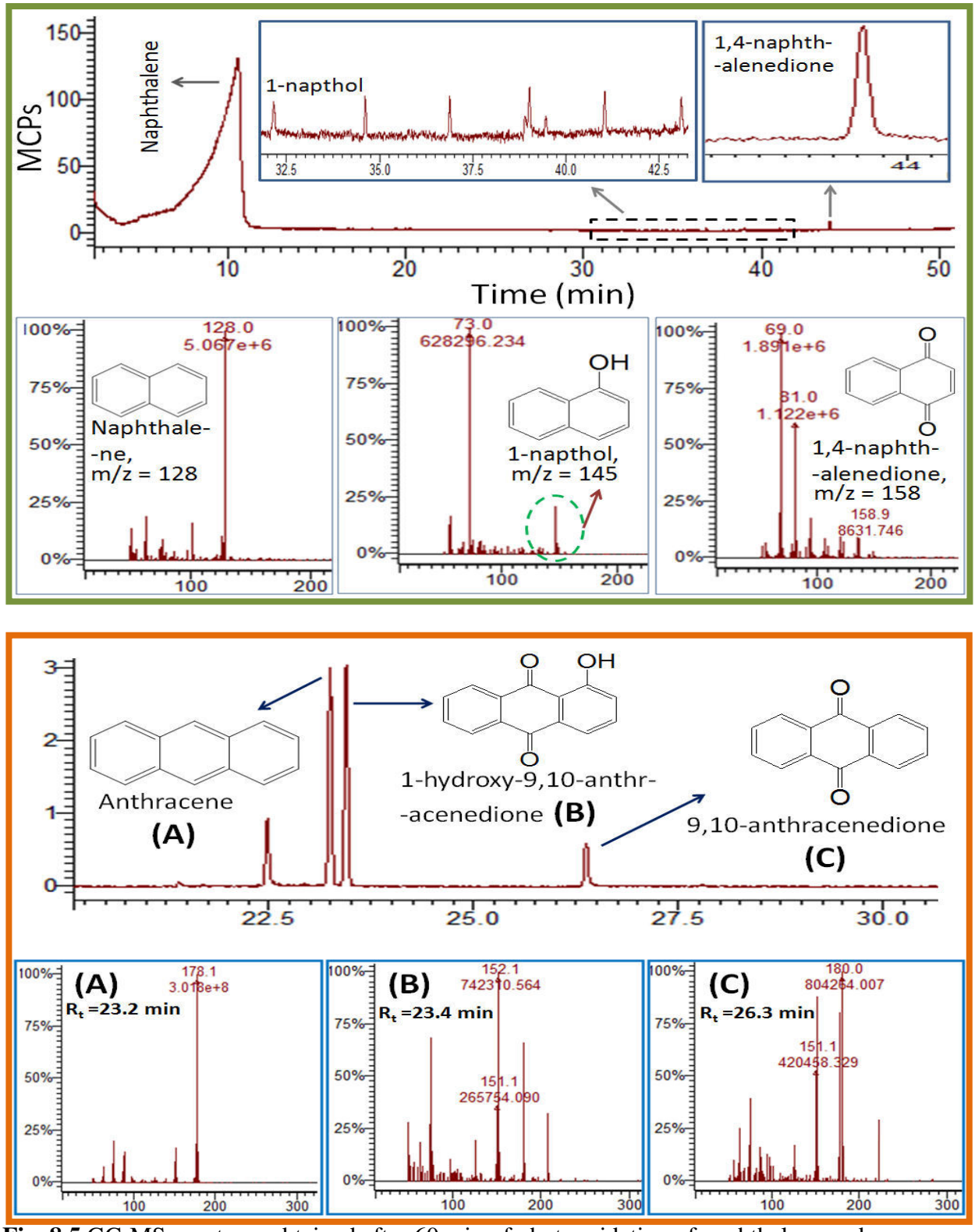

Fig. 8.5 GC-MS spectrum obtained after 60 min of photooxidation of naphthalene and anthracene in presence of S-C-5(1) catalyst.

Time course study for CO_2 formation (Fig. 8.6a-b) showed similar trends for photooxidation (Fig. 8.4a-b) of naphthalene and anthracene. The S-C-5(1) catalyst showed highest PCA for CO_2 formation, determined to be 50.1ppm (5.7 µmol = 73%) and 53.5 ppm (6.1 µmol = 78%) after 240 min of UV-light exposure and is less than the amount expected (7.8 µ mol) after complete mineralization of naphthalene (10 times the initial amount; inset Fig. 8.5a) and anthracene (14 times initial amount; inset Fig. 8.5b), respectively.

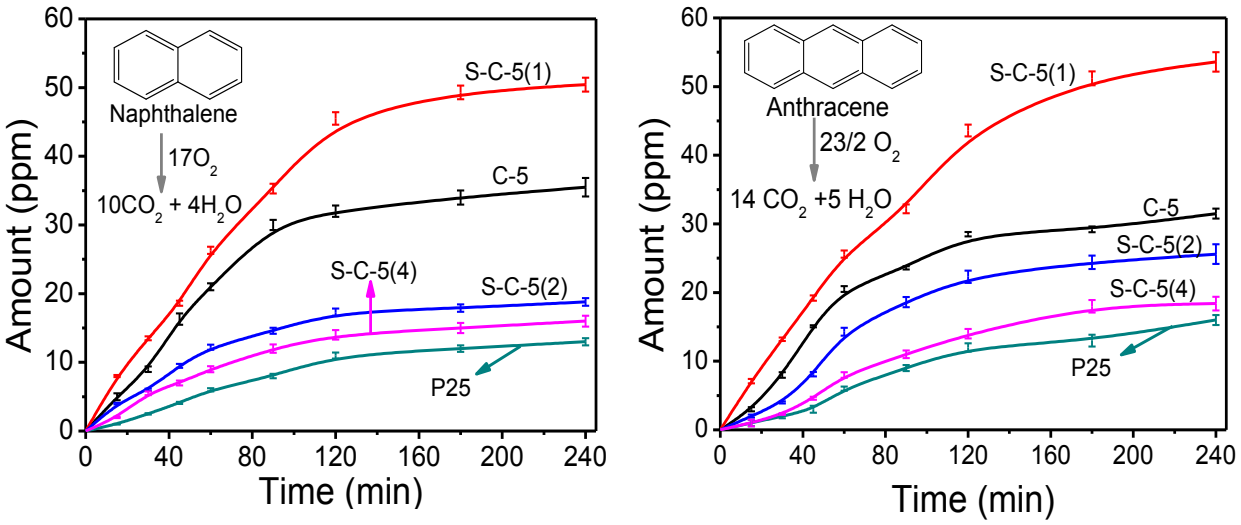

Fig. 8.6 CO_2 formation during photooxidation in presence of various TiO_2 catalysts.

The highest PCA of S-C-5(1) catalyst can ascribed to the mechanism of improved mass transfer where adsorption on the silica surface followed by surface diffusion of the contaminant(s) into the TiO_2 domains cause more interactions of molecules with it and hence high PCA than its bare counterpart. However, the increase in thickness of SiO_2 decreses the absorption of UV-light (Fig. 8.1a), thereby diminishing the formation of necessary e^-/h^+ pair and hence PCA. These results are in correlation to the recent work of Nussbaum et al. [8], showing thin layer of SiO_2 onto TiO_2 to be the cause for the enhanced photooxidation rates for degradation of salicylic acid.

8.4 Conclusions

In summary, coating of SiO_2 increases the surface area of TiO_2, hence the adsorption of the reacting molecules and its extent being in direct proportion to SiO_2 thickness. Overcoating of TiO_2 by SiO_2 deteriorates its photocatalytic activity ascribed to decrease in adsorption of necessary UV-light.

8.5 References

[1] I.S. Grover, S. Singh and B. Pal, *Appl. Surf. Sci.,* 280 (2013) 366-372.

[2] I.S. Grover, S. Singh and B. Pal, *J. Nanosci. Nanotechnol.,* (2014) doi:10.1166/jnn.2014.9072

[3] X. Chen and S.S. Mao, *Chem. Rev.,* 107 (2007) 2891-2959.

[4] I.S. Grover, S. Singh and B. Pal, *RSC Adv.*, 4 (2014) 24704-24709.

[5] Y. Ishii, Y. Kanamori, T. Kawashita, I. Mukhopadhyay and S. Kawasaki, *J. Phys. Chem. Solids,* 71 (2010) 511-514.

[6] P. Wilhelm and D. Stephan, *J. Photochem. Photobiol. A Chem.,* 185 (2007) 19-25.

[7] Q. Zhang, J.B. Joo, Z. Lu, M. Dahl, D.Q.L. Oliveira, M. Ye and Y. Yin, *Nano Res.,* 4 (2011)103-114.

[8] M. Nussbaum and Y. Paz, *Phys. Chem. Chem. Phys.*, 14 (2012) 3392-3399.

[9] A. Hilonga, J.K. Kim, P.B. Sarawade and H.T. Kim, *Powder Technol.,* 199 (2010) 284-288.

[10] S. Wang, T. Wang, W. Chen and Teruo Hori, *Chem. Commun.,* (2008) 3756-3758.

[11] S. Hu, F. Li and Z. Fan, *Bull. Kor. Chem. Soc.,* 33 (2012) 1895-1899.

[12] Y. Ren, M. Chen, Y. Zhang and L. Wu, *Langmuir,* 26 (2010) 11391-11396.

[13] C. Anderson and A.J. Bard, *J. Phys. Chem.* 99 (1995) 9882-9885.

[14] H. Nur, *Mater. Sci. Eng. B,* 133 (2006) 49-54.

[15] H.S. Lee, S.M. Koob and J.W. Yoo, *J. Ceram. Process. Res.,* 13 (2012) 300-303.

[16] S. Qourzal, N. Barka, M. Tamimi, A. Assabbane, A. Nounah, A. Ihlal and Y. Ait-Ichou, *Mater. Sci. Eng. C,* 29 (2009) 1616-1620

[17] F. Mei, C. Liu, L. Zhang, F. Ren, L. Zhou, W.K. Zhao, Y.L. Fang, *Cryst. Growth Desig.,* 292 (2006) 87-91.

[18] T. Torimoto, S. Ito, S. Kuwabata and H. Yoneyama, *Environ. Sci. Technol.,* 30 (1996) 1275-1281.

[19] N. Takeda, T. Torimoto, S. Sampath, S. Kuwabata, H. Yoneyama, *J. Phys. Chem.,* 99 (1995) 9986-9991.

9. Preparation and characterization of TiO_2 nanowires for improved photocatalytic activity under sun light irradiation

9.1 Introduction

Elongated TiO_2 nanostructures such as TNW has been demonstrated [1-13] as an attractive photocatalyst due to its higher surface area, porous structure, superior charge transfer and suitable band edge positions with respect to oxidation/reduction potential of the functional groups. It has been found that TNW exhibits improved PCA [1,3-5,9-11] than well known most photoactive P25. For instance, Wang et al. [4] and Mandal et al. [9] found 5 and 2-fold higher photocatalytic activity for anatase and rutile TNW than P25 for the degradation of methylene blue dye. This PCA of TiO_2 nanostructure including TNW can be further improved by controlling the recombination process of excited charge carriers. It can be achieved by making hetero-junctions of TiO_2 in its crystal structures (anatase/rutile and anatase/brookite) and/or loading of noble metal.

In case of crystal phased hetero structure, the relative dislocation of the conduction and valence band positions favor migration of charge carriers from one phase to another and thereby efficiently suppresses the recombination process. However, this system has been rarely considered for TNW [5,10] but well studied for other [13-18] TiO_2 nanoparticles. A report by Liu et al. [5] demonstrated that TNW having anatase and brookite phase exhibited higher photocatalytic activity than TNW with any of these phases alone, which was suggested to be due to the synergetic effect of these phases. This PCA of TNW can be further notably improved by noble metal loading which act as an electron sink for photoproduced electrons and is discussed in *section* of chapter-1 and proved in chapters-4 (*section-4.3*),-5 (*section-5.3*), and -6 (*section-6.3*). In addition, the loaded noble metal also extends the absorption of TiO_2 from UV- to Vis-region, by well known phenomenon of surface plasmon resonance (SPR) that facilitates to use of such TiO_2 catalyst under direct sun-light (having > 90 % of visible light) for degradation of organic pollutants. Toward this end, present chapter consider the synthesis of mixed phased (anatase and rutile) TNW, photodeposited by Au nanoparticles and studied in comparison to P25 for photocatalytic decomposition of propiconazole to CO_2 under UV- and sun-light.

9.2 Experimental Section

9.2.1 Synthesis, characterization and photoactivity of bare and Au-photodeposited TNW: TNW were synthesized as per method discussed in *section-2* of chapter-2. Au loading was done by photodeposition method and is described in *section-2.4.1* of chapter-2. These as-prepared samples were characterized by XRD (*section-2.5.1*), SEM (*section-2.5.2)*, TEM (*section-2.5.3*) and time resolve photoluminescence (*section-2.5.7*) techniques as described in chapter-2. The bare and Au-loaded TNW were used in comparison to the photodegradation of the propiconazole fungicide under UV and sun-light, as describe in *sections-2.6.1* (chapter-2).

9.3 Results and Discussion

The XRD analysis (Fig. 9.1) for TNW in comparison to P25 showed the existence of anatase (JCPDS card number 21-1272) and rutile (JCPDS card number 21-1276) phases as revealed by their characteristics peaks at 2θ = 25.3° and 27.5°, respectively. High diffraction, sharp and intense peaks indicating crystalline TNW which is needed for an efficient photocatalyst. The weight fraction of anatase and rutile phases in TNW ca. by reported method [14] is found to be 72% and 28% and is almost similar to that found for P25 (anatase =70% and rutile = 30%). Moreover, the mean crystallite size ca. using Scherrer equation (*section-2.5.1* of chapter-2) for TNW (anatase = 32.0 nm and rutile = 33.8 nm) is found to be smaller than the P25 (anatase = 34.6 and rutile = 40.8 nm).

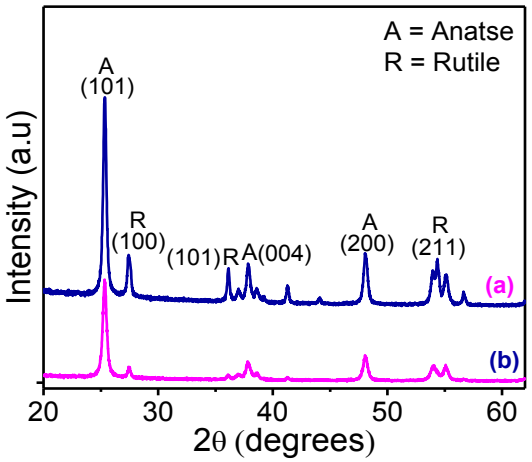

Fig. 9.1 XRD patterns for (a) TiO_2 nanowires and (b) P25.

The SEM images (Fig. 9.2a-d) at different resolutions show many TNW with diameter of 82-420 nm and length in few hundreds of nanometers. The TEM analysis (Fig. 9.3a-d) of Au-TNW sample show TNW particles of diameter = 78-415 nm which is in agreement with the SEM analysis. It can be clearly seen (Fig. 9.3c-d) that Au-nanoparticles of narrow size distribution (3-5 nm) were very finely deposited on the surface of many TNW particles.

The S_{BET} of TNW (148 m^2g^{-1}) is found to be ~2.7 times more than that possessed by P25 (59 m^2g^{-1}) indicating its highly porous structure. However, the S_{BET} of TNW was reduced to 136 m^2g^{-1} after 1 wt% Au-photodeposition onto it, ascribed to its surface coverage with Au-deposits.

Similar results for the decrease in S_{BET} after deposition of coinage metals over titania nanostructures were recently reported [16,19] by our group.

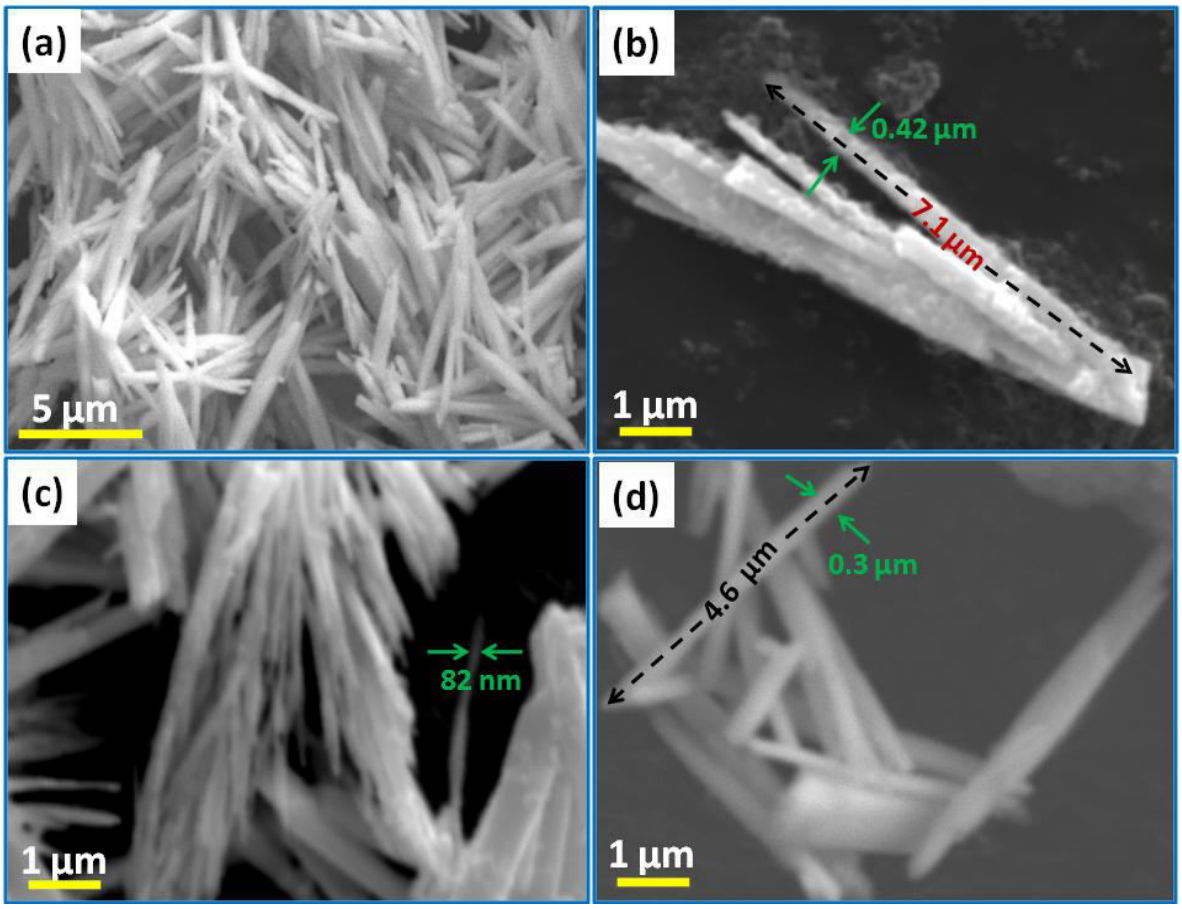

Fig. 9.2 (a-d) SEM images for TiO_2 nanowires

The DRS spectra (Fig. 9.4a) used to study reflectance/absorption of catalysts in UV-visible light, clearly showed that Au-loading decreases the reflectance i.e., increases the absorption of TNW in visible region (400-700 nm) which is higher in relation to P25 and is required for better activity of a photocatalyst in visible region. Time resolve photoluminescence decay indicating average charge recombination time, was also relatively measured (Fig. 9.4b) before assessing the PCA of as-prepared catalysts. The average relaxation time of excited charge carriers determined for TNW (57 µs) (*section- of chapte-2*) is found to be around 12 µs more than that of P25, and improved to 79 µs for Au-TNW catalyst (Fig. 9.4b). As the photodeposited Au act as a sink for the photogenerated electrons, therefore life time of these charged species is significantly improved. These results are in accordance with our [19] and others [20,21] reports where metal loading is found to improve average relaxation time of excited charge carriers.

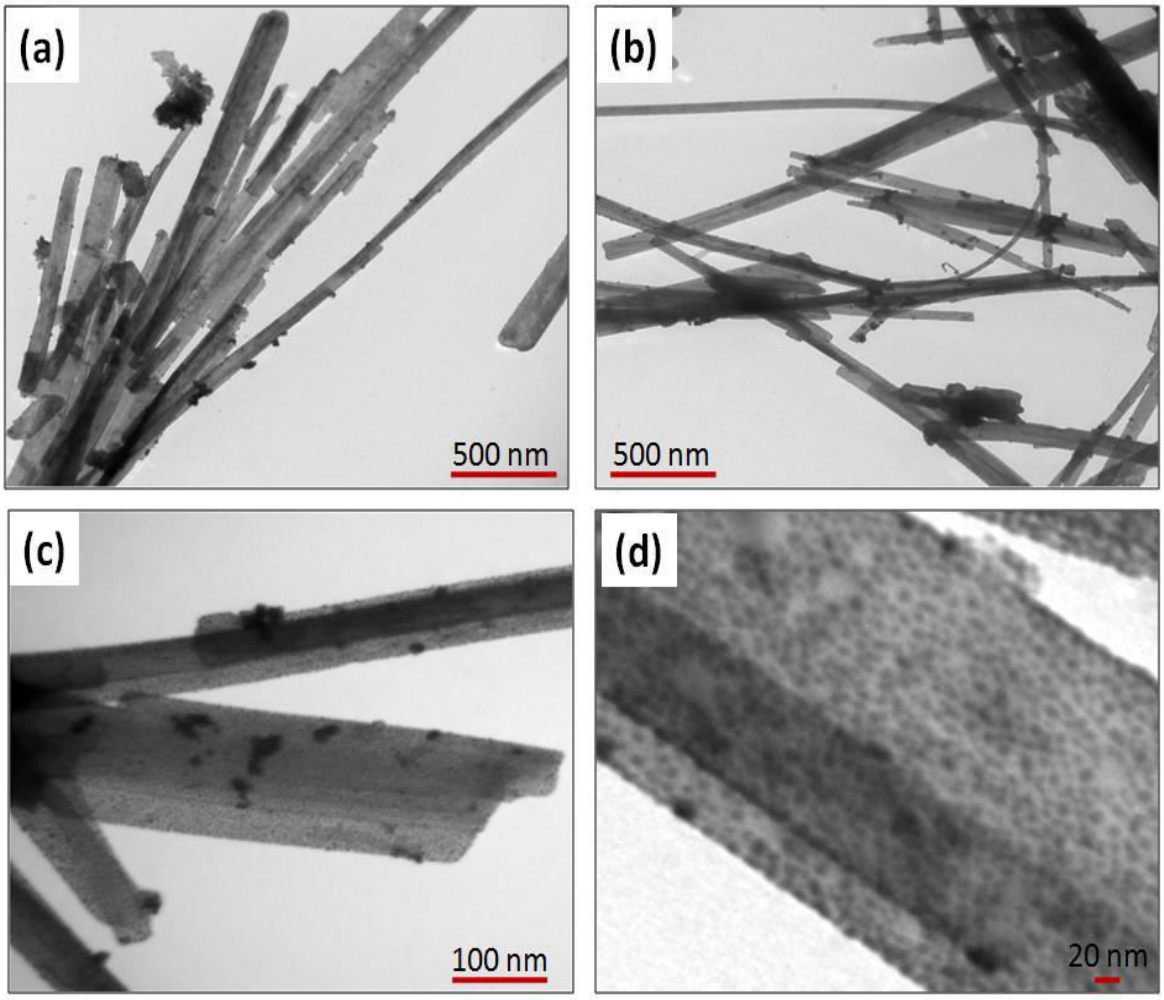

Fig. 9.3 (a-d) TEM images for Au-loaded TiO_2 Nanowires.

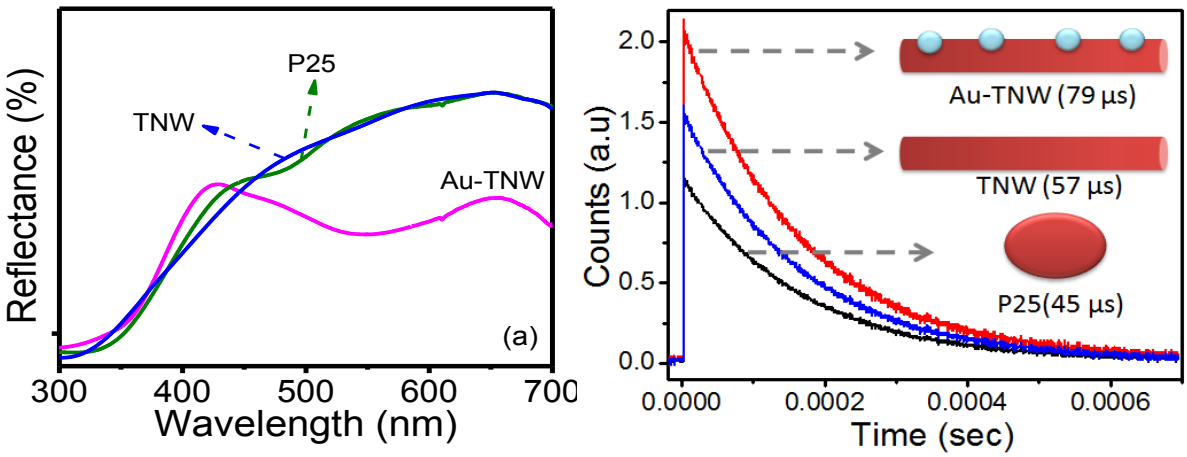

Fig. 9.4 (a) DRS and (b) Time resolve photoluminescence decay studies for TiO_2 catalysts

Time dependant photocatalytic degradation of propiconazole under UV- and sun-light using TNW as photocatalyst always showed better performance than P25 and is further improved for Au-TNW catalyst (Fig. 9.5a-b). This degradation was found to follow pseudo-first order kinetics where Au-TNW exhibited highest apparent rate constants (k) of 3.9 $\times 10^{-2}$ min^{-1} and 4.9 $\times 10^{-2}$ min^{-1}, under UV- and Sun-light irradiation, respectively. Interestingly, Au-TNW is also found to quickly degrade propiconazole under Sun-light than that found under UV-light irradiation, indicating its better ability to effectively utilize the visible region of solar spectrum for photooxidative removal of this pesticide. This is in correlation with previous reports of noble metal loaded TiO_2, exhibiting higher PCA [13,14,21] under visible-light.

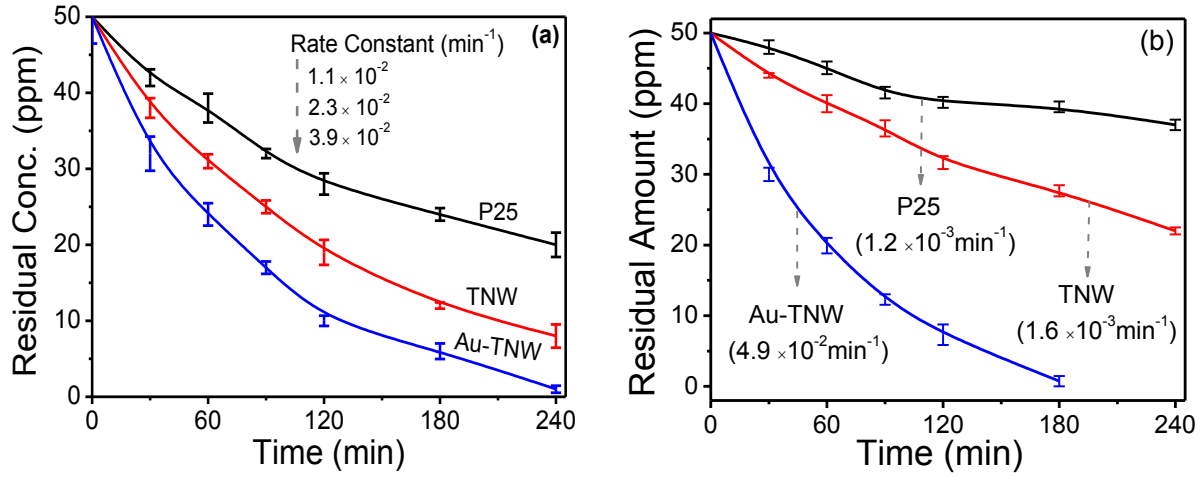

Fig. 9.5 Photocatalytic activity of TiO_2 catalysts under (a) UV-light; inset pseudo-first order rate constants, and (b) Sun-light.

Although, after 240 min of UV-light exposure, Au-TNW catalyst showed complete oxidative removal of propiconazole, yet incomplete mineralization occurs because of formation of some heteroatom containing small molecules which were identified as 2-ethylhexanoic acid and nitrobenzene by the GC-MS study (Fig. 9.6). Therefore, CO_2 formation during photooxidation of propiconazole was quantitatively measured to determine the extent of its decomposition.

Time course study for CO_2 formation during photooxidation of propiconazole under UV- (Fig. 9.7a) and visible-light (Fig. 9.7b) showed steady increase in its concentration with the illumination time. It is noticed that trends for CO_2 formation in UV and visible lights by using different TiO_2 catalysts is similar to the photooxidation of propiconazole, where bare and Au-

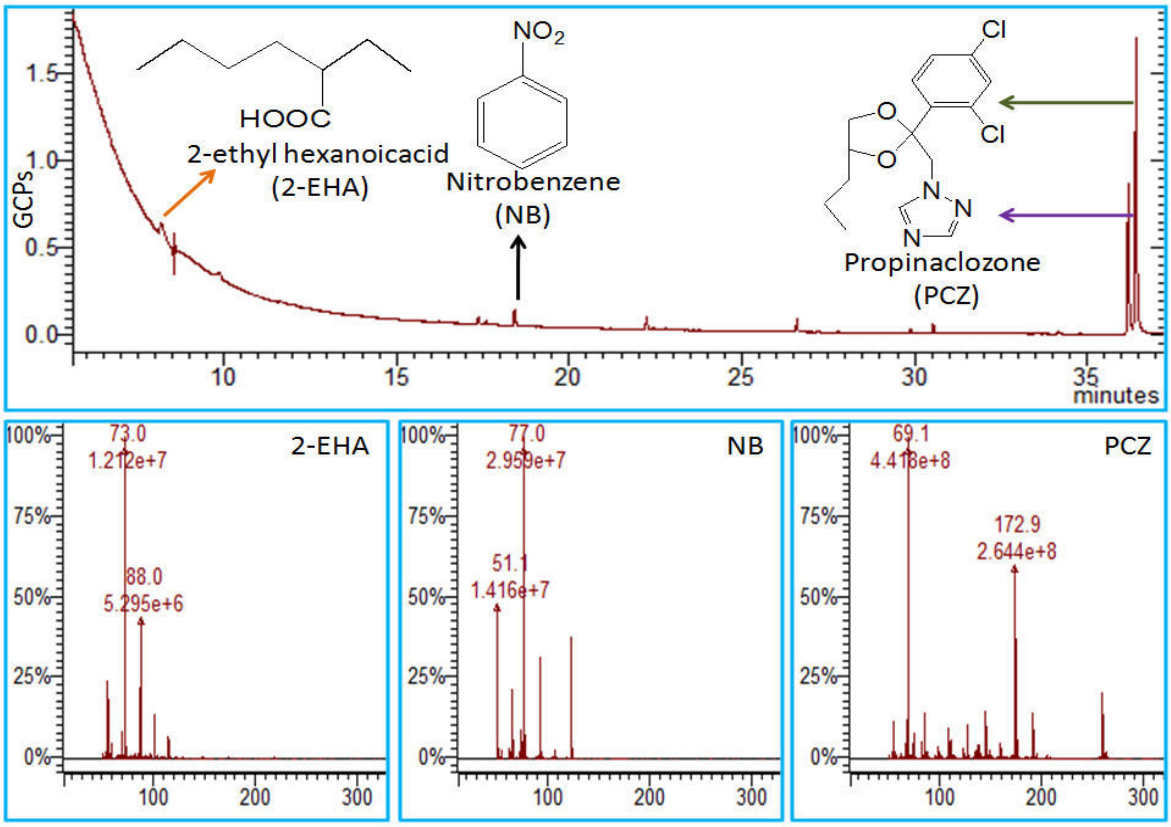

Fig. 9.6 GC-MS chromatograms for identified photoproduced intermediates during degradation of propiconazole using Au-photodeposited TNW.

loaded TNW exhibited higher (1.3 - 40.0 times) rate for its formation than P25. The highest amount of CO_2 formed by Au-TNW catalyst under UV- (53 ± 1.2 ppm) and Sun- light (7 5 ± 1.5 ppm) corresponds to ~ 60 and 76 % of mineralization, respectively.

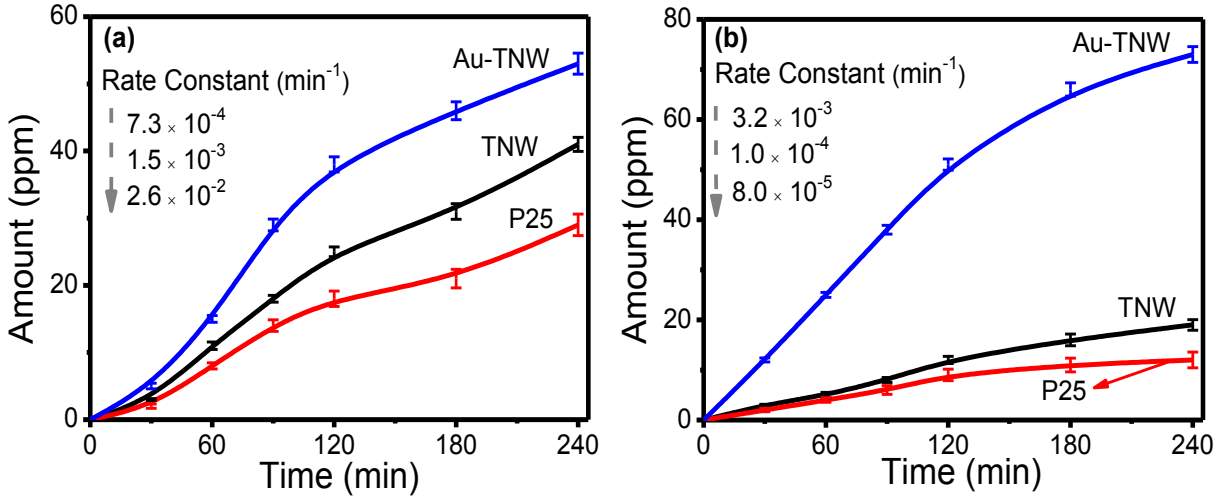

Fig. 9.7 CO_2 formation during photodecomposition of propiconazole using TiO_2 catalysts under illumination of (a) UV-light and (b) Sun-light; inset pseudo-first order rate constants.

This higher photocatalytic activity of TNW than P25 can be ascribed to the comparatively higher relaxation time (Fig. 9.4b) of the excited charge carriers, resulting into more availability of h^+ that can either directly oxidize the propiconazole or forms the oxidative hydroxyl radicals. At the same time available electrons can reduce the molecular oxygen to oxidative superoxide radicals, thereby further enhancing the degradation rates. The small anatase and rutile crystallite size for TNW than P25 is also responsible for better photocatalytic activity of former catalyst, since it is well known that titania nanocrystals with small crystallite size is a better photocatalyst [13-15] than larger crystallites. Moreover, presence of relatively higher fraction (2%) of crystalline anatase phase corresponding to (101) acting as better adsorption sites for electron scavenging O_2 molecules facilitating the formation of oxidative superoxide radicals, could also be a cause for higher catalytic activity of TNW. This is in agreement with our recent report [15] where presence of crystalline anatase as a major phase was found to be the cause for higher activity of prepared TiO_2 catalysts than P25. The low activity of the TNW under UV-light to that found under visible-light is due its very low adsorption in former light spectrum region (Fig. 9.4a). This resulted lesser excited charger carries and hence reduction in formation of oxidative radical species that in turn decreases the activity.

The Au-loading notably improves the photocatalytic activity owing to rapid charge transfer and Fermi energy level equilibrium at the Au-TiO_2 interface which by acting as electron sink, increases the life time of excited charge carries (Fig. 9.4b) and hence photocatalytic activity. It is also observed that, the activity of Au-TNW under sun-light is much higher than that found in UV-light. This could be ascribed to the localized surface plasmon resonance excitation, where highly energetic (*ca.* 2.23 eV) photoproduced electrons of Au overcome the interfacial energy gap (0.96 eV) between its Fermi level and conduction band of TiO_2 can easily diffuses to later, thereby increasing the radical generation [21] and hence photocatalytic activity.

9.4 Conclusions

In summary, mixed phased TiO_2 nanowires were successfully prepared and decorated with very fine Au nanoparticles through a facile photodeposition technique. The TiO_2 nanowires because of improved charge dynamics exhibited enhanced photocatalytic activity than P25 for the degradation of propiconazole to CO_2 under UV- and sun-light, and was further improved by Au-loading. Our study also suggests that visible light in the solar spectrum can be utilized for

decomposition of propiconazole, and if optimized, can be effectively used for the fast and complete decomposition of the other pollutants.

9.5 References

[1] F. Dong,W. Zhao and Z. Wu, *Nanotechnology,* 19 (2008) 365607-365617.

[2] L. Ge, J. Liu, *J. Phys. Conf. Ser.,* 188 (2009) 12019-122022.

[3] M.C. Wu, H.C. Liao, Y.C. Cho, C.P. Hsu, T.H. Lin, W.F. Su, A. Sapi, A. Kukovecz, Z. Konya, A. Shchukarev, A. Sarkar, W. Larsson, J.P. Mikkola, M. Mohl, G. Toth, H. Jantunen, A. Valtanen, M. Huuhtanen, R.L. Keiski and K. Kordas, *J. Nanopart. Res.,* 16 (2014) 2143-2154.

[4] C. Wang, L. Yin, L. Zhang, N. Liu, N. Lun and Y. Qi, *Appl. Mater. Interfaces,* 2 (2010) 3373-3377.

[5] B. Liu, A. Khare and E.S. Aydil, *Appl. Mater. Interfaces,* 3 (2011) 4444-4450.

[6] B. Liu, H.M. Chen, C. Liu, S.C. Andrews, C. Hahn, P. Yang, *J. Am. Chem. Soc.,* 135 (2013) 9995-9998.

[7] Q. Li, B. Cheng, X. Yang, R. Liu, B. Liu, J. Liu, Z. Chen, B. Zou, T. Cui and B. Liu, *J. Phys. Chem. C,* 117 (2013) 8516-8521.

[8] B. Wen, C. Liu and Y. Liu, *Inorg. Chem. Commun.,* 44 (2005) 6503-6505.

[9] S.S. Mandal and A.J. Bhattacharyya, *Talanta,* 82 (2010) 876-884.

[10] W. Zhou and Y. He, *Chem. Eng. J.,* 179 (2012) 412-416.

[11] J. Jitputti, Y. Suzuki and S. Yoshikawa, *Catal. Commun.,* 9 (2008) 1265-1271.

[12] X. Lv, H. Zhang and H. Chang, *Mater. Chem. Phys.,* 136 (2012) 789-795.

[13] K. Nakata and A. Fujishima, *J. Photochem. Photobiol. C Photochem. Rev.,* 13 (2012) 169-189.

[14] X. Chen and S.S. Mao, *Chem. Rev.,* 107 (2007) 2891-2959.

[15] I.S. Grover, S. Singh and B. Pal, *RSC Adv.,* 4(2014) 24704-24709.

[16] I.S. Grover, S. Singh and B. Pal, *Appl. Surf. Sci.,* 280 (2013) 366-372.

[17] T. Luttrell, S. Halpegamage, J. Tao, A. Kramer, E. Sutter and M. Batzill, *Sci. Rep.,* 4 (2014) 4043-4050.

[18] S.G. Kumar and L.G. Devi, *J. Phys. Chem. A,* 115 (2011) 13211-13241.

[19] I.S. Grover, S. Singh and B. Pal, *J. Nanosci. Nanotechnol.*, (2014) doi:10.1166/jnn.2014.9072

[20] A. Yamakata, T.A. Ishibashi and H. Onishi, *J. Phys. Chem. B,* 105 (2001) 7258-7262.

[21] X. Zhang, Y.L. Chen, R.S. Liu and D.P. Tsai, *Rep. Prog. Phys.,* 76 (2013) 46401-46442.

Conclusions

In summary, present work demonstrated the preparation and detailed characterization of different sizes, shapes, silica coated titania/titanate nanoparticles by DRS, XRD, SEM-EDS, TEM, Raman and time resolve photoluminescence techniques, including determination for their electro-kinetic properties and surface area analysis. These as-prepared nanostructures were modified by metal-loading and studied in comparison to their corresponding bare analogies and P25 for the decomposition of pesticides (imidacloprid, sulfosulfuron, propiconazole and methyl parathion) and PAHs (naphthalene and anthracene) by HPLC, UV-visible spectrophotometer, GC, GC-MS and IC techniques.

Chapter-1 covers general introduction to the photocatalysis, influence of size, shape and crystals structures of titania on the optical and electronic properties, which in-turn affects their photocatalytic activities. The properties such as inertness, transparency, porosity etc. making SiO_2 as a suitable shell material to be coated over TiO_2 are also discussed. An overview of the various studies reported earlier for the decomposition/degradation of environmental pollutants,namely, pesticides and PAHs was also discussed.

Chapter-2 described the experimental methods and techniques used for the determination of physico-chemical, opto-electronic and electro-kinetic properties of as-prepared catalysts.

In summary ***chapter-3*** correlated the crystal phase, surface, structural and electro-kinetic properties of bare, and Ag and Cu deposited TNT and TNR that were obtained from Degussa P25. By changing the size and shape depending on the preparation condition, causes the alteration in electronic charge of their surface and subsequently, the ζ value is markedly varied in case of different aqueous suspensions of TNP. These electro-kinetic parameters would be

beneficial for determining dispersion stability of TNP for potential use in metal oxide based nanofluids. The photocatalytic activity of TNT crystals for photo-oxidation of imidacloprid is found to be superior to the conventional best photoactive P25 owing to its largest surface area and hollow porous surface structure.

It was demonstrated in ***chapter-4*** that Ag-photodeposited TNT is an efficient catalyst for the decomposition of IMI to CO_2 and inorganic ions, and it notably recedes half-life of IMI to that found by most photoactive P25-TiO_2. Although, structural parameters of TNT were found to play a vital role for the improved decay constants, yet the detrimental influence of Na-atoms was not observed. The formation of number of identified intermediates reveal the complexity of photocatalytic process, suggesting the existence of various oxidation routes and non-specific attack of hydroxyl radicals that result in multi-step and interconnected pathways for decomposition of IMI. The fate of heteroatoms suggested their partial mineralization to inorganic ions and is manifested by the presence of heteroatom containing intermediates which were found to persist after the complete degradation of IMI.

Chapter-5 revealed the preparation of highly crystalline sodium titanate nanorods from amorphous sodium titanate nanotubes exhibiting comparable photoredox activities to that of P25 for photoreduction of m-DNB and photooxidation of sulfosulfuron. The increase in dimensionality of these nanorod particles increases the delocalization of electrons and decreases the e^-/h^+ recombination and hence make it more photoreductive like P25. Photodeposition of Au onto titania nanostructures not only improved the photoactivity but also changes the selectivity/yield for the formation of *m*-DAB and *m*-NA. The layered structure of sodium titanate nanotubes cause more adsorption of water molecules and corresponding formation of hydroxyl radicals resulting in its highest photooxidation activity.

Chapter-6 emphasized the combined effect of Au-loading and thermal treatment on the structure, morphology and photocatalytic activity of TNT. It was found that the extent of C_{Strain} induced in the crystal structure of TNT by the presence of Au influences the crystal phase, morphology, surface area and particle size during its thermal treatment, that in-turn affected the photocatalytic activity. Among a variety of as-prepared crystal structures, anatase and rutile phase with aid of Au in TNT-Au^o(PS) exhibited superior photocatalytic activity for the mineralization of imidacloprid to CO_2 than most photoactive P25-TiO_2, owing to higher lifetime of charge carriers for the former.

It can be concluded from ***chapter-7*** that rice-like anatase TiO_2 nanorods retain their anatase crystal structure after calcination at > 800 ^oC, whereas the P25 catalyst is converted to the rutile phase under similar experimental conditions. Although an increase in crystallinity and rate constant per unit surface area of this as-prepared stable anatase TiO_2 crystal phase played a vital role for superior photoactivity for MP degradation, the detrimental influences of decreased surface area, increased particle size and crystallite size are not observed for the C-2 to C-9 catalysts that were thermally treated at high temperatures.

Chapter-8 showed a coating of as-prepared TiO_2 catalyst having higher PCA than P25, by a method other than reported one, and if optimized, could be useful for coating of TiO_2 with desired SiO_2 thickness. The dark adsorption efficiency for the SiO_2 coated over TiO_2 catalysts was found to be a function of amount of silica precursor, affecting growth of SiO_2 onto TiO_2 surface. However, trend for mineralization of naphthalene and anthracene to CO_2 was opposite to the adsorption study, where S-C-5(1) exhibited highest PCA and was ascribed to the mechanism of improved mass transfer.

In **chapter-9**, preparation of TiO_2 nanowires of almost same phase composition to P25 but of higher S_{BET}, was demonstrated. These TNW displayed much higher PCA than P25 for decomposition of propiconazole under UV- and sun-light, that further improved after Au-loading, because of higher recombination time of photo-excited charge carriers.

List of publications

1. **Inderpreet Singh Grover**, Satnam Singh, Bonamali Pal, "Stable anatase TiO_2 formed by calcination of rice like titania nanorod at 800 ^oC exhibits high photocatalytic activity", ***RSC Advances***, 4 (2014) 24704-24709

2. **Inderpreet Singh Grover,** Satnam Singh and Bonamali Pal*, "Influence of thermal treatment and Au-loading on the growth of versatile crystal phase composition and photocatalytic activity of sodium titanate nanotubes", *RSC Advances,* doi: 10.1039/c4ra06605g

3. **Inderpreet Singh Grover**, Satnam Singh, Bonamali Pal, "The preparation, surface structure, zeta potential, surface charge density and photocatalytic activity of TiO_2 nanostructures of different shapes", ***Applied Surface Sciences***, 280 (2013) 366-372

4. **Inderpreet Singh Grover**, Satnam Singh and Bonamali Pal*, "Photodegradation of Imidacloprid insecticide by Ag deposited titanate nanotube- A study of intermediates products and its reaction pathways", ***Journal of Agriculture and Food Chemistry (revised submitted)***

5. **Inderpreet Singh Grover**, Satnam Singh, Bonamali Pal, "Enhanced photocatalytic activity of as-prepared sodium titanates for m-dinitrobenzene reduction and sulfosulfuron oxidation", ***Journal of Nanoscience and Nanotechnology***, 15(2015) 1490-1498

6. **Inderpreet Singh Grover,** Satnam Singh, Bonamali Pal, "Influence of thermal treatment and Fe-loading on Morphology, Crystal Structure and Photocatalytic activity of Sodium Titanate Nanotubes", ***Particulate Science and Technology*****,** doi: 10.1080/02726351.2014.943828

7. **Inderpreet Singh Grover**, Satnam Singh, Bonamali Pal, Priority PAHs in orthodox black tea during manufacturing process, ***Environmental Monitoring and Assessment***, 185 (2013) 6291-6294

8. **Inderpreet Singh Grover**, Rashmi Sharma, Satnam Singh, Bonamali Pal,"Polycyclic aromatic hydrocarbons in some grounded coffee brands", ***Environmental Monitoring and Assessment*****,** 185 (2013) 6459-6463

9. **Inderpreet Singh Grover,** Vishal, Satnam Singh, Bonamali Pal," Size and shape dependant synthesis of TiO_2 nanoparticles and study of their comparative photocatalytic activity" Science & Society, 9 (2011) 169-174

10. Bonamali Pal, Rupinder Kaur, **Inderpreet Singh Grover**, "Superior adsorption and photodegradation of Eriochrome Black-T dye by Fe^{+3} and Pt^{+4} impregnated TiO_2 nanostructures of different shapes", communicated to ***Environmental Science and Technology***, July 2014.

11. Inderpreet Singh Grover, Satnam Singh, Bonamali Pal, Priority PAHs in green and roasted beans of Arabica and Robusta coffee", communicated to ***Environmental Monitoring and Assessment*****,** July 2014

12. Inderpreet Singh Grover, Satnam Singh, Bonamali Pal, "Polycyclic Aromatic Hydrocarbons formed during roasting process in Arabica coffee beans", **(Manuscript under preparation)**

13. Inderpreet Singh Grover, Satnam Singh, Bonamali Pal, "Influence of SiO_2 coating over TiO_2 nanoparticles for photodegradation of Naphthalene and Anthracene", **(Manuscript under preparation)**

14. Inderpreet Singh Grover, Satnam Singh and Bonamali Pal, "Enhanced photocatalytic activity of TiO_2 nanowires for photooxidation of Propiconazole", **(Manuscript under preparation)**

List of papers/poster presented in conferences

1. Inderpreet Singh Grover, Vishal Mutreja, Bonamali Pal and Satnam Singh, "Photocatalytic degradation of sulfosulfuron herbicide by metal loaded TiO2 photocatalyst". International Conference on Nanotechnology and its Applications in Medical Sciences held at D.Y Patil University, Kolhapur (India) in 21st – 23rd Oct. 2010

2. Inderpreet Singh Grover, Vishal Mutreja, Satnam Singh and Bonamali Pal*, "Size and shape dependent synthesis of TiO2 nanoparticles and study of their comparative photocatalytic activity". National Symposium on Nanoscience and Nanotechnology (Nanostech-2011), Benchmarking-Science and Society, held at Nirmala College, Muvattupuza, Kerlea (India) in 1st-2nd Sep. 2011

3. Inderpreet Singh Grover, Satnam Singh & Bonamali Pal "Prepration and characterization of TiO2 nanoparticles of different shapes and their comparative photoactivity", Nanoscience and Technology (NanoSciTech-2012) held at Panjab University, Chandigarh, India ***(Awarded 2nd Prize),*** 16th – 18th Feb. 2012

4. Inderpreet Singh Grover, Bonamali Pal and Satnam Singh,"Priority PAHs in orthodox black tea manufacturing process", Recent Advances in Chemical and Environmental Sciences held at Modi College, Patiala (India), 3rd March. 2012

5. Inderpreet Singh Grover, Vishal Mutreja, Bonamali Pal and Satnam Singh, "Shape Dependent Synthesis and Photocatalytic Activity of Titania Nanostructures", Internantional Conferenec on Emerging Technologies held at BITS, Pilani-Goa (India). 23rd – 24th Feb. 2013

6. Inderpreet Singh Grover, Satnam Singh and Bonamali Pal, "Thermal Stability of Anatase TiO2 nanorods", National Conference on Innovative Molecules for Sustainable Future (NCIMS-2013), held at Thapar University, Patiala (India) in 24th – 26th Oct, 2013

7. Inderpreet Singh Grover, Satnam Singh and Bonamali Pal, "Effect of thermal treatment on morphology and photocatalytic activity of Fe-impregnated sodium titanate nanotubes**,** Powder Granular Bulk Soilds: innovations and Applications (PGBSIA-2013), held at Thapar University, Patiala (India), Nov. 2013

8. Inderpreet Singh Grover, Satnam Singh and Bonamali Pal, Photocatalytic and electro-kinetic properties of as-prepared titania nanostructures having different surface structures and crystal phases". Advanced oxidation Processes (AOP), held at Thapar University, Patiala, India ***(Awarded Best Oral Presentation),*** 21st - 23rd Nov. 2013